DESIGN AND COMMISSIONING OF A CONTINUOUS ISOTHERMAL FAST PYROLYSIS REACTOR

A Thesis
Presented to
The Academic Faculty

by

Samuel Melville Glauber

In Partial Fulfillment
of the Requirements for the Degree
Master of Science in the
G. W. Woodruff School of Mechanical Engineering

Georgia Institute of Technology
May 2013

DESIGN AND COMMISSIONING OF A CONTINUOUS ISOTHERMAL FAST PYROLYSIS REACTOR

Approved by:

Dr. J. Rhett Mayor, Advisor
G. W. Woodruff School of Mechanical Engineering
Georgia Institute of Technology

Dr. Yogendra Joshi
G. W. Woodruff School of Mechanical Engineering
Georgia Institute of Technology

Dr. John Muzzy
School of Chemical and Biomolecular Engineering
Georgia Institute of Technology

Date Approved: 01/11/2013

I would like to dedicate this work to my parents to thank them for not moving us to Montana all those years ago, and likely ruining my academic future.

ACKNOWLEDGEMENTS

I would like to thank the Chevron Corporation for providing the funding for this research, Dr. Alexander Williams for laying the groundwork for this work through his extensive research on fast pyrolysis of *Pinus taeda*, and Charlotte Wheat for her assistance in preliminary testing and biomass preparation.

I am grateful to my committee members: Dr. John Muzzy and Dr. Yogendra Joshi, whose insight, analysis, evaluation, and recommendations much improved this work.

I would especially like to thank my advisor, Dr. J. Rhett Mayor, who has challenged my models, designs, and results to push me to improve the quality of all of them, while pushing me to become a critical researcher and engineer.

TABLE OF CONTENTS

LIST OF TABLES

LIST OF FIGURES

SUMMARY

In order to meet growing demands for alternatives to fossil fuels, biomass pyrolysis is a method that has been explored in depth as a method to develop new liquid fuels. Fast pyrolysis is a subtype of pyrolysis reaction in which a specimen is heated at rates in excess of 10°C/s in an oxygen-free environment, causing the specimen to thermally degrade and release a volatile bio-oil. The goal of this study is to design and commission a novel reactor for the continuous isothermal fast pyrolysis of ground biomass. The reactor design utilizes a vibrating plate heated to a set pyrolysis temperature. Analytical and empirically-derived vibratory transport models are presented for ground *Pinus taeda* (loblolly pine) to assist in setting the desired pyrolysis reaction time. A condenser system was designed to rapidly evacuate and chill the volatiles to prevent tar formation and secondary reactions. Commissioning tests were run at a pair of temperatures and biomass residence times to determine the degree of agreement between the reactor yields and two-component volatile formation data derived from batch fast pyrolysis of *Pinus taeda*.

CHAPTER 1

INTRODUCTION

1.1 Introduction

There is an increased need to develop alternative liquid fuels to meet growing energy demands. With oil production expected to reach its zenith around 2050 [1], additional liquid fuel supplies must be developed to offset declining production in the latter half of the century. Pyrolysis is a potential process for achieving this increase, but still requires significant development in preprocessing techniques, feedstock breeding and selection, and reactor design, before it will be commercially viable.

Pyrolysis is a process in a chain of thermal degradation reactions, in which heat is applied to biomass or other carbonaceous solid material in the absence of an oxidizing agent, preventing combustion. Up to temperatures of 200°C, free water is driven from the feedstock. Following this, the feedstock undergoes a process called torrefaction, where some additional bound water is driven off and the biomass particle undergoes densification, forming an energy-dense solid fuel [2]. In a range of 280°C to 750°C, a pyrolysis reaction occurs within the organic substance, breaking down cellulose, hemicellulose and lignin in the biomass, driving off organic vapors, and leaving char. When cooled, a light bio-oil may be condensed out of the vapor phase, while the non-condensable gases, primarily carbon monoxide (CO), carbon dioxide (CO_2), methane (CH_4), and hydrogen (H_2), may be captured or combusted. If the temperature is increased past 750°C [3], the remaining organic molecules will break down into simple molecules such as water vapor and CO. Combining these, and the remaining char, with steam and oxygen will force a gasification reaction, generating additional CO_2, CO and H_2. A water-gas shift reaction can be further used to convert CO into CO_2 while converting H_2O into H_2. The thermal degradation process is illustrated in Figure 1.1.

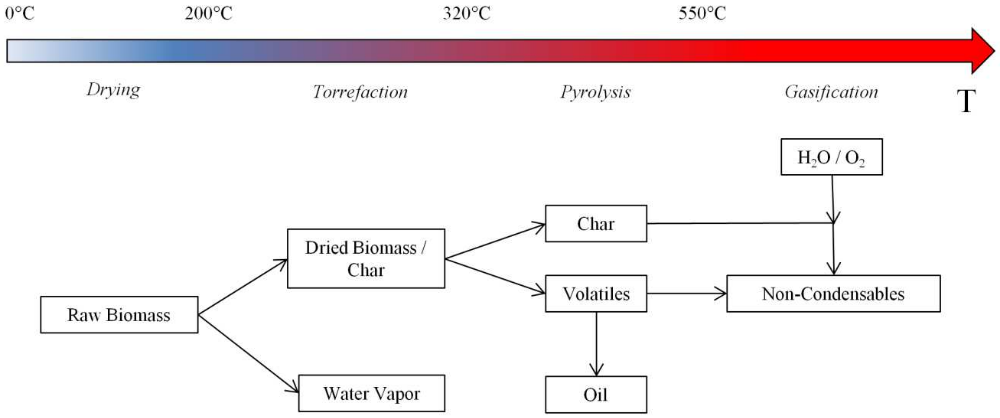

Figure 1.1 - Flowchart Illustrating Detailing Product Production During Torrefaction, Pyrolysis and Gasification and Associated Temperature Ranges

Extensive work has been done to characterize the oil produced from pyrolysis of various species of woody biomass [4-8], leafy biomass [9-11], and recyclable or waste materials [12-15]. Not only are these sources renewable, but they are considered "carbon neutral," as replacing harvested feedstock requires planting additional plants that, in turn, absorb atmospheric carbon dioxide. The oils driven off of organic material is incredibly complex; Azeez *et al.* [5] identified 80 distinct molecules in pyrolysis oil, yet these only accounted for 45% of the oil mass. Consequently, these investigations have yielded oil with lower lower heating values (LHV) than refined fossil fuels; Mayor and Williams [16], for example, reported an LHV of 14.04 MJ/kg for oil condensed from *Pinus taeda* fast-pyrolyzed at 400°C, whereas octane is typically taken to have an LHV of 44.43 MJ/kg [17]. High acidity is also reported; Oasmaa *et al.* [18] report a total acid number (TAN) of 60 for pyrolysis oil, compared with 0.5 for crude oil [19]. Therefore, pyrolysis oils require extensive refining before they may be used as an acceptable bio-diesel for use in motor vehicles. The pyrolysis oil may also serve as an effective turbine oil. Torrefaction, which drives of water and some acidic compounds, has been shown to make bio oil easier to process downstream, but reduces yields [20].

Loblolly pine (*Pinus taeda*) was the species of biomass that this study focused on. This chosen for a number of reasons. *Pinus taeda* is a fast-growing softwood native to the southeastern United States and eastern seaboard between New Jersey and Florida. Stands can reach heights of 13.5 m (44.2 ft) after a fifteen year growth period, yielding 17.230 tonnes/acre dry weight of chip-and-saw wood [21], making it an interesting potential commercial energy source. Furthermore, earlier work carried out at Georgia Tech by Williams [4] investigated the thermal and chemical kinetics of loblolly pine using a novel micro-reactor, providing a strong body of work to compare results to.

This work aims to build on this research, incorporating a larger continuous reactor. This work focuses exclusively on fast pyrolysis. In fast pyrolysis, heating rates fall between 10°C and 300°C/s [22-24]. Such high heating rates, necessitate processing of small particles so that, in basic analysis, heat and mass transfer may be decoupled, as heating rates are much greater than mass diffusion rates. Even so, the mass flow rate of biomass must be restricted to ensure the necessary residence time (contact time with the heating medium) for fast pyrolysis of ground *Pinus taeda*. William's [4] work, for fast pyrolysis between 380 and 420°C, puts this at at least 50 s to ensure complete pyrolysis as determined by a single-component kinetic model, but more complex kinetics models indicate that 100 s or more is highly desirable.

1.2 Research Objectives

The goal of the proposed research is to design, build and commission a continuously feeding reactor to characterize the yields of fast-pyrolyzed Loblolly pine. In support of this goal, the following research objectives will be pursued:

1. To measure vibratory transport characteristics of ground woody biomass on an inclined surface.
2. To measure the mass conversion efficiency of biomass undergoing isothermal fast pyrolysis as a function of temperature and residence time.
3. To demonstrate the application of fast pyrolysis kinetics to the design of vibro-fluidized bed pyrolysis reactors.

1.3 Thesis Organization

This study presents a detailed design and evaluation process for a continuous fast isothermal pyrolysis reactor. Heat transfer requirements are explored in detail to ensure that power requirements are met, and that products are condensed in a manner conducive to oil, rather than tar, production. A detailed examination of the vibratory spreading mechanism used to transport biomass is further presented. In this study, vibratory spreading characteristics of *Pinus taeda* were explored to facilitate easier spreading in the continuous reactor.

A detailed overview of the reactor design and construction is presented, along with possible modifications for increased efficiency. Mass yields are presented, alongside derived experimental uncertainty, and compared with results from the work performed on the micro-reactor by Williams. Finally, a proposal for improving the continuous reactor is presented.

CHAPTER 2

REACTOR CONCEPTUAL DESIGN

2.1 Introduction

This chapter details the design of a novel reactor developed to continuously pyrolyze woody biomass under a light vacuum. Three novel designs were considered: a spread and scrape heated plate reactor, a continuous belt reactor, and an inclined plate reactor, which was selected. In this design, an eccentric mass mounted on a motor was spun to shake an H frame platform. The platform was mounted on a central tower, henceforth referred to as the heating tower, on four rubber vibration isolators. Mounted to this platform was the heated plate which may be pivoted between -5 and 20°. The heating tower was mounted to a mobile box frame base, and enclosed by a thin-walled stainless steel canister. A plexiglass roof was attached with a feeder mechanism built in. The feed system delivered discrete deposits of ground biomass at regular intervals, which was gravity-fed from and stored in a stirred hopper. A nitrogen purge kept the feedstock, reactants and products from combusting.

2.2 Review of Salient Literature

Several different methods of pyrolysis have been explored in detail since the 1970’s. These include ablative pyrolysis, fluidized bed systems, entrained flow systems, vacuum pyrolysis and solar pyrolysis [25-29]. The majority of this research has utilized either ablative pyrolysis or fluidized bed pyrolysis, as their operation is the best characterized and understood.

Ablative pyrolysis relies primarily on conduction between a heated, non-reacting surface, and a piece of biomass. The biomass, which need not be ground to the millimeter scale, is pressed into and slid along a heated surface [30], often a spinning disc [25]. As the particle of biomass passes, volatiles form a layer of oil on the hot surface and then evaporate and are collected and condensed. This is advantageous because it does not require the biomass to be ground beforehand and does not require a carrier gas to handle the volatiles. On the other hand, the remaining char can cause wear on the system--though char yields are typically lower [31]--and heating methods are complex and often difficult to sustain [26].

Fluidized bed reactors incorporate a bed of granular material, typically sand or salt ground to a diameter of 250 μm [25], that has been heated to the desired pyrolysis temperature. An inert carrier gas is pumped into the reactor through the bottom of the bed, fluidizing it. A feed mechanism, often a screw feeder, feeds ground biomass particles into the bed. The biomass particles, which are less than 6 mm in diameter, mix with the sand, and pyrolyze, primarily due to conduction. The volatiles leave the particles, and are swept by the carried gas out through the top of the reactor, and passed through a series of cyclones, to remove any stray char or bed particles that may have come with it, before being condensed. Non-condensable gases may be reheated and used as carrier gas [25]. The advantages of using such a system include the high heat transfer rates associated with heavy particle interaction, and production of finely-ground char. Disadvantageously, the produced char must be separated from the bed material using a complex solids separation system, the hot solids in the reactor may lead to secondary thermal cracking of the volatiles, and the char remaining in the system may catalytically crack the volatiles as well, leading to tar formation.

Entrained flow reactors are primarily convection-driven systems where hot inert carrier gas is passed through ground biomass [32, 33]. Because gases have low thermal conductivities, particles must be small (less than 2 mm) in order to pyrolyze fully [25]. Because the biomass is ground so fine, the particles are consequently transported by the carrier gas up through the reactor. The walls of the reactor are often heated to ensure that devolatilization continues along its entire span. In some systems, where burning propane is the heating method, the combustion gasses are allowed to mix with the carrier gasses [32] to help boost reactor efficiency. At the top of the reacting tube, a cyclone separates the char from the gasses, and the volatiles are quickly condensed. Entrained flow reactors share the solids separation drawback with fluidized bed models in that they require filtering out char particles from the bulk flow medium, in this case, requiring a cyclone. This increases the residence time of the pyrolysis vapors in the reactor, potentially leading to secondary reactions and tar buildup, which both wastes the prepared feedstock and forces the reactor offline for cleaning.

Vacuum pyrolysis does not refer to a specific type of pyrolysis reactor, but rather refers to a condition under which pyrolysis takes place. In vacuum pyrolysis, the chamber of the reactor is significantly evacuated--Garcia-Perez [34] reports evacuating to as little as 8 kPa absolute pressure inside the test section--which alters the kinetics of the reaction. Heat transfer rates are lower in vacuum pyrolysis as such systems must rely on conduction or radiation, but mass transfer rates increase because of the low pressure. Thus, even though the heating simulates slow pyrolysis, the combined kinetics respond as fast pyrolysis to the point where Carrier *et al.* [35] found that vacuum pyrolysis at 8 kPa yielded a gas residence time of only 2-3 s, while the residence time for a similar slow pyrolysis reaction was 165-70 s. Larger biomass samples are typically used here, as the low pressure sometimes carries away smaller char particles with the vapor. This phenomenon encourages the use of cyclones in pilot scale plants to prevent char from reacting with the condensed oil [34, 36].

Some research has been done into solar pyrolysis, but the method is not common. In this system, white light from the sun is focused on a single point of a reactor, typically the center of a quartz tube, through which a stream of ground biomass would pass in a carrier gas [28, 29, 37]. Such systems are very similar to entrained flow designs, although some fluidized bed models have been proposed [27], and may incorporate vacuum pyrolysis elements. The major economic drawbacks of such a system are that they cannot operate without sunlight, and they require adequate space for a solar field to direct light into the reactor. More importantly, very little biomass can be processed at any given point. Only a single stream of fine particles may pass through the hot spot without blocking radiation from the others, and if a single particle were exposed to the heating source multiple times, as in a system using a fluidized bed instead of an entrained flow, a particle could experience thermal shocks and secondary reactions [27]. On top of this, biomass and its major chemical components, such as cellulose, exhibit high reflectivity [38].

The microreactor developed by Williams [4], on which this reactor is partially based, used a heated plate, using vibratory and swept arm spreading to disperse biomass for pyrolysis. The system was manually fed and only pyrolyzed discrete samples of biomass. Cartridge heaters brought the reacting surface disc to temperature, and the assembly was vibrated while a pair of rotating spreaders spread the biomass evenly around the surface of the disc. Following pyrolysis, during which a helium stream transported the pyrolysis vapor into a cold finger condenser cooled by liquid nitrogen, the spreader arms would make several sweeps of the disc to push the char into a char catch.

2.3 Potential Reactor Designs

Before beginning to design a reactor, a foundation of desired metrics must be laid out to ensure that the pyrolysis reactor both reacts fast, isothermally, and continuously, and advances the domain of reactor design knowledge. A number of target metrics are presented in Table 2-1.

Table 2-1 – Target Reactor Design Metrics

Design Metric	**Value or Range**
Mass Flow Rate	1.5 kg/hr
Pyrolysis Temperature	380-420 °C
Temperature Gradient Across Reaction Zone	0 °C/m
Particle Residence Time	50-300 s
Vapor Residence Time	3 s ≤
Oil Mass Yield	0.2-0.5 g/g
Maximum Run Time	≥ 2 hr

In order to hit these target metrics the reactor must accomplish the functions laid out in the reactor function tree presented in Figure 2.1.

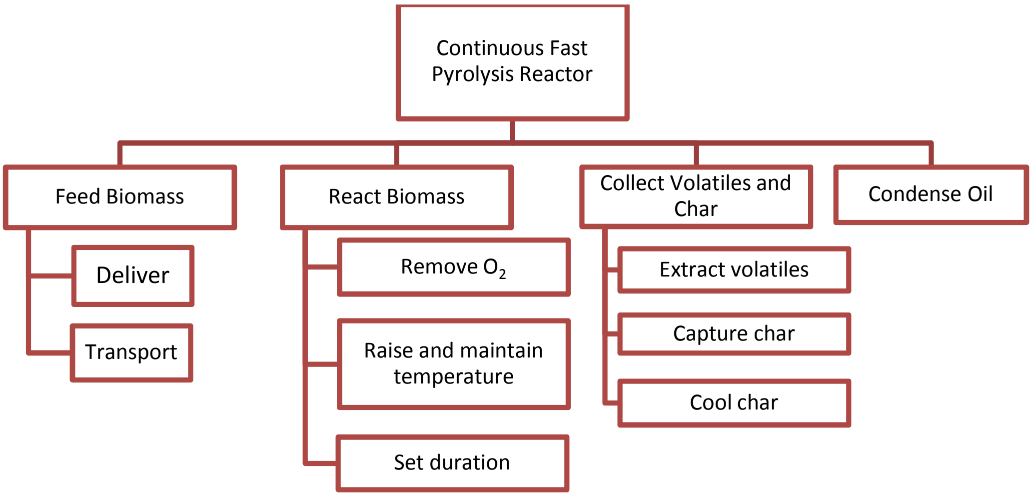

Figure 2.1 - Reactor Function Tree

In order to meet these design metrics and satisfy these reactor functions, three novel potential designs were explored: a spread and scrape heated plate reactor, a continuous belt reactor, and an inclined plate reactor.

2.3.1 Spread and Scrape Heated Plate Reactor

The spread and scrape heated plate reactor (illustrated in Figure 2.2) utilizes a stainless steel plate with an imbedded copper plate situated horizontally under a fume hood. Cartridge heaters are imbedded within the copper plate which, due to the high thermal conductivity of copper, spreads heat evenly across the plate, bringing the non-reactive surface of the stainless steel to a uniform temperature. Ground material is dropped onto the plate, and a spreading bar on a conveyer belt spreads this material to a uniform thickness across the plate. A scraper bar follows the spreader at a distance, scraping the resulting char into the char catch following the desired particle residence time.

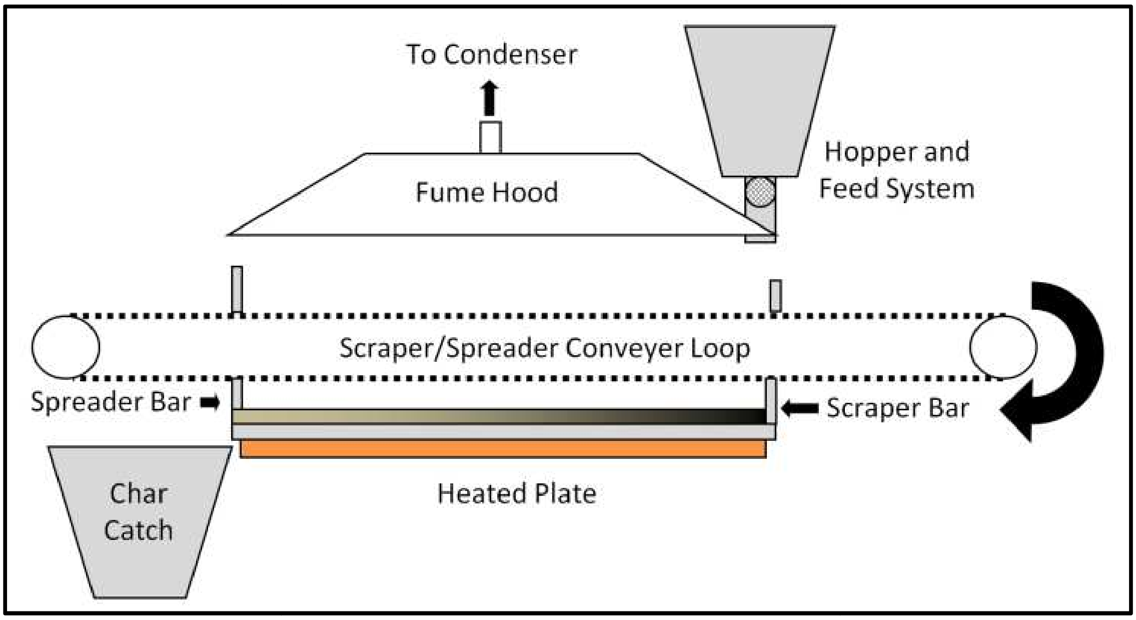

Figure 2.2 - Spread and Scrape Heated Plate Reactor

Like an ablative reactor, this design would allow for high heating rates without heating a secondary heat transfer medium. Unfortunately, also like ablative reactors, prolonged use would ensure wear from interactions between the char, reacting surface, and scraper bar. Such wear could result in incomplete clearing of reacted char, leading to secondary reactions and incomplete pyrolysis of later material.

2.3.2 Continuous Belt Reactor

The continuous belt reactor incorporates a stainless steel belt onto which biomass is deposited and spread. The belt moves through a series of reaction chambers where the bed is heated and volatiles collected, making adaptation for fractionated pyrolysis easy. The resulting char is cooled before being dropped into a char catch. Three methods of bed heating were explored: a radiant heating design (illustrated in Figure 2.3) in which infrared radiation from a radiant heater is concentrated in a band across the width of the belt, an electric resistance heating design wherein a current is passed across the width of the belt causing the belt temperature to rise, and a conduction design where a heated copper block is pressed into the underside of the belt.

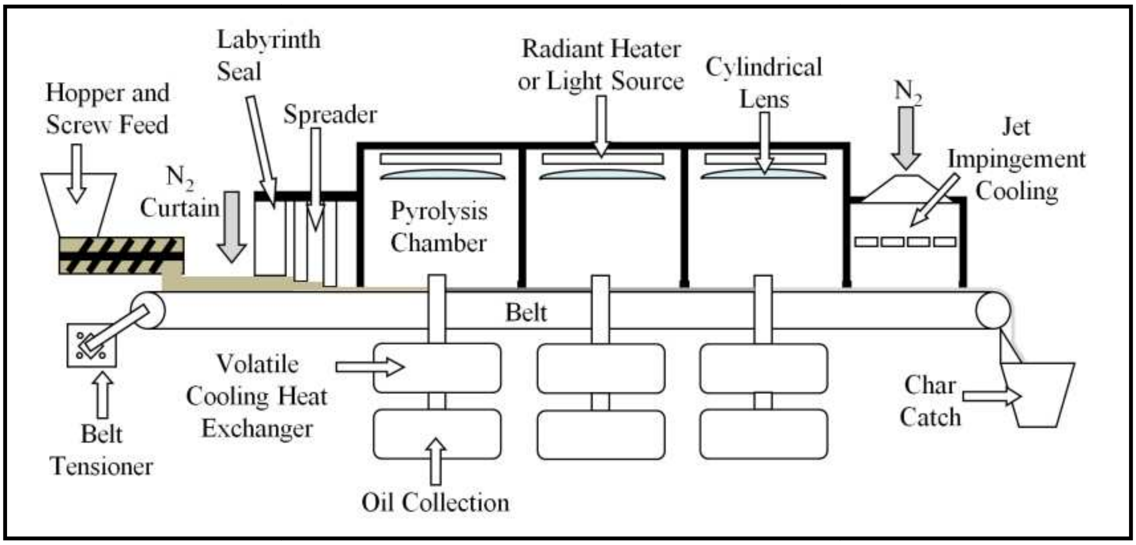

Figure 2.3 - Continuous Belt Reactor

Maintaining reaction temperature was found to be too difficult in this design. The belt, due to the high stiffness of stainless steel, must be kept thin leading to a fin-like effect wherein the belt rapidly loses heat. Radiant heating can only pyrolyze a thin strip of material at a time, leading to low residence times and rapid changes in particle temperature as it enters and exits the heated band. Electric resistance heating would require significant power input for losses in the belt to lead to a pyrolyzing temperature. Finally, conduction heating would require pressing heated blocks into a sliding surface, leading to high contact resistance and inefficient heating, not to mention the use of large, heavy, and expensive copper blocks to offset losses in the belt.

2.3.3 Inclined Plate Reactor

The inclined plate reactor utilizes heated stainless steel plates similar to the one used in the spread and scrape reactor. These plates are mounted on frames that may be vibrated via an eccentric mass. The frames are attached to a central tower inside a sealed chamber, and the plates can be set at varying angles. During operation, the plates are vibrated such that the material dropped onto them is spread evenly across the plate and spends a set amount of time on the plate. A pair of spreader bars on the topmost plate help to spread the material to an even bed depth. Volatiles are collected through a fume hood placed above each level. The reactor design is illustrated in Figure 2.4 and Figure 2.5.

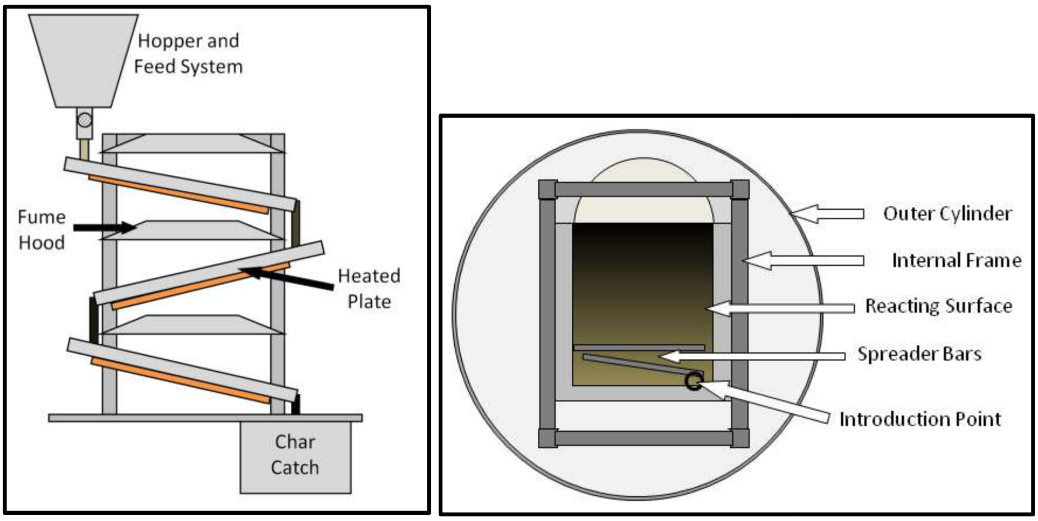

Figure 2.4 - Side and Top Interior Views of Inclined Plate Reactor

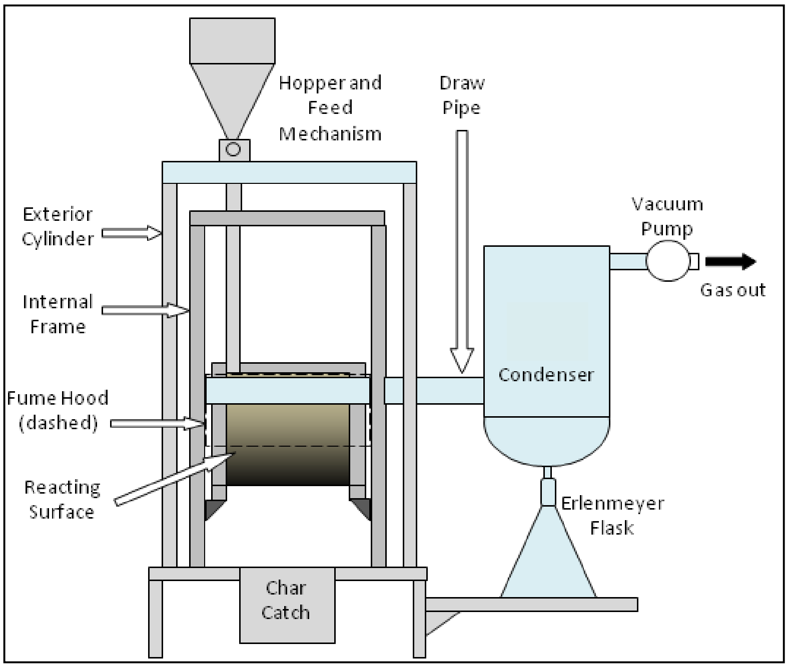

Figure 2.5 - Inclined Plate Reactor, Front View (Single Stage Shown)

The inclined plate reactor does not suffer from the same wear issue that the spread and scrape plate design does, nor does the design suffer the same magnitude of heat losses that the continuous belt design does. This design was therefore selected. The heat transfer aspects of this design are outlined in Chapter 3, and the vibratory transport aspects in Chapter 4.

2.4 Solid Modeling of Key Subsystems

Solid models of the inclined plate reactor subsystems were developed. These efforts were primarily focused on determining geometry and part orientation for key subsystems, namely the feed system and individual inclined plate levels.

2.4.1 Solid Modeling of Feed System

Figure 2.6 depicts a solid model of the feed system, and presents several key features: the hopper, paddle feed system and the hopper stirrer.

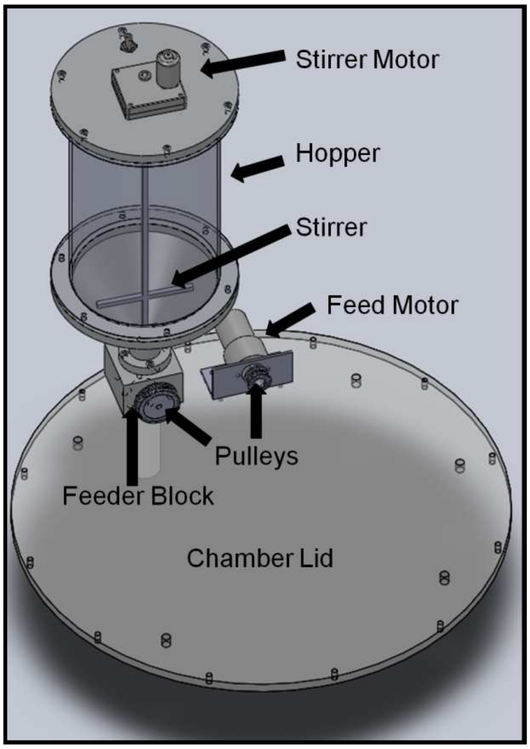

Figure 2.6 - Solid Model of Reactor Feed System

The hopper is sized so as have sufficient volume to run for two hours. The paddlewheel feed system (wheel depicted in Figure 2.7) uses two slots to deliver small volumes of biomass automatically into the feed chute and reactor. The slots are sized (see Chapter 5 for details) to ensure that the target mass flow rate may be met without running the feed motor at an excessive rate (> 60 rpm). Finally, a stirrer was designed to prevent ground biomass from clinging to the walls of the hopper.

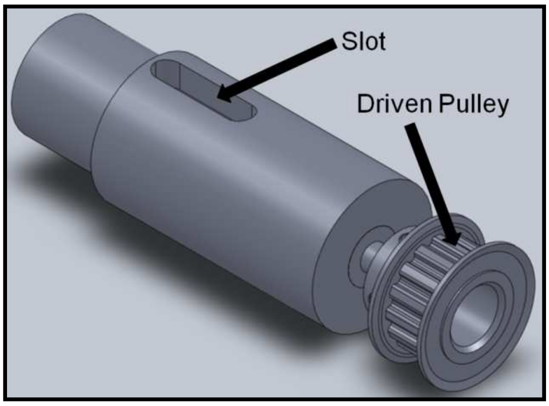

Figure 2.7 - Paddlewheel Paddle Detail (2nd slot hidden)

2.4.2 Solid Modeling of Reactor Level

Figure 2.8 illustrates the reactor level before it is attached to the internal frame of the reactor.

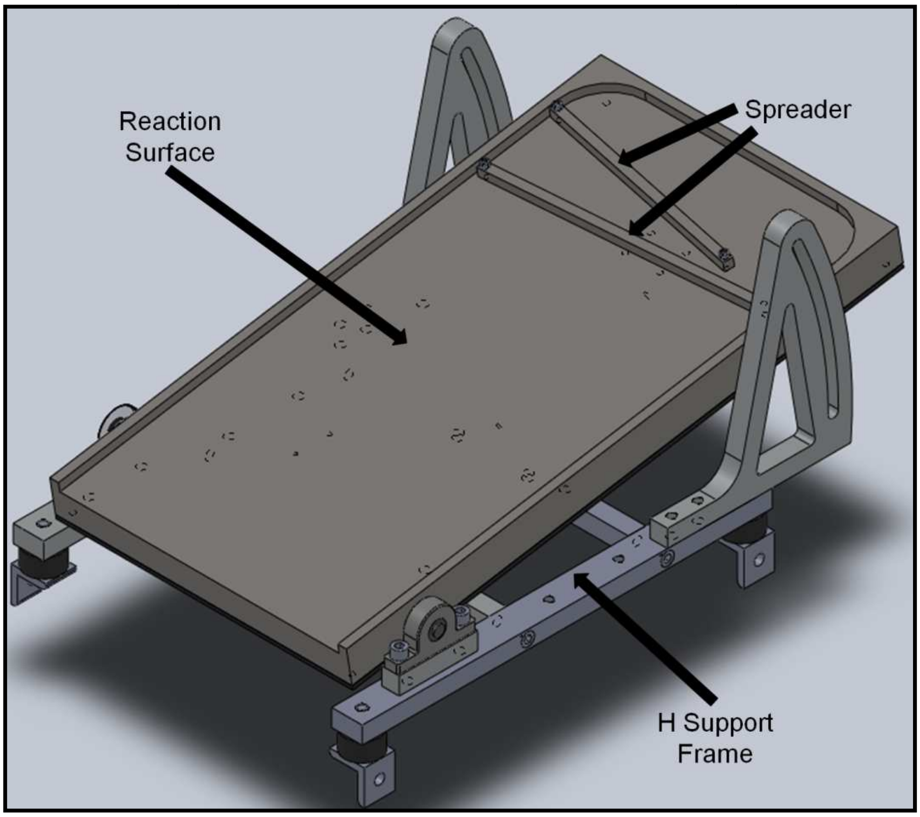

Figure 2.8 - Solid Model of Inclined Plate Heater Level

The plate is held at an angle via an adjustable rear support mechanism, allowing the angle of the plate to be adjusted. Two support mechanisms were considered: a threaded rod that could be locked into place with a pair of nuts, and a pair of fixed supports which the plate would be fixed to by tightening bolts that ride in the slots of the supports and bolt into the sides of the plate. These two support mechanisms are depicted in Figure 2.9.

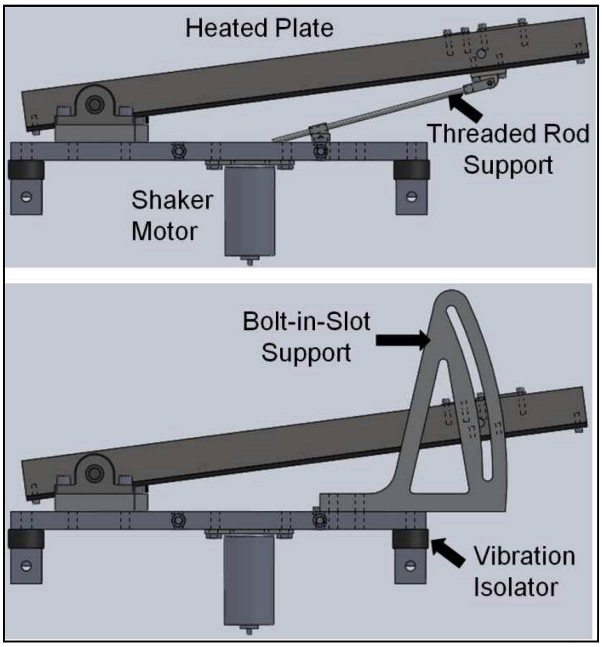

Figure 2.9 - Detail of Plate Support System Showing Threaded Rod Arrangement (top) and Fixed Suport Arrangement (bottom)

An motor with an eccentric mass (illustrated in the center of the frame in Figure 2.9) is mounted to the support frame for the plate, providing the vibratory input, and adjustable-height spreader bars spanning the width of the plate surface allow biomass falling onto the plate to spread evenly across the width of the plate. The support frame itself is mounted on cylindrical vibration isolators to isolate the level from damping by the frame.

The plate, when attached the frame is illustrated in Figure 2.10. The figure further illustrates the shape of the fume hood, support frame design, and char catch placement and char catch cooling fan support.

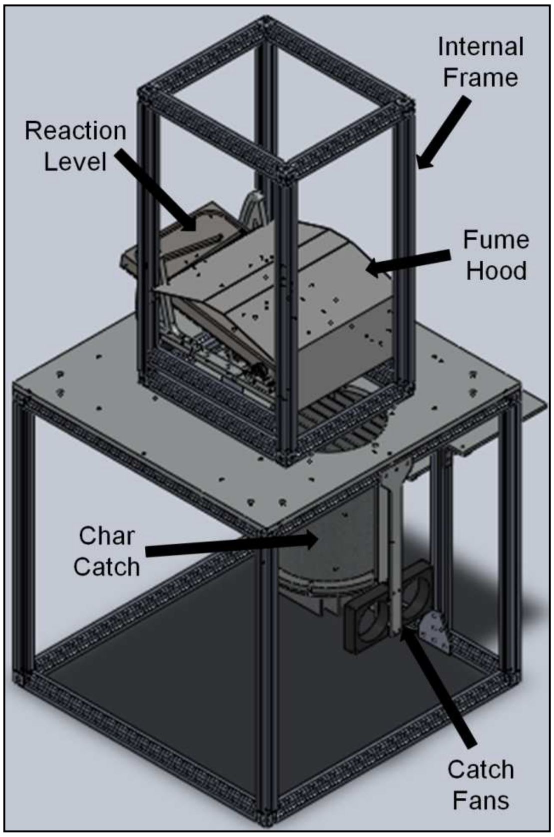

Figure 2.10 - Solid Model of Inclined Plate, Char Catch, and Cooling Fans Mounted to Main Support Frame

2.5 Summary

A design overview of the novel reactor design was presented. Three novel reactor designs were explored following a review of reactor design literature. An inclined plate reactor was selected and designed. Solid models were developed for key reactor subsystems to assist in sizing and fabrication.

CHAPTER 3

REACTOR THERMAL ANALYSIS AND DESIGN

3.1 Introduction

The most important factors in driving and controlling a fast pyrolysis reaction is the heating of the reactants and cooling of the products. Heat is required to bring the biomass up to temperature, and then maintain the bed at temperature as well as sustain the endothermic pyrolysis reaction. The resulting products must also be cooled. If allowed to linger at reaction temperature, the vapor will form tar through secondary reactions. It is therefore necessary to cool the vapor rapidly, condensing it into oil. Similarly, the remaining char must be cooled to keep if from undergoing secondary reactions, and so the cooling system for that must also be designed.

The reactants undergoing pyrolysis follow the temperature vs. time curve illustrated in Figure 3.1.

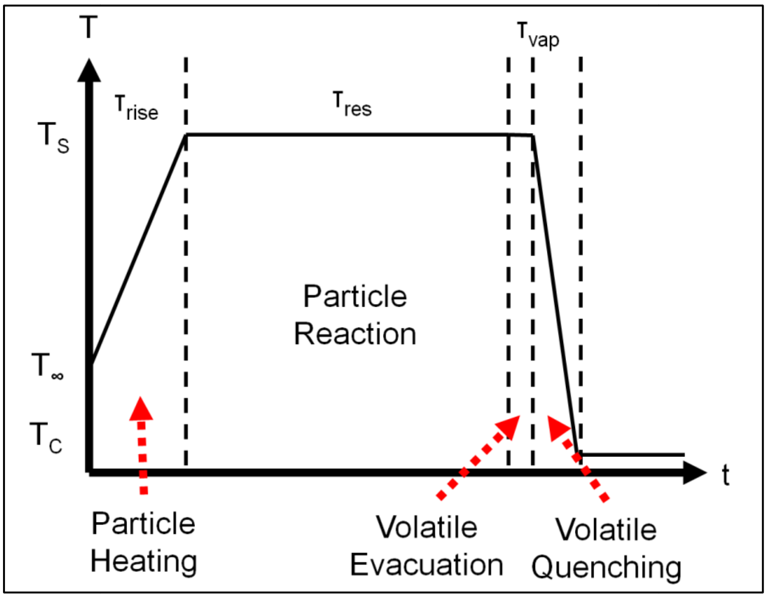

Figure 3.1 - Temperature vs. Time Curve for Pyrolysis Reactants

For *Pinus taeda* (loblolly pine), Williams [4] found that the heating rate was 400°C/s leading to heating time, τ_{rise}, for ground particles of 1 s. As the proposed reactor also incorporates particles of similar size on a heated surface, the rates are assumed to be the same within the reaction zone. The particles remain at the reaction temperature, T_S, for a set particle residence time, τ_{res}. This time is set by the settings of the vibratory transport system detailed in Chapter 4. The volatiles are assumed remain at T_S during the evacuation process. Finally, the volatiles pass through the condenser system, reaching a temperature of T_c. Together the volatile evacuation and quenching processes take some time, τ_{vap}, referred to as the vapor residence time.

3.2 **Review of Salient Literature**

A major consideration of heating biomass is the amount of energy required to bring it to temperature and the additional amount to pyrolyze it. Studies on heat of pyrolysis have been performed on several types of woody biomass. Beech wood, in work done by Gomez [39], exhibits a heat of pyrolysis of 222 kJ/kg contrasting with values given by Rath [40] in which heat of pyrolysis was found to vary widely with residual char fraction. Several researchers have reported exothermic reactions at higher residual char fractions, and determining endo or exothermicity of these reactions can only be carried out for slow pyrolysis reactions, leading to a problem in accurately determining heat of pyrolysis. The typical range for generic wood species lie between -150 and 360 kJ/kg [40]. Koufopanos *et al.* [41] names the heat of pyrolysis of pine to be 255 kJ/kg, which will, following the lead of Williams [4], be used for the heat of pyrolysis of pine. Van de Velden *et al.* [42] further indicates that ground material exhibits a higher heat of pyrolysis; mixed wood sawdust was found to have a heat of pyrolysis of 418 kJ/kg.

The specific heat of wood and char vary considerably with temperature. Several models have been set forth. Grønli [6] proposed a temperature-dependent specific heat for the wood and char of softwoods. Extensive experimentation has been carried out, using thermogravimetric analysis while samples undergo slow pyrolysis, leading to a wealth of mass loss data. Research into pyrolysis of macroscale samples have exhibited significant shrinkage and cracking in the presence of high heat loading [6]. As the volume of the sample is decreased, the shrinkage effects become noticeably smaller, but persist at the ground biomass scale. Models by Papadikis *et al.* [43] for fluidized bed reactors have modeled shrinkage in particles of comparable size with the tested particles. Sorum and Grønli [15] explored the pyrolysis of multiple species, mostly wastes, but included a good analysis of spruce which act similar to pines. Williams [4] tested *Pinus taeda* using thermogravimetric analysis, developing a highly useful mass-temperature relationship curve.

Radiative properties of biomass must also be considered given the high temperatures at which pyrolysis occurs. The emissivity of biomass is high relative to the reactor materials, but are not easily classifiable. Koufopanos *et al.* [41] lists the emissivity of wood at 0.9, which increases to 0.95 as it chars [44]. The reactor materials, by contrast, tend to be polished or lightly oxidized metals. Aluminum surfaces such at the reactor floor and radiation shields have an emissivity of between 0.05 and 0.2 depending on whether they are polished, or lightly oxidized respectively [45]. Stainless steel that has been cleaned or polished exhibits an emissivity between 0.17 and 0.26 at temperatures around the 400°C desired reaction point [45].

3.3 Determination of Heat Load for Sustained Reaction

3.3.1 Bed Heating Model

Several methods were considered for controlling the temperature of the plate in order to maintain isothermality. The selected design uses a LabVIEW control system and surface thermocouple to toggle the power delivered to six 200W and two 100W cartridge heaters imbedded in copper plates on and off. Copper is used for its high thermal conductivity (360 W/m-K for 145, or "machinable," copper) to spread the heat evenly across the reacting bed. This heat is transferred through an area of 6.19×10^{-2} m^2 (96 in^2) into the vibrating bed of woody biomass flowing, under design conditions, at 1.5 kg/hr down the topmost, or "reaction," surface. In order to sustain bed isothermality, an a appropriate bed depth must be determined, and sufficient heat must be provided to bring the biomass to the desired pyrolysis temperature, to overcome the endothermic reaction that is the pyrolysis process, and to offset radiative and convective losses to the inert nitrogen environment.

Determining the energy balance for sustaining this reaction is very complicated, as convection losses from the bed due to the vibration of the particles is very difficult to predict. Additionally, the transient nature of the reactor and the temperature and time-dependent properties of the material being reacted create additional uncertainties that prevent problem formulation as a single line energy balance. Some heat losses--convection losses through the bottom of the plate, radiation losses, and the heat of pyrolysis which sustains the chemical reaction--may be modeled using known equations, but the energy balance of the bed will need to be performed using finite element analysis.

The convective losses on the underside of the plate will occur due to free convection in the nitrogen environment. The total bottom side area is assumed to convect, leading to a characteristic length of:

$$L_C = \frac{A_S}{P} \tag{3.1}$$

where A_s is the total surface area of the bottom face (8.26×10^{-2} m^2 or 128 in^2) and P is the perimeter (1.219 m or 48 in). The characteristic length is thus 6.775×10^{-2} m (2.667 in). To determine the convection coefficient, the Rayleigh number must first be determined. For a heated, downward-facing surface the Rayleigh number is defined as:

$$Ra_L = \frac{g\cos(\theta)\beta_{N_2} L_C{}^3 (T_S - T_\infty)}{\alpha_{N_2} \nu_{N_2}} \tag{3.2}$$

where g is the gravitational constant, θ is the angle of the plate, T_S is the temperature of the plate or bed surface, T_∞ is the temperature of the nitrogen, β_{N2} is the coefficient of thermal expansion of the nitrogen, α_{N2} is the thermal diffusivity of the nitrogen and ν_{N2} is the viscosity of the nitrogen. At a 15° incline and the plate heated to 400°C in a 22°C nitrogen environment, the resulting Rayleigh number is 2.90×10^6. For Rayleigh number values between 10^5 and 10^{10} the associated Nusselt number [45] for the downward-facing side of the plate is:

$$Nu_{L,d} = 0.27 Ra_L{}^{1/4} \tag{3.3}$$

the resulting free convection coefficient is given as:

$$h = \frac{Nu_{L,d} k_{N_s}}{L_C} \tag{3.4}$$

For the example given above, the resulting convection coefficient is 4 W/m^2-K.

The radiative losses occur primarily on the top and bottom faces of the plate, but because the emissivity of the bed is much greater than that of the stainless steel plate on the bottom face and because the bottom face radiates only to reflective metal surfaces, the top face, it is estimated, will be the dominant source of radiative losses. The radiative losses may be determined using (3.5):

$$q_{loss,rad} = \sigma \varepsilon_{eff} A_S \left(T_S{}^4 - T_\infty{}^4 \right) \tag{3.5}$$

where ε_{eff} is the effective emissivity of the system. The emissivity of the biomass radiating to a black body is not the effective emissivity, as a heated radiation shield is placed above the plate as depicted in Figure 3.2.

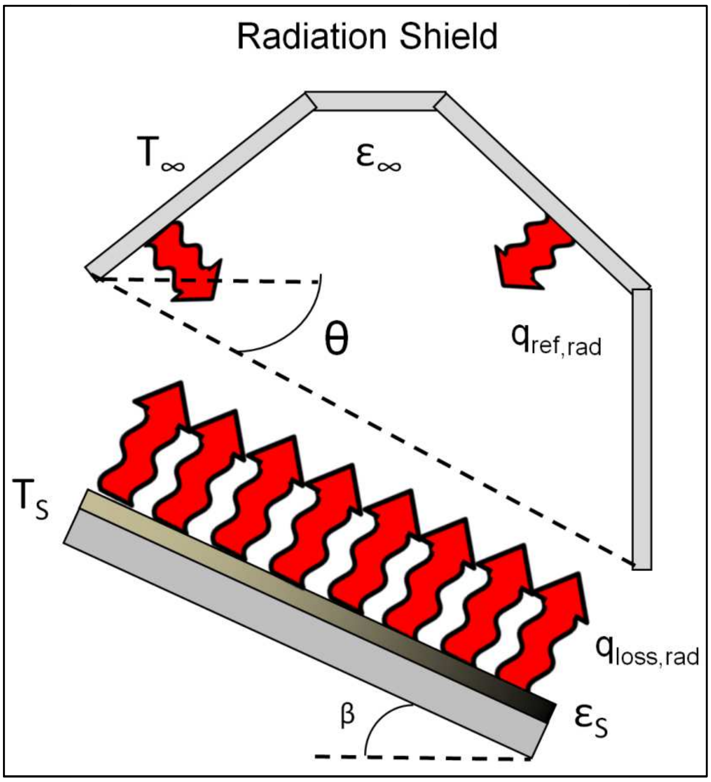

Figure 3.2 - Radiation Shield Aperture Above Reacting Surface

The effective emissivity is therefore given in (3.6):

$$\varepsilon_{eff} = \frac{1}{A_S}\left[\frac{1-\varepsilon_S}{\varepsilon_S A_S} + \frac{1}{A_S F} + \frac{1-\varepsilon_\infty}{\varepsilon_\infty A_\infty}\right]^{-1} \tag{3.6}$$

where ε_S is the emissivity of the hot surface, F is the view factor, ε_∞ is the emissivity of the radiation shield and A_∞ is the surface area of the radiation shield. Biomass has an emissivity of 0.95 and polished aluminum, which the radiation shield is formed from, has an emissivity of 0.05. The view factor for an inclined plate to a multi-faceted hood is very difficult to calculate, and so in order to select an appropriate view factor, the plate will be treated as radiating to an angled rectangular aperture with an emissivity consistent with polished aluminum, that is offset from the plate at a specified distance. The resulting view factor is determined by solving the integral presented in (3.7) [46]:

$$F_{1-2} = \frac{1}{A_1}\sum_{i=1}^{2}\sum_{j=1}^{2}\sum_{k=1}^{2}\sum_{l=1}^{2}\left[(-1)^{(i+j+k+l)} G\left(x_i, y_j, \eta_k, \xi_l\right)\right]$$

where

$$\begin{aligned} G = {} & -\frac{(\eta-y)\sin^2\alpha}{2\pi}\int_\xi \left(\frac{(x-\xi\cos\alpha)\cos\alpha - \xi\sin^2\alpha}{\left(x^2-2x\xi\cos\alpha+\xi^2\right)^{1/2}\sin^2\alpha}\tan^{-1}\left[\frac{\eta-y}{\left(x^2-2x\xi\cos\alpha+\xi^2\right)^{1/2}}\right]\right. \\ & +\frac{\cos\alpha}{(\eta-y)\sin^2\alpha}\left\{\left[\xi^2\sin^2\alpha+(\eta-y)^2\right]^{1/2}\tan^{-1}\frac{x-\xi\cos\alpha}{\left[\xi^2\sin^2\alpha+(\eta-y)^2\right]^{1/2}} - \xi\sin\alpha\tan^{-1}\left(\frac{x-\xi\cos\alpha}{\sin\alpha}\right)\right\} \\ & \left.+\frac{\xi}{2(\eta-y)}\ln\left[\frac{x^2-2x\xi\cos\alpha+\xi^2+(\eta-y)^2}{x^2-2x\xi\cos\alpha+\xi^2}\right]\right)d\xi \end{aligned}$$

(3.7)

where x and y define the bounds of the plate surface, and η and ξ defined the bounds of the aperture surface in the planes set at an angle of α apart from each other. The view factor for varying aperture-plate offset angles for this system is summarized in Figure 3.3.

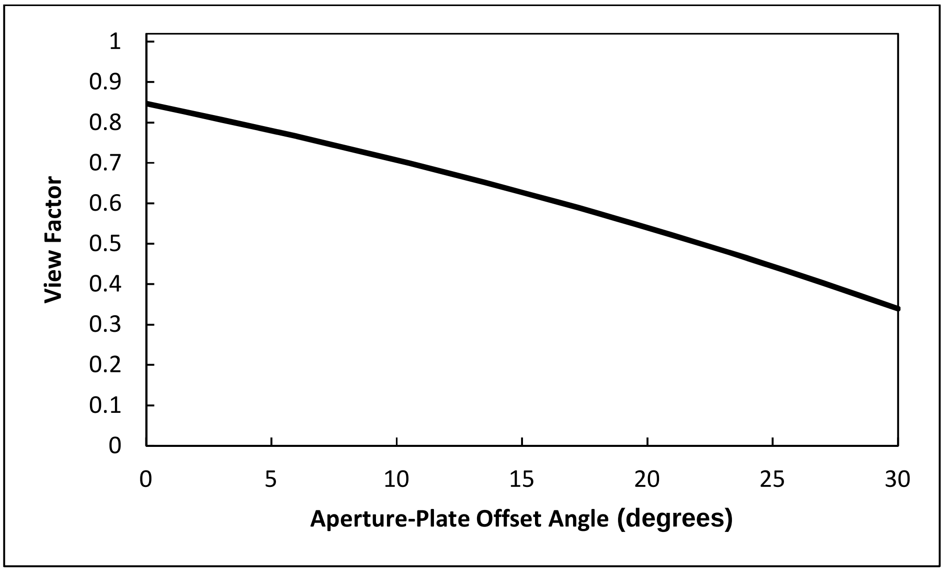

Figure 3.3 - View Factor with Varying Fume Hood Aperture - Plate Offset Angle

For testing, this offset angle is relatively low: 5°, and therefore the view factor is 0.78 and the effective emissivity is therefore 0.057. The resulting heat loss in the 400°C case is 40.1 W for an unheated radiation shield, and 31.5 W for a radiation shield heated to 200°C.

3.3.2 Determination of Bed Isothermality

The isothermality of the reaction zone must be ensured in order to sustain an isothermal pyrolysis reaction. Modeling isothermality in the reactor design is not a simple matter of applying a lumped capacitance check, as the boundary conditions on the plate are irregular and heat loading is uneven. Therefore, a finite element model is used to determine the bed surface temperatures within the designated reaction zone. Due to the complexities of modeling an open system in ANSYS's thermal modeling package, the bed will be assumed to be static. This is considered valid as, in fast pyrolysis, the material of the bed reaches temperature in a time that is much less than the typical desired residence time.

Three solid models of the stainless steel reacting surface, copper heating plates, and biomass bed were analyzed using the thermal modeling package in ANSYS 12. Each model was identical except for the depth of the biomass beds, which ranged, in 200 μm increments, from 200 μm (approximately the mean diameter of the tested particles) to 1 mm. A tetrahedral mesh with edge length of 63.5 mm (0.25 in.) was applied to the solids. A total heat load of 800 W was applied to the cartridge heater hole walls (100 W each), which converts into a heat flux of 206.7 kW/m^2. Radiation and convection coefficients consistent with the earlier presented work were applied to the appropriate surfaces, and a volumetric heat loss corresponding to pyrolyzing 1.5 kg/hr of material was applied to the bed to account for the heat of pyrolysis.

In order to model the convection losses through the top surface of the bed, a sensitivity study of three convection coefficients was performed. Because the material moves very slowly down the plate, with a maximum bulk velocity of 6 mm/s, the maximum convection coefficient is unlikely to be well within the range of forced convection. Hence an upper bound for the convection coefficient for the bed surface was set at 30 W/m^2-K which is in the transition zone between free and forced convection. Under conditions where bed thickness is high, the resultant bulk velocity is low, and therefore a lower bound convection coefficient of 10 W/m^2-K was set; approaching natural convection [45]. A third coefficient at the midpoint, 20 W/m^2-K, was also explored.

Figure 3.4 illustrates the mesh applied to the solid bodies, and Figure 3.5 calls out the heating conditions for the model geometry.

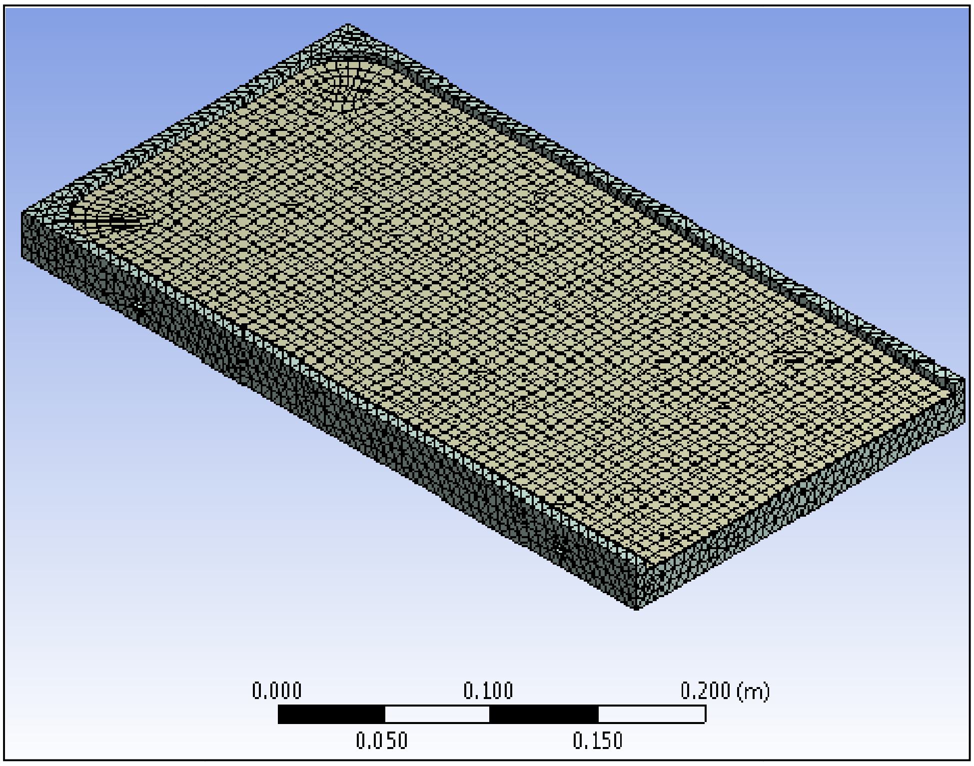

Figure 3.4 - Tetrahedral Mesh Applied to 200 μm Thick Bed Model

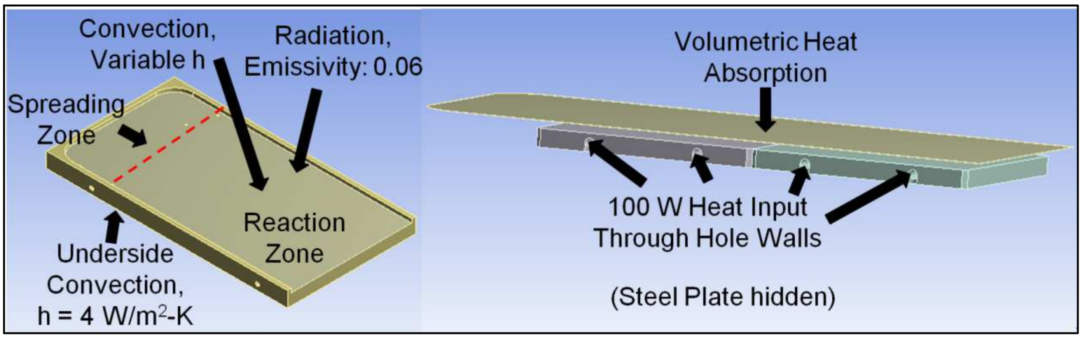

Figure 3.5 - FEA Model Geometry, Boundary Conditions, and Zones of Interest

Table 3-1 illustrates the surface temperature profiles of the various modeled bed depths at the three modeled bed surface convection coefficients.

Table 3-1 - Bed Surface Temperature Profiles with Varying Bed Depth and Bed Surface Convection Coefficient

Bed Depth [μm]	Temperature Scale [°C]	Bed Top Face Convection Coefficient [W/m^2-K]		
		10	20	30
200	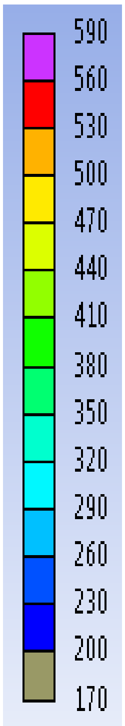		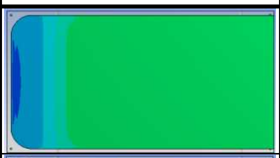	
400		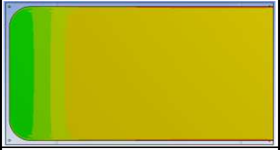	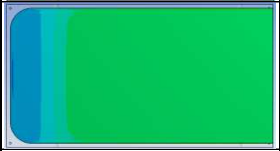	
600		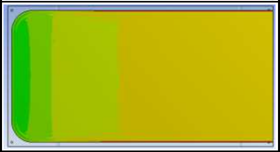		
800				
1000		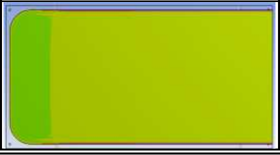	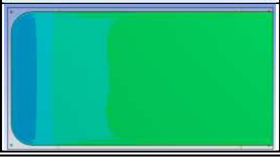	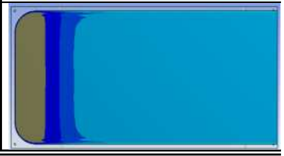

The convection coefficient has a significant effect on the temperature of a given bed, meaning that either power inputs will have to be tuned to an experimentally-derived convection coefficient, or, more easily, actively controlled to maintain a desired surface temperature. Controlling for temperature, it is of interest to maintain the isothermality of the reaction zone. This zone, illustrated in Figure 3.5 and which is to the right in the images in Table 3-1, shows substantially less temperature variation relative to the spreading zone. Both bed thickness and convection coefficient affect this gradient however. At the highest heat loss case, where the convection coefficient is 30 W/m^2-K, there is little variation in temperature profile between beds that are 200 μm thick and those that are 1 mm thick. As the convection coefficient decreases, thicker beds exhibit greater temperature variation in the reaction zone to the point where, at 20 W/m^2-K, only the 200, 400, and 600 μm beds exhibit similar temperature profiles in the reaction zone. Lowering the convection coefficient even further leads to an even greater change in profile, with both the 200 and 600 μm beds showing a substantial gradient in the reaction zone.

Therefore, in order to account for the possibility of a low convection coefficient, the bed height should be set by the spreader bars at, or around, 400 μm. This works out well, as the maximum experimental particle diameter is 425 μm [4], and so this height will be used to set bed depth. While the bed surface in all cases is not perfectly isothermal, modifications to improve the results would require significant additional thermal modeling and likely increased machining costs to improve the response.

3.4 Volatile Evacuation Model

While secondary reactions may occur in the pyrolysis vapor if not rapidly chilled, forming a different set of products, this does not generally occur at temperatures above the operating point of this reactor (400°C) [47]. The vapor can however condense on cooler surfaces such as the reactor walls and fume hood, throwing off the mass balance of a reactor run, and reducing the effectiveness of the radiation shield. It is imperative, therefore, that, in addition to heating the radiation shield, the pyrolysis gasses be evacuated from the chamber and into the condenser as rapidly as possible. Two pressure models were developed to determine the amount of time the vapor spends in the fume hood for a given pressure drop between the chamber and vacuum pump. The purpose of which was to determine the proper pump size rather than a detailed model of presure drop across the system.

The first model assumes laminar flow through a simplified version of the entire system. The second models individual pressure drops in each subsection of the gas line and allows for the possibility of turbulent flow. The equations used in this section are well known, and may be found in any undergraduate fluids text; for example: *Introduction to Fluid Mechanics* by Fox, McDonald and Pritchard [48].

In the first system, illustrated in Figure 3.6, it is assumed that laminar plug flow occurs in the fume hood, and that the flow continues into the draw pipe. It is assumed that the flow through the draw tube and condenser remains laminar. The time in the fume hood is determined from the estimated pressure drop across the system. First, the volumetric flow rate of the pyrolysis gas is determined using the following:

$$Q = \frac{\pi}{8}\frac{R^4}{\mu}\frac{\Delta P}{L_{sys}} \tag{3.8}$$

where μ is the viscosity of the gas, L_{sys} is the length of fume hood and the draw pipe, ΔP is the pressure differential across the system, and the hydraulic radius of the fume hood, R, is given as:

$$R = \frac{4xh}{2(x+h)} \tag{3.9}$$

where x is the length of the fume hood in the direction of granular flow and h is the height of the fume hood. The time spent passing through the system is given as:

$$\tau = \frac{L_{sys}}{v} \tag{3.10}$$

where the velocity is given as:

$$v = \frac{Q}{xh} \tag{3.11}$$

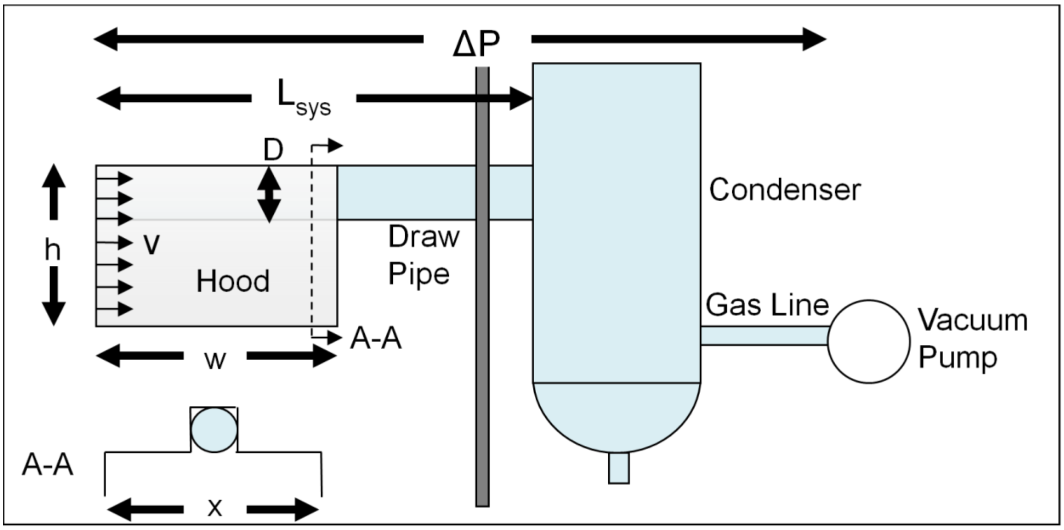

Figure 3.6 - Illustration of Condenser System and Associated Dimensions for First Gas Residence Time Model

In the second model, illustrated in Figure 3.7, instead of the time being derived from the pressure differential, the required pressure differential is determined from a specified reactor residence time. The gas extraction system is broken into four parts: the fume hood (1), the draw tube holes (2), the draw tube (3), and the gas line and condenser(4). Each section has an associated pressure drop that adds up to a required pressure differential. A time to pass through the fume hood is set, and an associated velocity at the mouth of the fume hood is determined by the following:

$$v_1 = \frac{L_{path}}{\tau_{hood}} \tag{3.12}$$

where L_{path} is the length of the flow path from the edges of the fume hood to the center of the holes drilled into the draw tube. For simplification this is set to be:

$$L_{path} = h + \frac{x}{2} \tag{3.13}$$

The cross-sectional area of the fume hood changes as the height increases, and so, for simplification, Bernoulli's equation is used to determine the pressure drop across the fume hood, such that:

$$\Delta P_1 = \frac{1}{2}\rho\left(v_2^{\,2} - v_1^{\,2}\right) \tag{3.14}$$

where, from conservation of mass:

$$v_2 = \frac{4}{\pi}\frac{xw}{nc^2} \tag{3.15}$$

where w is the width of the plate (and hence fume hood), n is the number of holes drilled into the downward face of the draw pipe and c is the diameter of these holes.

There is a small pressure drop as the vapor passes through the holes, given by:

$$\Delta P_2 = f\,\frac{\rho v_2^{\,2}\delta}{2c} \tag{3.16}$$

where δ is the thickness of the glass tubing, and the friction factor, f, is determined by the Reynolds number such that:

$$f = \frac{64}{\mathrm{Re}_2}, \quad \mathrm{Re}_2 \le 2300 \tag{3.17}$$

$$f = \frac{0.316}{\mathrm{Re}_2^{\,0.25}}, \quad 2300 < \mathrm{Re}_2 \le 10^5 \tag{3.18}$$

according to the Blasius correlation for smooth pipes. A similar pressure drop in the draw pipe is determined by:

$$\Delta P_3 = f\,\frac{\rho {v_3}^2 L}{2D} \tag{3.19}$$

where L is the length of the draw pipe, D is the inner diameter of the draw pipe. The friction coefficient is the determined in the same manner as before, where:

$$v_3 = \frac{nc^2}{D^2} v_2 \tag{3.20}$$

Finally, the pressure drop in the tube connecting to the condenser to the vacuum pump (as well as the condenser itself) must be determined. The bulk velocity through the vacuum line may not be determined by setting the volumetric flow rate into the condenser equal to the volumetric flow rate out, as both mass condenses out of the gas flow, and the gas decreases in temperature. Assuming ideal gas behavior, the specific volume of the gas is proportional to temperature, and hence density inversely proportional, such that:

$$\frac{v_{out}}{v_{in}} = \frac{\rho_{in}}{\rho_{out}} = \frac{T_{out}}{T_{in}} \tag{3.21}$$

Applying this density change, the mass flow rate, is assumed to follow the balance:

$$\dot{m}_{gas} = 0.3\dot{m}_{total}\,, \quad \dot{m}_{vols} = 0.8\dot{m}_{total} \tag{3.22}$$

where $\dot{m}_{vols}$ is the mass flow rate of the total volatiles, and so the gas volumetric flow rate passing out of the condenser is given by:

$$q = \frac{3}{8}\frac{QT_{out}}{\rho_{in}T_{in}} \tag{3.23}$$

The resulting velocity is hence:

$$v_4 = \frac{4}{\pi}\frac{q}{d^2} \tag{3.24}$$

where d is the diameter of the vacuum line. Pressure drop may be determined using the same method as before, with:

$$\Delta P_4 = f \frac{\rho_{out} v_4{}^2 \left(l + \pi \frac{K}{2} \right)}{2d} \tag{3.25}$$

where K is the diameter of the condenser.

For the more complex model condensation on the interior of the draw pipe must also be considered. The total residence time between the bed and the condenser is thus:

$$\tau_{total} = \tau_{hood} + \frac{\delta}{v_2} + \frac{L}{v_3} \tag{3.26}$$

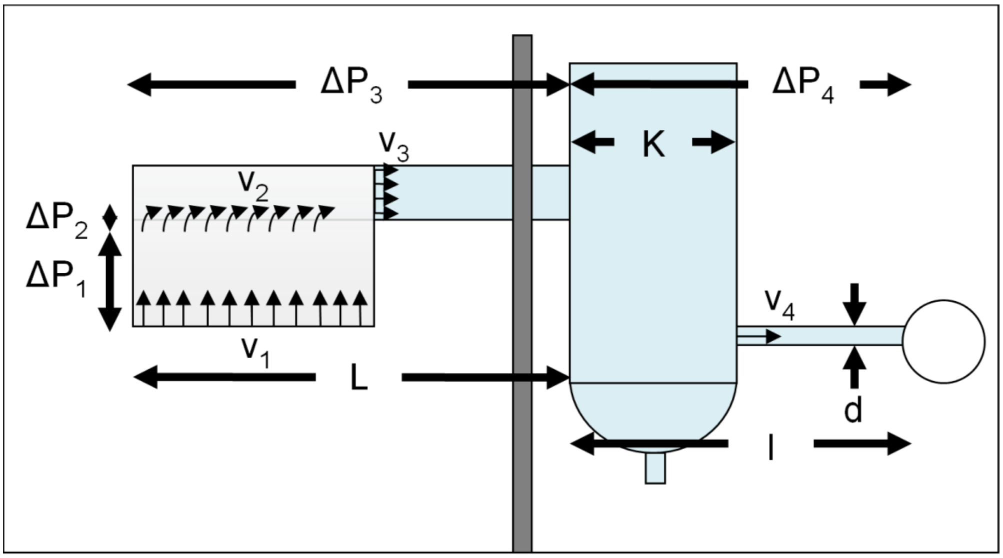

Figure 3.7 - Illustration of Condenser System and Associated Dimensions for Second Gas Residence Time Model

A comparison of the predictions of the two methods is illustrated in Figure 3.8.

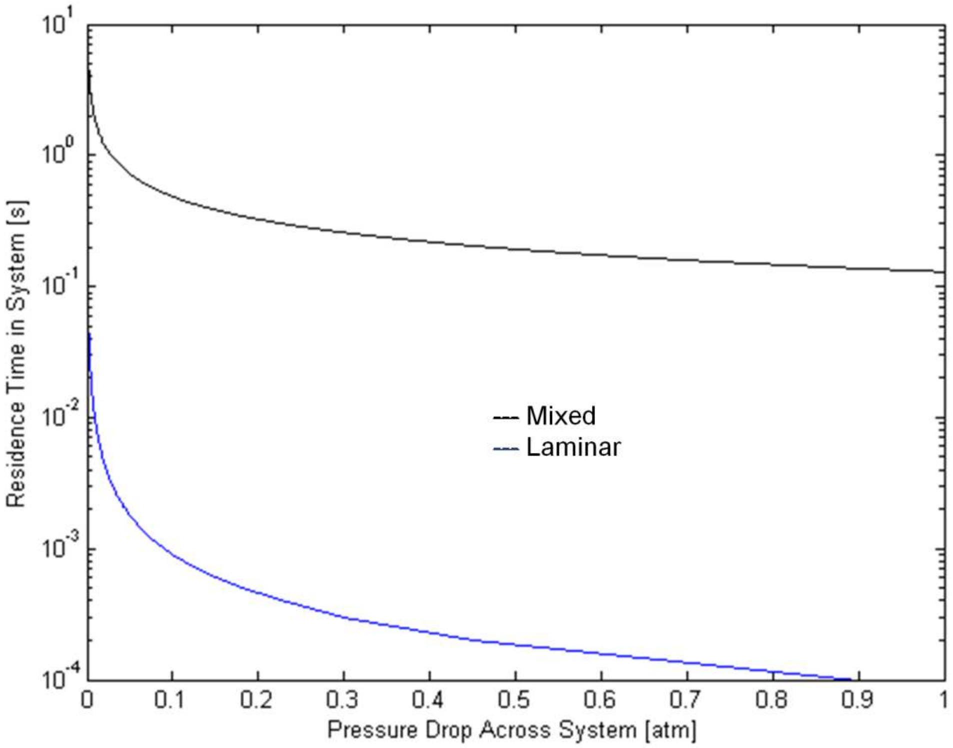

Figure 3.8 - Residence Time Before Reaching Condenser with Respect to System Pressure Differential

As is illustrated, the laminar flow model significantly underpredicts the system residence time with respect to the piecewise mixed flow model. Therefore, because it is more conservative, the piecewise model was used to drive pump sizing for experimentation. While even 0.05 atm is enough of a pressure differential to discourage prolonged contact with the radiation shield, it will be heated nonetheless to encourage a mild Raleigh-Taylor instability at the surface of the shield, creating a buffer zone protecting the surface from the majority of the vapor stream.

3.5 Condensation and Product Cooling

3.5.1 Evaluating a Potential Counterflow Condenser System

Two condenser systems were considered for pyrolysis reactor: a counterflow system and a dry ice trap. The behavior of both systems are well known, and may be found summarized in any undergraduate heat transfer textbook; for example: *Fundamentals of Heat and Mass Transfer* by Incropera, Dewitt, Bergman and Lavine [45]. The effectiveness of the counterflow condenser is given by the following:

$$\varepsilon_{counterflow} = \frac{1 - \exp[-NTU(1 - C_r)]}{1 - C_r \exp[-NTU(1 - C_r)]} \tag{3.27}$$

where the number of transfer units (NTU) is defined as:

$$NTU = \frac{UA_{mid}}{C_{\min}} \tag{3.28}$$

where U is overall convection coefficient, A_{mid} is the area of the midsurface of the condenser tube defined as the average of the condenser tube inner and outer surface areas, C_{min} is the minimum heat capacity rate, and the heat capacity ratio (C_r) is defined as:

$$C_r = \frac{C_{\min}}{C_{\max}} \tag{3.29}$$

Gas is treated as water vapor at average temperature of 275°C and the coolant is chilled acetone at -77°C

$$C_{\min} = f\dot{m}_g c_g \tag{3.30}$$

$$C_{\max} = f\dot{m}_{cool} c_{cool} \tag{3.31}$$

$$U = \left[A_{mid} \left(\frac{1}{h_g A_{in}} + \frac{R''_{f,g}}{A_{in}} + \frac{\ln(D_{out} / D_{in})}{2\pi kL} + \frac{R''_{f,cool}}{A_{out}} + \frac{1}{h_{cool} A_{out}} \right) \right]^{-1} \tag{3.32}$$

where A_{in} is the condenser tube inner surface area, A_{out} is the condenser tube outer surface area, $R''_{f,g}$ is the fouling factor of the gas, $R''_{f,cool}$ is the fouling factor of the salt water, D_{out} and D_{in} are the outside and inside tube diameters respectively, L is the length of the tube and k is the thermal conductivity of glass. The convection coefficients, h_i, must be determined by empirical models, and depend on the Reynolds number. The Reynolds number calculation used to determine whether flow is laminar is given in (3.33).

$$\mathrm{Re} = \frac{\rho u D}{\mu} \tag{3.33}$$

where ρ is the density of the fluid, D is the pipe diameter, μ is the viscosity of the fluid and u is the velocity of the fluid, which, from Bernoulli's relation, we may determine from our imposed pressure differential to be:

$$u = \sqrt{\frac{2\Delta P}{\rho}} \tag{3.34}$$

Treating the gasses as water vapor at 275°C and pipe diameter of 3.18 mm (0.125 in.) the Reynolds number will be less than 50000, dependant on the pressure differential imposed by the vacuum pump, assuming the pump is limited to a maximum pressure differential of one atmosphere. The corresponding Nusselt number for the gas will be determined based on whether the flow is laminar (Re<2300) or not. The Nusselt number describing the convection transfer from the pyrolysis gas is found, following conventional heat exchanger design, using a constant heat flux condition for laminar flow, and the Dittus-Boelter correlation for tube flows for turbulent flow [45].

$$Nu_g = 4.36, \quad \mathrm{Re} \le 2300 \tag{3.35}$$

$$Nu_g = 0.023\mathrm{Re}^{0.8}\,\mathrm{Pr}^{0.3}, \quad \mathrm{Re} > 2300 \tag{3.36}$$

In addition to the imposed pressure differential, the pyrolysis gas will experience a pressure drop due to fictional effects. These, for laminar and turbulent flows are given in (3.37) and (3.38).

$$P_{loss} = \frac{32\mu_g uL}{D^2}, \quad \mathrm{Re} \le 2300 \tag{3.37}$$

$$P_{loss} = f\,\frac{\rho u^2 L}{2D}, \quad \mathrm{Re} > 2300 \tag{3.38}$$

where L is the flow length between the hood and the condenser.

For the acetone:

$$\dot{V} \ge 0.1\frac{gal}{\min} \tag{3.39}$$

This fluid in the heat exchanger passes through a jacket pipe approximately 0.5" in diameter. Again, treating the flow as laminar:

$$Nu_{cool} = 4.36 \tag{3.40}$$

The resulting convection coefficients for each fluid (i) may be determined using:

$$h_i = \frac{Nu_i k_i}{D_i} \tag{3.41}$$

where k_i is the thermal conductivity of fluid i. Table 3-2 summarizes key values for a counterflow condenser for an imposed pressure differential of one tenth of an atmosphere.

Table 3-2 - Summarized Values of Counterflow Condenser with an Imposed Pressure Differntial of 0.1 atm

Variable	Value
h_g [W/m^{2}K]	702.4
h_{cool} [W/m^{2}K]	193.3
U [W/m^{2}K]	131.6
A [m^2]	0.01435
C_{min} [W/K]	0.20
C_{max} [W/K]	8.78
C_r [-]	0.0225
NTU [-]	9.56
$\varepsilon_{counterflow}$ [-]	0.999
P_{loss} [kPa]	51.8

3.5.2 Evaluating a Potential Dry Ice Trap Condenser

Dry ice traps are simpler than counterflow condensers. In such a system, dry ice is mixed into a liquid, often acetone, with a point at the sublimation temperature of the dry ice. Vapor then condenses on the outside of the container holding the dry ice slurry. Because the dry ice and acetone mixture is boiling C_{max} will be infinite leading to the following simplications:

$$C_{\min} = f\dot{m}_g c_g \tag{3.42}$$

$$C_{\max} = \infty \tag{3.43}$$

$$\varepsilon_{dry\ ice} = 1 - \exp\left(- NTU\right) \tag{3.44}$$

$$NTU = \frac{UA}{C_{\min}} \tag{3.45}$$

Not knowing the condensing area, and there being difficulty in calculating the convection coefficients, we log mean temperature difference will be used to determine the NTU value.

$$UA = \frac{f\dot{m}_g \left(c_g \left(T_H - T_C \right) + f_{cond} \Delta h_{vap} \right)}{\Delta T_{lm}} \tag{3.46}$$

$$\Delta T_{lm} = \frac{\left(T_{h,i} - T_{c,o} \right) - \left(T_{h,o} - T_{c,i} \right)}{\ln \left(\frac{T_{h,i} - T_{c,o}}{T_{h,o} - T_{c,i}} \right)} \tag{3.47}$$

The temperature of the dry ice mixture does not change, therefore:

$$T_{c,i} = T_{c,o} \tag{3.48}$$

Table 3-3 summarizes key values for a dry ice condenser for an imposed pressure differential of one tenth of an atmosphere.

Table 3-3 - Summarized Values of Dry Ice Condenser with an Imposed Pressure Differntial of 0.1 atm

Variable	Value
$T_{H,i}$ [°C]	550
$T_{H,o}$ [°C]	0
$T_{C,i}$ [°C]	-77
f_{cond} [-]	0.625
f [-]	0.333
ΔT_{lm} [°C]	263.7
NTU [-]	5.09
$\varepsilon_{dry\ ice}$ [-]	0.994

Comparing the dry ice trap and counterflow systems, the effectiveness of the single-pass shell and tube counterflow condenser is greater than that of the dry ice trap, but both exceed a 0.99 effectiveness value. It is easier to implement the dry ice trap system than the counterflow system as it does not require a refrigeration cycle, but will require occasionally refilling the condenser with dry ice. Therefore the dry ice trap was selected.

3.5.3 Char Catch Design

To prevent secondary reactions, the char should be cooled as quickly as possible. To achieve this, the char catch will be a finned heat sink. A fan will blow room temperature air across the exterior fins, removing heat from the char. Interior fins have also been considered, and will be added, such that they are oriented parallel to the direction of bulk mass flow along the surface of the reactor plate. This helps ensure that the char builds up evenly between all interior fins. To prove the usefulness of adding interior fins, consider the char catch models and associated resistance networks laid out in Figure 3.9.

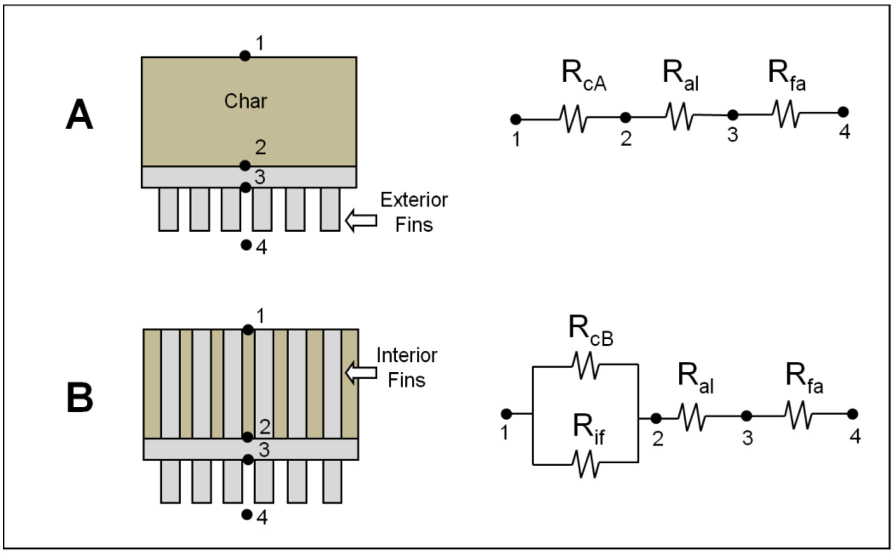

Figure 3.9 - Example Char Catch Designs and Associated Thermal Resistance Networks

Model A has no interior fins, and model B does. The resistances in their associated thermal resistance networks may be defined as follows:

$$R_{cA} = \frac{z_c}{A_T k_c} \tag{3.49}$$

$$R_{al} = \frac{z_{al}}{A_T k_{al}} \tag{3.50}$$

$$R_{fa} = \frac{1}{\eta_o h A_{fa}} \tag{3.51}$$

$$R_{cB} = \frac{z_c}{(A_T - NA_{cs})k_c} \tag{3.52}$$

$$R_{if} = \frac{z_{al}}{NA_{cs}k_{al}} \tag{3.53}$$

where the subscripts c, al, fa, and if indicate char, aluminum, the exterior fin array and the interior fins respectively. z is the depth of the char, or thickness of the aluminum plate that forms the bottom of the char catch, A_T is the total cross-sectional area of the char catch interior, k is the thermal conductivity of char or aluminum, A_{fa} is the surface area of the fin array, A_{cs} is the cross-sectional area of a single fin, h is the convection coefficient and N is the number of fins. η_o is the efficiency of the fin array, defined as:

$$\eta_o = 1 - \frac{NA_f}{A_{fa}}(1 - \eta_f) \tag{3.54}$$

where A_f is the surface area of a fin and η_f is the efficiency of a single fin, defined as:

$$\eta_f = \frac{\tanh(uL_C)}{uL_C} \tag{3.55}$$

where:

$$u = \sqrt{\frac{2(w_f + z_f)h}{w_f z_f k_{al}}} \tag{3.56}$$

$$L_C = L_f + \frac{z_f}{2} \tag{3.57}$$

where w_f is the width of the fin, z_f is the thickness of the fin and L_f is the length of the fin. And so the total resistance for each system is defined as the following:

$$\Sigma R_A = R_{cA} + R_{al} + R_{fa} \tag{3.58}$$

$$\Sigma R_B = \left(\frac{1}{R_{cB}} + \frac{1}{R_{if}} \right)^{-1} + R_{al} + R_{fa} \tag{3.59}$$

The heat extracted from the char is given by:

$$q = \frac{T_C - T_\infty}{\Sigma R} \tag{3.60}$$

where T_c is the temperature of the char entering the char catch.

For fins that are, on average, 0.08 m (3.13 in) wide, 3.175×10^{-3} m (0.125 in) thick and 0.0508 m (2 in) long on the exterior, an exterior temperature of 22°C, convection coefficient of 200 W/m^2-K, 9 fins, total cross-sectional area of area of 0.05806 m^2 (90 in^2) and char temperature of 550°C, Figure 3.10 illustrates the extractable heat with respect to char depth for the two arrangements.

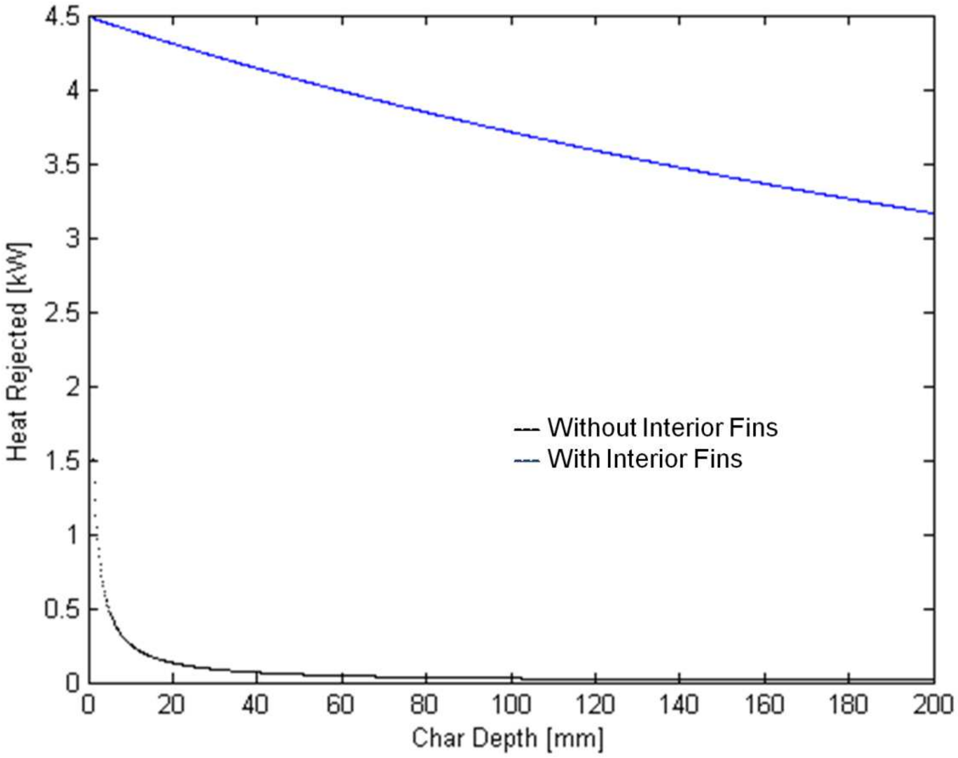

Figure 3.10 - Heat Rejection from Char Catch by Fin Arrays With and Without Interior Fins

The arrangement with interior fins (blue) rejects significantly more heat than the arrangement without interior fins (black). This largely due to the very low thermal conductivity of char, which is only 0.08 W/m-K. Interior fins are therefore a necessity in order to rapidly cool the char.

3.6 **Summary**

This chapter examined the relevant heat transfer models for continuous pyrolysis. Finite element analysis was performed to ensure isothermality in the reaction zone, and the critical bed depth for isothermal reaction determined. A model of volatile evacuation was presented. A cold trap condenser system was found to be nearly as effective as a counterflow condenser system and selected for ease of implementation.

CHAPTER 4

VIBRATORY TRANSPORT OF WOODY BIOMASS

4.1 Introduction

This chapter examines models for spreading woody biomass via vibration from an eccentric mass. Biomass is a poor thermal conductor and so in order to enable fast pyrolysis of the entire reactor load, the biomass needs to be spread into a thin layer. Dried biomass is fibrous and often carries a high static charge, causing particles to cling to one another and not spread in the same manner as other particulate matter, such as sand, would. An external force is required to overcome friction and static in order to achieve an even surface. Vibratory spreading, in which the surface underneath the biomass is excited at a constant frequency and amplitude is one such method. This chapter explores the use of vibratory spreading to both create an even layer biomass across the width of a plate, and to overcome static friction forces when inclined.

4.2 Review of Salient Literature

Granular flow is of great interest to the agriculture, mining, and construction industries, among others. In these, however, focus is generally on bulk gravity-driven flow. Studies [49-51] have been performed to measure the trajectories of seeds and fertilizer spread by agricultural equipment in order to model particle spreading and tune distribution for even spreading. While potentially useful, the length scales and velocities in such studies are too large to accurately measure individual particle behavior in vibratory spreading. Other groups [52-55] have attempted to characterize how columns of particulate matter collapse under the influence of gravity, what flow characteristics are experienced on the edges of the pile [53], and what effects the ambient environment has on the collapse [54]. These are greater concerns with high aspect ratio piles (those whose height exceeds their diameter), and in this system, buildup of particulate matter is largely low aspect ratio.

Work by Chelomey [56], further tested by Golovanevskiy [57], developed correlations for the bulk flow velocity of a vibrating inclined particle bed in which the velocity is defined as:

$$v = 0.7 X\omega_d \cos(\beta) \tag{4.1}$$

where X is the amplitude of vibration, ω_d is the driving frequency and β is the angle of the incline. This is assumed to be valid between 0° and 30°. From this the angle and drive frequency may be set such that a velocity, v, is acquired which satisfies the required mass flow rate and desired bed depth. The work also outlines a vibration overloading factor, w, to determine the state of the bed: whether the bed becomes fluidized, or if particles are ejected, etc.

$$w = \frac{X \sin(\beta)\omega_d^{\,2}}{g} \tag{4.2}$$

Vibro-fluidization typically occurs at overloading factors between 0.3 and 1, but can occur at lower overloading factors. Vibro-boiling, in which particles are ejected from the constraints of the bed, occurs at overloading factors greater than 1. It is imperative then, in order to ensure continuous heating, to keep the bed from experiencing vibro-boiling.

4.3 Vibratory Transport Model

The vibration model for the reacting plate may be treated as a mass sitting upon four spring-mass dampers, with an attached eccentric mass rotating about the vertical axis at some speed ω_d. The spring-mass dampers, or vibration isolators, are set at the corners of the reactor level and act in parallel. While only one vibration isolator is placed on each corner, the isolators act in both the X and Y directions. Additional damping may be added to stiffen the response in a desired direction, but this will not affect amplitude of the response in the other direction. The system model is illustrated in Figure 4.1 and Figure 4.2.

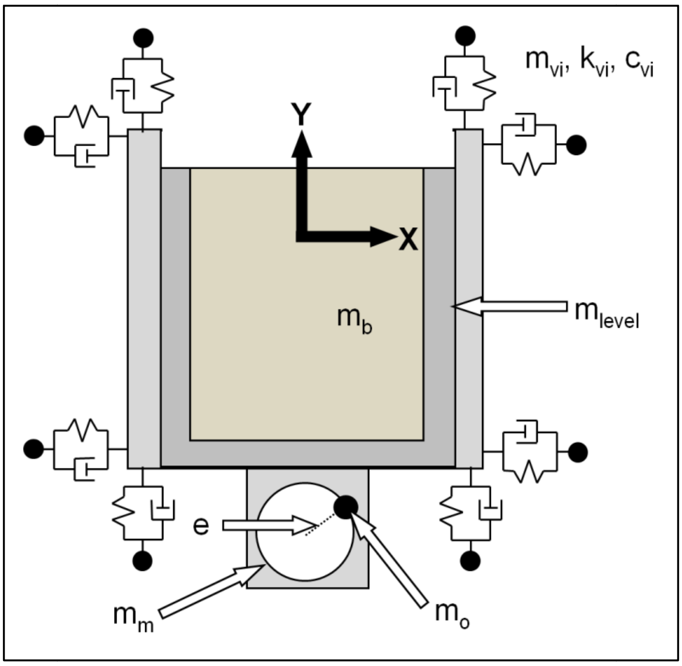

Figure 4.1 - Top View: Vibration Model

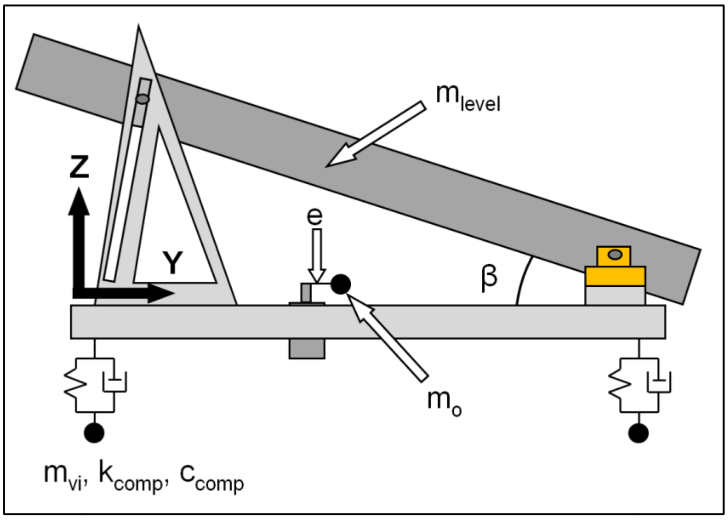

Figure 4.2 - Side View: Vibration Model

It is assumed that the underside of the vibration isolator is rigidly fixed to the tower, and that the tower itself is perfectly rigid. The minimum motor torque required is given as:

$$T_{\min} = T_{static} + T_{dynamic} \tag{4.3}$$

where T_{static} is the torque required to overcome the internal motor friction. This would also include resisting gravitational acceleration of the eccentric mass were the motor shaft not oriented perpendicular to the ground. $T_{dynamic}$ is the required torque to keep the motor spinning at the desired speed given as:

$$T_{dynamic} = F_r e \tag{4.4}$$

where:

$$F_r = m_o e \omega_d{}^2 \tag{4.5}$$

where e is the eccentricity of the mass and F_r is the resistive force that the motor must overcome. Because the eccentric mass is free, revolving in a plane perpendicular to the pull of gravity, the resistive force may be reduced to internal friction, and so will be treated as having no resistive force. Some torque is still required to bring the motor up to speed in a reasonable timeframe however. This torque is given by:

$$T_{dynamic} = I\alpha_d = \left(m_o e^2\right)\left(\frac{\omega_d}{t_{lead}}\right) \tag{4.6}$$

where I is the moment of inertia of the eccentric mass, α_d is the driving angular acceleration, m_o is the eccentric mass, and t_{lead} is the lead time necessary to bring the motor up to speed. The natural frequency of level vibration in the top plane, as can be determined using standard methods laid out in any introductory vibrations textbook (i.e. Inman [58]), is given as:

$$\omega_n = \sqrt{\frac{k_{eff}}{m_{tot}}} = \sqrt{\frac{Nk_{vi}}{m_{level} + m_o + m_b + \frac{N}{3} m_{vi} + m_m}} \qquad (4.7)$$

where k_{eff} is the effective spring stiffness of the vibration isolators, m_{tot} is the total mass of the level that is accelerated, N is the number of vibration isolators (the isolators act in parallel), k_{vi} is the shear stiffness of the vibration isolators, m_{level} is the mass of the inclined plate and support structure of the level resting on the vibration isolator, m_b is the mass of the biomass, m_{vi} is the mass of the vibration isolator and m_m is the mass of the motor. The one third represents the effects of grounding one end of the flexible vibration isolators, treating them as a bending spring. Note that the radial direction can be resolved into an X and Y component that, if no additional damping or stiffness is introduced, will exhibit the same response, only 90° out of phase with one another. From here on, this work will consider the response in the X direction.

To determine the displacement of the level we must solve the following differential equation:

$$(m_{tot} - m_o)\ddot{x} = F_r - c_{eff}\,\dot{x} - k_{eff}\,x \qquad (4.8)$$

where x is the displacement in the X direction, c_{eff} is the effective damping, which will be defined further on in the work. Solving this differential equation will yield a solution of the form:

$$x(t) = X \sin(\omega_d t - \theta) \qquad (4.9)$$

Solving the differential equation we obtain the amplitude of displacement of the bed and phase shift as:

$$X = \frac{m_o e}{m_{tot}} \frac{{r_x}^2}{\sqrt{\left(1 - {r_x}^2\right)^2 + \left(2\zeta r_x\right)^2}} \tag{4.10}$$

$$\theta = \tan^{-1}\left(\frac{2\zeta r_x}{1 - {r_x}^2}\right) \tag{4.11}$$

where r is the ratio between the drive and natural frequency, such that:

$$r_x = \frac{\omega_d}{\omega_{n,x}} \tag{4.12}$$

where $\omega_{n,x}$ is the natural frequency in the X direction, and ζ is the damping factor estimated, initially, to be 0.5, and is defined as:

$$\zeta = \frac{c_{eff}}{2\sqrt{k_{eff}\, m_{tot}}} \tag{4.13}$$

where, because the dampers are attached at four separate corners and therefore act in parallel, the effective damping is the following:

$$c_{eff} = Nc_x \tag{4.14}$$

The maximum acceleration of the level is given as:

$$\ddot{X} = X{\omega_d}^2 \tag{4.15}$$

The resulting force is given as:

$$F = m_{tot}\ddot{X} \tag{4.16}$$

Dividing this by N yields the maximum force absorbed by each isolator. The force on the shaft of the motor is the following:

$$F_{shaft} = m_o e {\omega_d}^2 \tag{4.17}$$

Using Chelomey's work for determining vibro-fluidization, the response characteristics of the flow may be estimated, and controllable parameters set to encourage vibro-fluidization while avoiding vibro-boiling. A high residence time on the shaker bed is desirable for effective fast pyrolysis. The residence time may be determined from the predicted velocity as:

$$t_{res} = \frac{x_{reaction}}{v} \tag{4.18}$$

where $x_{reaction}$ is the length of bed below the fine spreader.

A model of the system was programmed using MATLAB simulation software to simulate expected mass flow rate at different angles over a range of voltages. The expected mass flow rate for a bed that is 1 mm thick is presented in Figure 4.3 for angles between 10° and 20°.

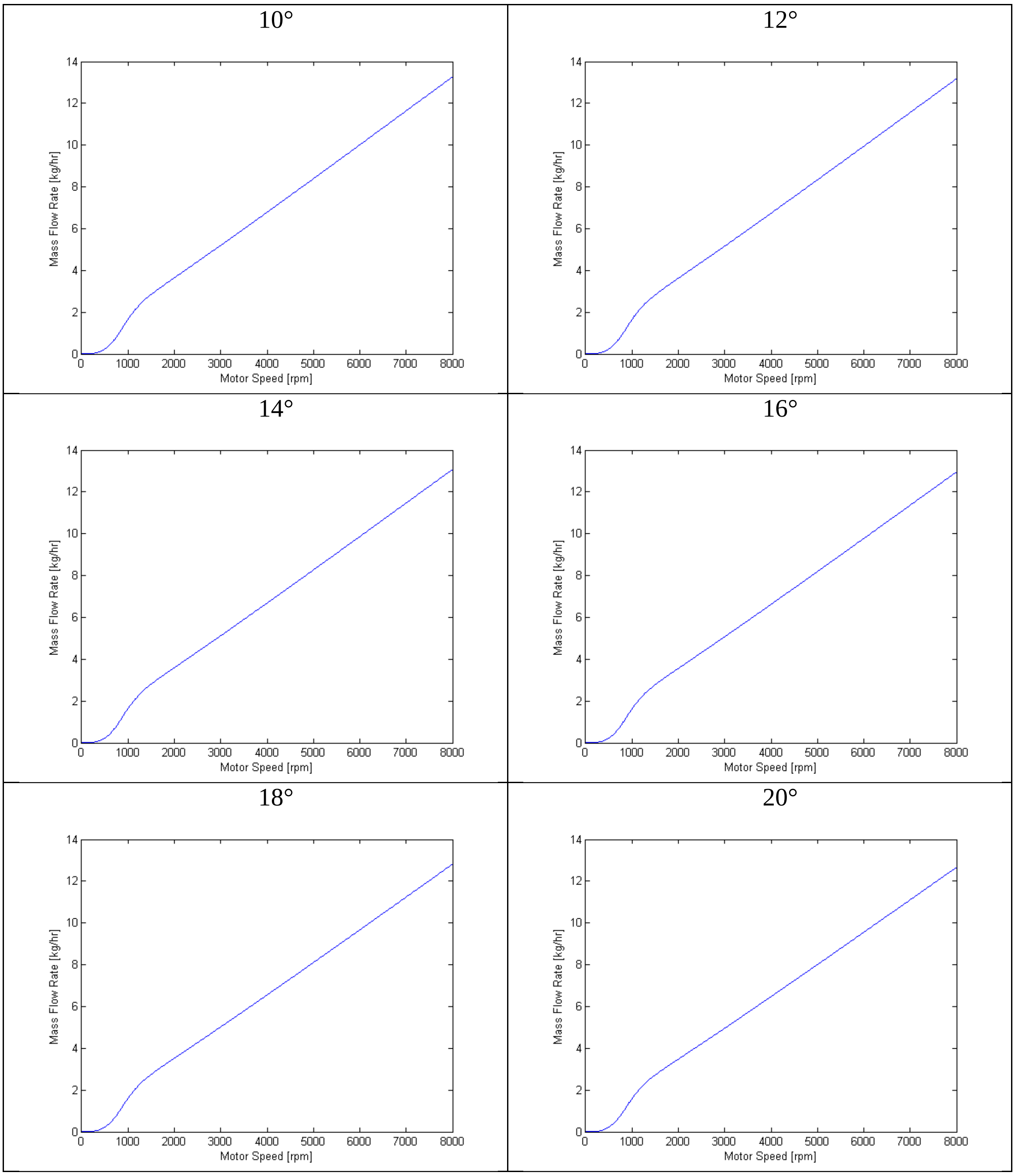

Figure 4.3 - Predicted Mass Flow Rates for an Example Plate Design Corresponding to Motor Speed at Varrying Plate Angles

As illustrated, the response is not expected to be strongly affected by changing the angle of the plate. The shape of the curve is heavily dependent on the damping ratio, a problem in modeling this system. The damping coefficient of the selected vibration dampers isn't explicitly stated, and must be determined experimentally. For example, Figure 4.4 details the comparison of mass flow rate responses between several damping ratios.

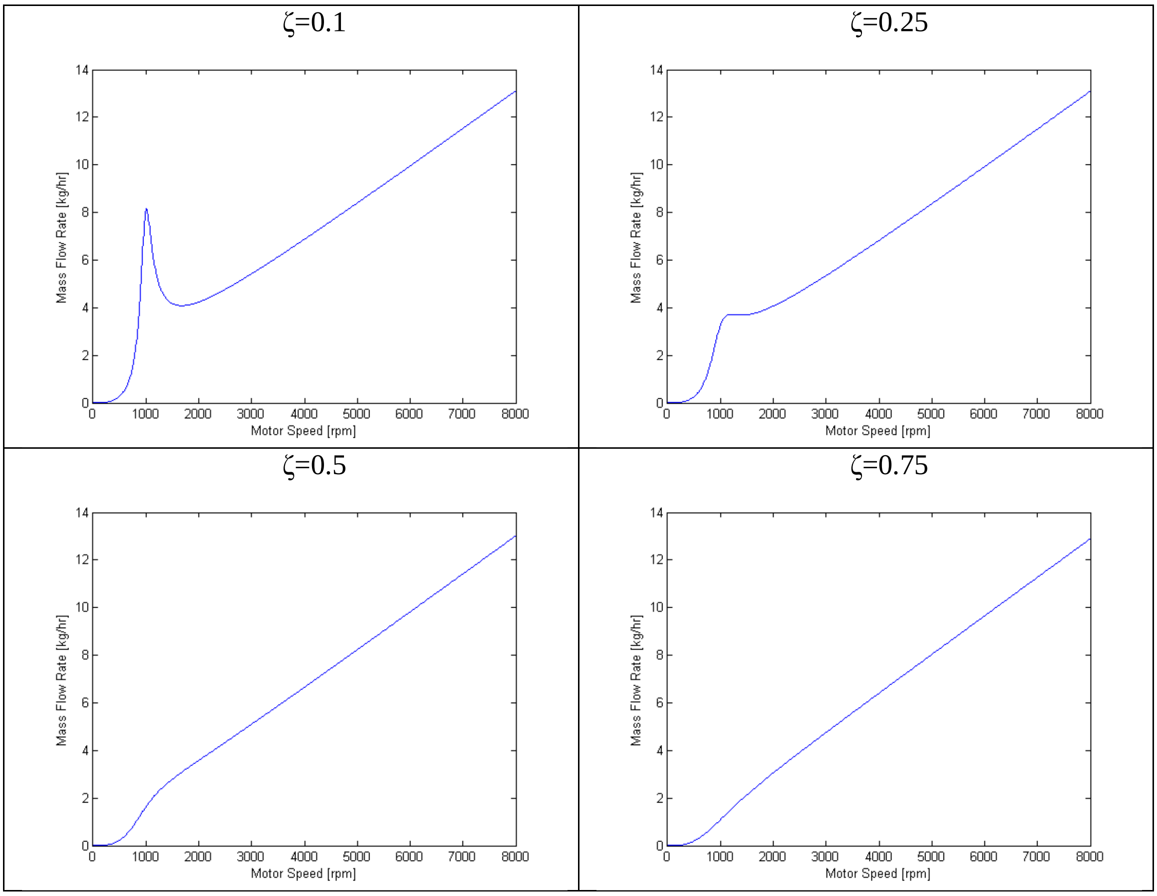

Figure 4.4 - Predicted Mass Flow Rates Corresponding to Motor Speed at Varying Damping Ratios at a Plate Angle of 15°

Damping ratio therefore has a significant effect on the magnitude of the response curve close to the resonant frequency of the system, and must be verified experimentally.

4.4 Kline-McLintock Error Analysis of Vibratory Spreading Model

It is important that uncertainty analysis be performed on the vibratory spreading model to ensure that it is as accurate as possible. A Kline-McLintock error analysis was performed to determine the maximum expected variance between the model and the experimental results. The uncertainty of several variables were calculated in order to determine the uncertainty in the mass flow rate. The uncertainty in the mass flow rate is given by the following:

$$w_{\dot{m}} = \sqrt{\left(\frac{\partial \dot{m}}{\partial X} w_X\right)^2 + \left(\frac{\partial \dot{m}}{\partial \omega_d} w_{\omega_d}\right)^2 + \left(\frac{\partial \dot{m}}{\partial \beta} w_\beta\right)^2 + \left(\frac{\partial \dot{m}}{\partial x} w_x\right)^2 + \left(\frac{\partial \dot{m}}{\partial z} w_z\right)^2 + \left(\frac{\partial \dot{m}}{\partial m_b} w_{m_b}\right)^2 + \left(\frac{\partial \dot{m}}{\partial D} w_D\right)^2 + \left(\frac{\partial \dot{m}}{\partial d} w_d\right)^2} \tag{4.19}$$

where the uncertainty in the amplitude of vibration is given by:

$$w_X = \sqrt{\left(\frac{\partial X}{\partial m_o} w_{m_o}\right)^2 + \left(\frac{\partial X}{\partial e} w_e\right)^2 + \left(\frac{\partial X}{\partial m_{tot}} w_{m_{tot}}\right)^2 + \left(\frac{\partial X}{\partial r_x} w_{r_x}\right)^2 + \left(\frac{\partial X}{\partial \zeta} w_\zeta\right)^2} \tag{4.20}$$

where the uncertainty in the total mass of the level is given by:

$$w_{m_{tot}} = \sqrt{\left(\frac{\partial m_{tot}}{\partial m_{level}} w_{m_{level}}\right)^2 + \left(\frac{\partial m_{tot}}{\partial m_o} w_{m_o}\right)^2 + \left(\frac{\partial m_{tot}}{\partial m_b} w_{m_b}\right)^2 + \left(\frac{\partial m_{tot}}{\partial m_{vi}} w_{m_{vi}}\right)^2 + \left(\frac{\partial m_{tot}}{\partial m_m} w_{m_m}\right)^2} \tag{4.21}$$

and the uncertainty in the frequency ratios is given by:

$$w_{r_x} = \sqrt{\left(\frac{\partial r_x}{\partial \omega_d} w_{\omega_d}\right)^2 + \left(\frac{\partial r_x}{\partial \omega_n} w_{\omega_n}\right)^2} \tag{4.22}$$

The uncertainty in the natural frequency is given by:

$$w_{\omega_n} = \sqrt{\left(\frac{\partial \omega_n}{\partial k_{vi}} w_{k_{vi}}\right)^2 + \left(\frac{\partial \omega_n}{\partial m_{tot}} w_{m_{tot}}\right)^2} \tag{4.23}$$

and the uncertainty in the driving frequency, which is a function of voltage applied to the shaker motor, is given by:

$$w_{\omega_d} = \frac{\partial \omega_d}{\partial V} w_V \tag{4.24}$$

The uncertainties for the measured values are summarized in

Table 4-1.

Table 4-1 - Uncertainies of Base Variables in Vibratory Transport Model

Measured Variable	Uncertainty
Plate length ($x_{reaction}$)	1.27E-5 m
Plate width (y)	1.27E-5 m
Motor input voltage (V)	0.1 V
Plate angle (β)	0.5°
Mass of biomass (m_b)	1.16E-4 kg
Level mass (m_{level})	0.01 kg
Vibration isolator mass (m_s)	1.91E-4 kg
Eccentric mass (m_o)	1E-5 kg
Motor mass (m_m)	1E-5 kg
Eccentricity (e)	0.001 m
Damping ratio (ζ)	0.018
Vibration isolator stiffness (k)	500 N/m
Test sample deposit diameter (D)	1.39E-4 m
Test sample deposit depth (d)	1.65E-4 m

Applying this error analysis to the model, an envelope of expected results is obtained. Figure 4.5 illustrates the expected mass flow rate alongside the upper and lower bounds.

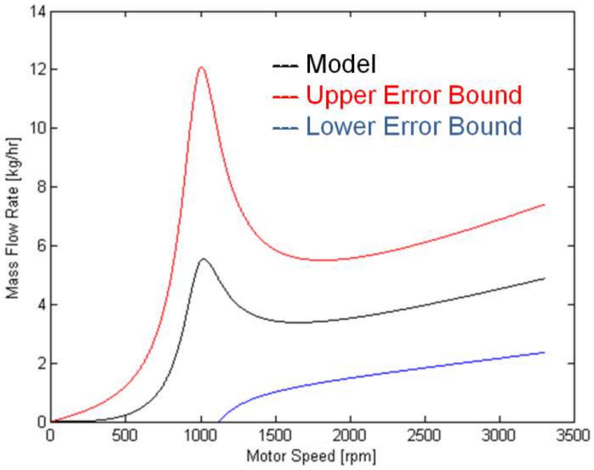

Figure 4.5 - Predicted Mass Flow Rate from Part Specifications for Transporting Loblolly Pine at a 16° Plate Angle

4.5 Analytical Determination of Char Trajectory

The char resulting from pyrolysis must be collected in a single receptacle to ensure the most accurate possible mass balance of the system. Therefore, determining the trajectory of the char particles, i.e. determining how far a particle will travel before reaching the mouth of the char catch, is important. While not realistic, to present a worst case scenario, the plate will assumed to be flat in order to maximize range for a given char ejection velocity.

The char falls off the end of the plate, but assuming no drag, particles will not travel far as they are ejected. Under this assumption, particle range may be equated from the following force balances:

$$ma_x = 0 \qquad ma_y = -mg \tag{4.25}$$

This leads to the following expression of the particle range:

$$x = v_o\sqrt{\frac{2y_o}{g}} \tag{4.26}$$

where v_o is the velocity of the char leaving the plate in the horizontal direction, y_o is the height of the plate lip above the char catch and g is the gravitational constant

This projection is likely grossly inaccurate, however, as drag on the blunt object with a mass less than a picogram will have a significant effect on it. For a rectangular solid ejected into gas the force balance reduces to:

$$ma_x = -\frac{1}{2}C_{D,x}\rho_g A v_x{}^2 \qquad ma_y = \frac{1}{2}C_{D,y}\rho_g A v_y{}^2 - mg \tag{4.27}$$

this further reduces to:

$$a_x = -\frac{1}{2l}C_{D,x}\frac{\rho_g}{\rho_c}v_x{}^2 \qquad a_y = \frac{1}{2h}C_{D,y}\frac{\rho_g}{\rho_c}v_y{}^2 - g \tag{4.28}$$

where ρ_g is the density of the gas, ρ_c is the density of the char and is approximately one tenth of the density of the unreacted wood [59], l is the length of the particle (the dimension in line with the x-axis), h is the thickness of the particle (the dimension in line with the y-axis), and C_D is the coefficient of drag in the specified direction. This, for a small rectilinear particle, as given by the correlation developed by Haider [60] is:

$$C_{D,i} = 24\left[1 + \exp\left(2.329 - 6.458\varphi + 2.449\varphi^2\right)\mathrm{Re}_i^{(0.557\varphi - 0.904)}\right] + \frac{\mathrm{Re}_i \exp\left(4.905 - 13.894\varphi + 18.422\varphi^2 - 10.26\varphi^3\right)}{\mathrm{Re}_i + \exp\left(1.468 + 12.258\varphi - 20.732\varphi^2 + 15.886\varphi^3\right)} \quad (4.29)$$

where Re_i is the Reynolds number in the ith direction of the particle movement, such that:

$$\mathrm{Re}_i = \frac{u_i L_i}{\nu} \quad (4.30)$$

where u_i is the velocity in the ith direction, ν is the kinematic viscosity of the air and L_i is the characteristic length of the particle (l in the x-direction, h in the y-direction). φ is a term used to correlate the behavior of a rectilinear particle to a spherical one and is defined such that:

$$\varphi = \frac{S_{sphere}}{S_{particle}} \quad (4.31)$$

where S_{sphere} is the surface area of a sphere with the same volume as the particle, and $S_{particle}$ is the surface area of the particle. For simplicity it was assumed that the Reynolds numbers, which at all times are well inside the laminar flow range, were constant with u_x equal to $v_o\cos(\beta)$, and Re_y equal to 10.

Returning to the force balance, the x and y velocities of the particle become solvable in terms of time. After solving the ordinary differential equations of velocity the following relations are determined:

$$u_x(t) = \frac{2v_o\rho_c l}{2\rho_c l + v_o\rho_g C_{D,x} t} \quad (4.32)$$

$$u_y(t)=\left(\frac{2g\rho_c h}{\rho_g C_{D,y}}\right)^{\frac{1}{2}}\frac{1+\exp\left(\sqrt{\dfrac{g\rho_c C_{D,y}}{2\rho_g h}}\right)}{1-\exp\left(\sqrt{\dfrac{g\rho_c C_{D,y}}{2\rho_g h}}\right)} \qquad (4.33)$$

Solving for x and y, a time t that satisfies y(t) = 0 is found where:

$$y(t)=\frac{2\rho_c h}{\rho_g C_{D,y}}\left[\sqrt{\frac{g\rho_g C_{D,y}}{2\rho_c h}}t-2\ln\left(\exp\left(\sqrt{\frac{g\rho_g C_{D,y}}{2\rho_c h}}t\right)-1\right)\right]+y_o \qquad (4.34)$$

Taking this time and applying it to the range equation, the ejected particle range can be modeled using the following:

$$x(t)=\frac{2\rho_c l}{\rho_g C_{D,x}}\ln\left(\frac{2\rho_c l+v_o\rho_g C_{D,x}t}{2\rho_c l}\right) \qquad (4.35)$$

Expected particle mass probability function, and the correlating expected particle ejection range at those masses, are plotted in Figure 4.6 for a sample design where particles leave the plate at 1 m/s, 0.5m above the mouth of the char catch.

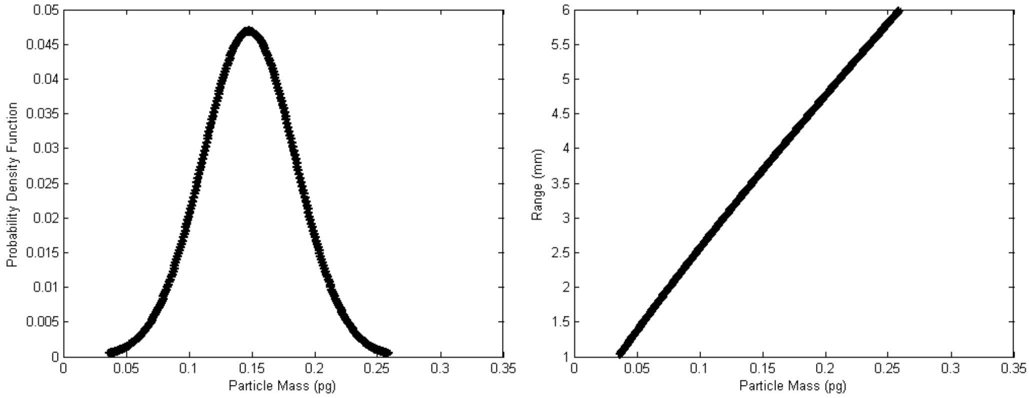

Figure 4.6 - Particle Mass Probability Function and Expected Ejection Range (0.1 m Plate Height and 1 m/s Ejection Velocity)

As is clearly illustrated in Figure 4.6, even assuming a high ejection velocity in the conservative model, the predictions from the no drag case are significant overestimates, as the mean char particle will not travel more than 3.5 mm.

4.6 Summary

In this chapter a model for vibratory transport was presented for ground loblolly pine. The model was used to predict, assuming full spreading, residence time and bulk mass flow rate. A char particle trajectory model was developed to ensure that char could be easily collected and cooled.

CHAPTER 5

REACTOR CONSTRUCTION AND COMMISIONING

5.1 Introduction

This chapter focuses on the construction of the reactor, evaluation of the heat transfer and vibratory transport models, and evaluation of the mass balances derived from commissioning tests of fast pyrolysis of *Pinus taeda*. A brief discussion of pyrolysis kinetics is introduced. Steady state heat transfer tests were run at 1000 W power input to determine the accuracy of the heat transfer model. Vibratory transport testing was run over a range of plate angles and excitation frequencies to determine the accuracy of the vibratory transport model. Commissioning tests tested four temperature and residence time combinations spread over the kinetics model curves. Mass yields are compared to two-component kinetics models developed through earlier work using the microreactor, and the departure from those results discussed.

5.2 Reactor Fabrication and Assembly

5.2.1 Reactor Superstructure Design

The main structure of the reactor is the heating tower. This is a 55.88 cm (22”) tall box frame essentially centered in the middle of the reactor chamber. Its footprint is 30.80 cm (12.125") by 25.40 cm (10"). The tower is used to support the reaction level and radiation shield. The rails that make up the tower are cut from slotted 2.54 cm (1") square frame material, allowing the heating level to move up and down to an appropriate height. There is space on the tower for three such heating plates, in order that fractionated pyrolysis experiments may be run in the future. The current design only supports a single reaction level.

The heating tower is bolted to the floor of the reactor which is made from a 1.27 cm (0.5") thick plate of aluminum, providing a sturdy mount for the heating tower. Towards one end of the tower, a circular hole, 20.32 cm (8") in diameter, is ringed by a bolt pattern. This hole is centered under one of the 25.4 cm (10") long crosspieces of tower and serves as the mounting point for the char catch. The crosspiece that would, if left in place, obstruct some of the char catch opening is removed, leaving the heating tower with eleven total struts.

Surrounding this assembly is a welded 304 14-ga flanged stainless steel canister. The top flange has a bolt pattern inscribed in it, allowing a circular 1.27 cm (0.5") thick plexiglass lid to be mounted to it. The bottom flange sports an identical pattern of through holes, allowing the canister to be bolted to a matching bolt pattern machined into the aluminum floor of the reactor. Three 6.35 cm (2.5") diameter holes have been cut into the wall of the canister along a vertical axis. These serve as ports for the condenser draw pipe to pass through for each stage of a fractionated pyrolysis setup. For single stage operation, the center hole is used, and the other two are plugged.

The aluminum base plate is elevated off the ground on a 60.96 cm (2 ft) cubic frame made from 2.54 cm (1”) slotted aluminum tubing. This provides clearance for the char catch. The catch is an aluminum cylinder that has an inner diameter of 20.32 cm (8"), an outer diameter of 22.86 cm (9") and a length of 27.94 cm (11"). A flange bolted to one end of the cylinder allows the experimenter to bolt the cylinder into the previously described pattern in the floor of the reactor. A 1.27 cm (0.5") thick and 22.86 cm (9") diameter disc of aluminum had nine 0.48 cm (3/16") deep slots machined into both sides of it with a 0.3175 cm (1/8") tool, and a countersunk through hole pattern drilled into it at

21.59 cm (8.5") in diameter. On the countersunk side, 0.3175 cm (1/8") thick fins of 5.56 cm (2-3/16") in length with welded into the slots. Similarly, on the other side, 25.88 cm (10-3/16") fins were used. This disc was slid into the char catch cylinder with the longer fins facing in, and bolted into the free end of the cylinder. The fins are aligned such that they are parallel to the flow path of material passing through the reactor. This allows, assuming even spreading across the reaction level, the char to settle evenly across the width of the fin array. Though aluminum is slightly reactive in the presence of activated carbon, the light layer of aluminum oxide that formed while the char catch was under construction was assumed to be sufficient to prevent secondary reactions between the char and the aluminum. The assembled char catch is pictured in Figure 5.1.

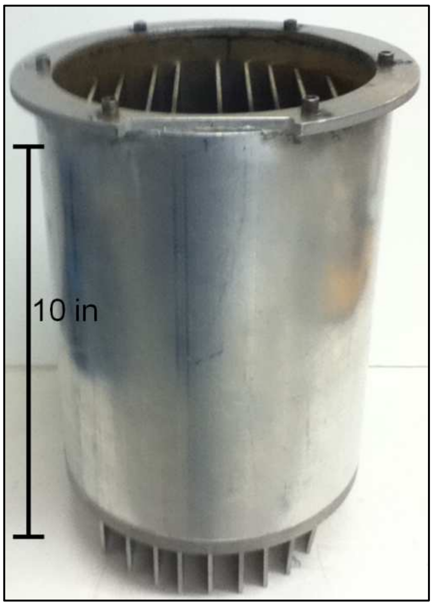

Figure 5.1 - The Assembled Char Catch

A pair of fans hangs from support pieces attached to one of the top rails of the box frame. These hang to such a level as to blow across the exterior fins of the char catch, enhancing char cooling and helping to prevent secondary reactions within the char.

Bracing another side of the box, three adjustable 2.54 cm (1") square slotted tube support struts are aligned vertically. Each of these is outfitted with a 0.64 cm (0.25") thick aluminum platform, supported on three brackets connecting them to the support struts. These platforms are height-adjustable, and are used to support a 500 mL Erlenmeyer flask and condenser for each fractionated pyrolysis level. For single stage use, all of the platforms are brought to the same height, and a support block with upward-facing rubber feet is used to support an aluminum spill tray underneath a 2000 mL Erlenmeyer flask supporting a condenser. The box frame, in order to move the reactor easily, is mounted on 10.16 cm (4") casters on its corners.

5.2.2 Reaction Plate Design and Manufacturing

The heater plate is machined from a block of 304 stainless steel as it exhibited sufficient corrosion resistance for a reacting surface. While another grade, such as 316 ("marine grade") might have been a better choice for preventing secondary reactions, 304 stainless was both easier to machine and considerably cheaper. A 2.54 x 21.59 x 41.91 cm (1" x 8.5" x 16.5") blank was cut from a block of stainless steel using a water jet, and the edges cleaned on a milling machine. A 30.48 x 17.78 cm (12" x 7") pocket was machined into one side of the plate to a depth of 1.27 cm (0.5") using a 1.27 cm (0.5") carbide end mill and a 6.35 cm (2.5") face mill. On the opposite face, a pocket with one open end, 40.64 cm by 20.32 cm (16" by 8"), was machined to a depth of 0.64 cm (0.25"). This would serve as the reacting surface. Four holes were drilled into the surface and tapped to accommodate the spreader bars. The reacting surface was then polished to an average surface roughness of 149±54 μm using a combination of sharpening stones and scotchbrite pads. A pair of holes was drilled into each long side of the reacting plate at a height of 1.27 cm (0.5”) from the topmost surface of the plate. The first, located towards the downstream side of the reacting surface, was a 0.635 cm (0.25”) diameter hole drilled to a depth of 2.54 cm (1”) and would be the anchoring point for a pivoting pin, connecting the reacting plate to the H frame, and constraining it translatively. The second hole was tapped to accommodate a 1/4-20 bolt, which would be tightened to fix the angle of the plate.

A pair of spreader bars were cut from 0.64 x 0.64 cm (0.25”x0.25”) 304 stainless steel stock, and one surface of them was machined flat. Two thru holes for #6 bolts were drilled through each, perpendicular to the flat side. These holes were aligned with the tapped holes in the reacting surface of the heating plate, and a bolt and washer setup used to orient the bars as herringbone spreaders.

A pair of 15.24 x 17.78 x 1.27 cm (6”x7”x0.5”) heating blocks were machined from 145, or “machinable”, copper. Four 8.26 cm (3.25”) deep 1.27 cm (0.25”) holes were drilled into the shorter sides, two per side, of each block to accommodate cartridge heaters. In one block, four 200 W cartridge heaters were added, and in the other: two 200 W cartridge heaters and two 100 W cartridge heaters, with one of each being placed into each side with like cartridge heaters aligned on the same drill path. These blocks were press fit into the pocket on the underside of the heating plate. As the steel portion of the plate was more massive on the spreader side, the block with all 200 W cartridge heaters was placed upstream. The second block was oriented so that the 100 W cartridge heaters were the most downstream heaters, as the least mass to be heated was downstream. Several layers of fiberglass backing were placed over the blocks, and a 304 stainless steel sheet bolted to the reacting plate underside was used to hold them in place. The cartridge heaters were wired in parallel.

Three more holes were drilled into the reacting plate, two in the long side, and one in the short. One on the long side, and the one on the short side were tapped so as to receive an accelerometer which would be used to characterize the forced response of the reacting surface. The third was left free as a mounting point for a grounding cable for the plate.

The heating plate pivots on an aluminum H-frame which mounts to the heating tower. This frame is composed of four major structural pieces, two which run parallel to the tower struts in the flow direction and two cross pieces that form an H-like shape when viewed from the top. A plate with a 10158 rpm 12 V DC motor mounted to it is bolted to these cross pieces, overlapping a portion of one of the longer pieces. An eccentric mass is attached to the motor shaft, providing a variable energy input source. A set of 1.27 cm (0.5") standoffs were mounted to the front and back of the frame. On top of these a layer of aerogel insulation was added. On the two on the downstream side, a brass pivot point was added, which, when fitted with a stainless steel pin, allowed the reacting plate to pivot between -5 and 20°. On the upstream standoffs, waterjetted aluminum parts provided an arced slot through which a 1/4-20 bolt may be passed. This allowed the experimenter to set the angle of the plate, and lock it in place. A layer of fiberglass insulation was placed between the aluminum support piece and the reacting plate. The frame itself was mounted on four rubber dual-stud vibration isolators, which were attached, on their underside, to the heating tower via four brackets mounted to two additional cross struts. This stiffened the tower while allowing the reacting stage to move vertically independently to it. Side and top views of the assembled reaction plate are pictured in Figure 5.2 and Figure 5.3.

Figure 5.2 - Side View of Reactor Plate Assembly

Figure 5.3 - Top View of Reactor Plate Assembly

5.2.3 Feed System Design and Manufacturing

The reactor must be continuously fed to meet the stated design objectives; therefore a feed system was design to accommodate this. The feed system is a combination of gravity and rotary feed. A hopper with a volume of 12671 cm^3 (773.2 in^3), sufficient for 3 kg of ground *Pinus taeda*, was fitted into a vertical hole drilled through a feed mechanism block. The block has a horizontal hole through its center, in which a feed cylinder is mounted. The cylinder, which is sealed off from the outside environment using two teflon bushings, has two slots machined into it, which can hold 0.969 cm^3 (0.059 in^3) of ground biomass each. A DC motor directly drives the cylinder, continuously dropping biomass down onto the vibrating plate below. The frequency of this rotation is matched to the mass flow rate that may be achieved on the pipe such that:

$$\omega = \frac{\dot{m}_{bed}}{2\rho_b \forall_{slot}} \tag{5.1}$$

A stirrer is also mounted in the lid of the hopper, allowing the biomass to be stirred, so that it doesn't stick to the walls of the hopper. The hopper itself is supported by a modified length of 30.48 cm (12 in) duct which was added after testing found that vibration of the frame caused the hopper to work loose from the feed mechanism block. The assembled hopper in and out of its support duct is pictured in Figure 5.4.

Figure 5.4 - Hopper Assembly Free From and Supported by Modified Duct

5.2.4 Condenser and Gas System Design

The gas system is broken into three major components: the purge gas system, volatile draw and condenser system, and the non-condensables line. In order to provide an inert environment for the pyrolysis reaction to take place in, a purge gas must be pumped into the canister. Four ports in the lid of the canister provided a method of filling the system with nitrogen, and help to prevent condensation on the reactor lid. The ports were spaced such that the gas flowed into the canister near its sides so that it would fill from the outside-in and so that it would not disturb the particles on the reaction plate. The gas delivery system ports and the gas line from the nitrogen tank are pictured in Figure 5.5.

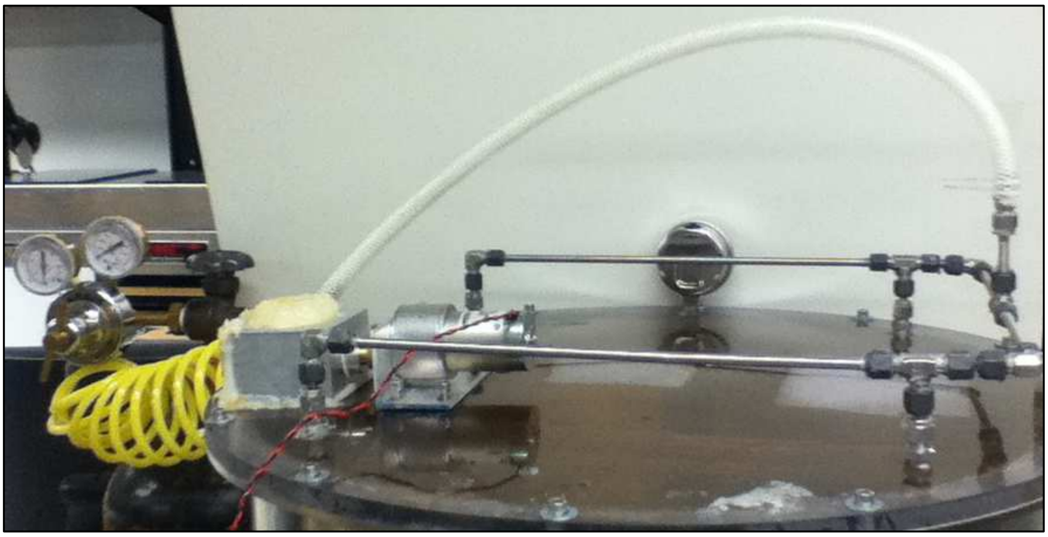

Figure 5.5 - Purge Gas Line and Delivery System

During reactor operation, the purge gas was used to carry the pyrolysis gas into the condenser. A 5.08 cm (2") diameter pipe with an outer 55/50 Standard Taper Joint was fused to an H.S. Martin dry ice trap condenser. A corresponding inner joint was fused to a second 40.64 cm (16”) long, 5.08 cm (2") diameter pipe with a closed end. Fourteen 1.91 cm (3/4") holes were drilled into the downward-facing side of this pipe along a width of 30.48 cm (12"). The pipe, hereafter referred to as the "draw tube," is pictured in Figure 5.6, and as part of the primary condenser assembly in Figure 5.7.

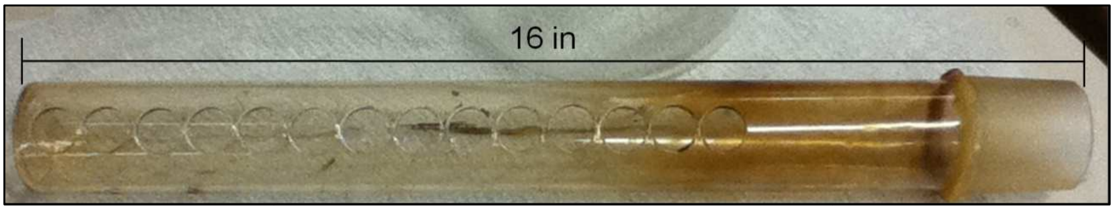

Figure 5.6 - Draw Tube Exhibiting Residual Tar Formation near the Condenser Connection Joint

Figure 5.7 - Primary Condenser Assembly

The draw tube was passed through one of the holes in the canister so that the holes were centered over the reacting plate. A bent 20-ga polished aluminum fume hood was fitted into the main struts of the heating tower, and lowered so that the hump in the hood fit over the gas collection pipe. The fume hood heaters, which are placed further out on the fume hood, therefore ensure a negative temperature gradient towards the center of the hood, encouraging flow inward via a larger Taylor flow boundary near the edges. The fume hood is pictured in Figure 5.8.

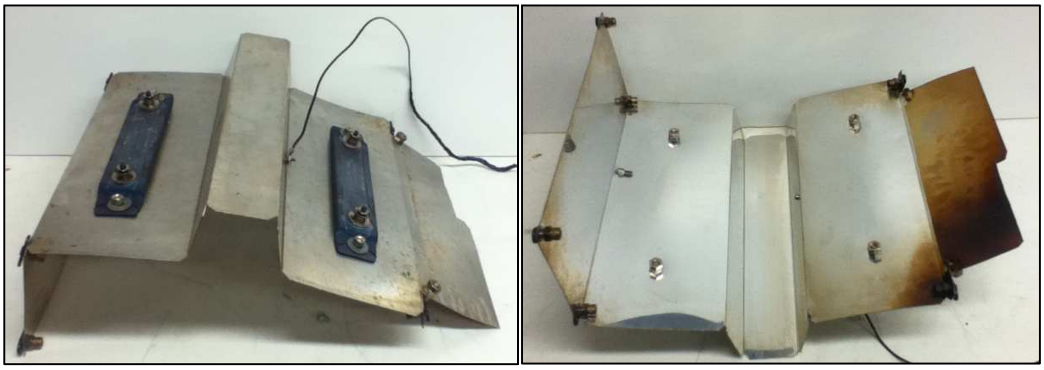

Figure 5.8 - Top and Underside Views of the Polished Aluminum Fume Hood, Note the Tar Formation on the Upstream Side of the Hood

This hood was heated to between 200°C and 220°C depending on the test, using a pair of Omega strip heaters to develop a Raleigh-Taylor boundary layer between the heated nitrogen close to the hood surface and the gasses in the reaction chamber, wherein the nitrogen becomes trapped at the surface of the hood, protecting the surface from tar deposition. The boundary results from a Raleigh-Taylor instability. The fume hood heaters, which are placed out from the center of the fume hood, ensure a negative temperature gradient towards the center of the hood, encouraging a larger Taylor flow boundary near the fume hood edges. This helped to direct the flow up the sides of the fume hood and into the draw pipe, while simultaneously discouraging condensation on the surface of the hood.

The mixture of pyrolysis gas and nitrogen was then drawn into the dry ice trap where the condensable gasses accumulated on the condenser walls and drained into the attached Erlenmeyer flask. A secondary 500 mL Erlenmeyer flask was connected to the top of the condenser using a pair of gas sampling connectors. The gas sampling connectors constrict the flow to force non-condensed volatiles to condense on the room temperature glass rather than in the vacuum pump. The flask collects heavier liquids that form just after the condenser, and includes a J-type thermocouple used for monitoring the temperature of the gasses passing out of the condenser. The assembly mates with the condenser via a standard taper joint, and is supported by a ring stand. The secondary assembly is pictured in Figure 5.9.

Figure 5.9 - Secondary Flask Assembly Free Standing and Attached to the Condenser Assembly

The remaining non-condensable gasses were pulled through a port in the top of the condenser by a vacuum pump. The pump was set to draw a slight vacuum of 90 kPa absolute pressure across the system, which was set by a ball valve. The gasses were released into a fume hood.

5.3 Reactor Operation

The continuous pyrolysis reactor is designed to be easy to use and not require regular user input once the pyrolysis reaction has started. For complete step by step instructions on reactor operation, refer to Appendix A. J-type thermocouples were connected to a National Instruments (NI) DAQ-9162 thermocouple reader. One J-type surface thermocouple was mounted to the plate underneath the downstream spreader, and another on the top surface of the fume hood at the innermost spot before volatile collection. An NI SCB-68 breakout box was wired to digitally control the output of the temperature control relays. A simple on/off control algorithm was built in NI LabVIEW which would set two pins of the digital out port to high or low, depending on the desired control action. A high triggers the relay, heating either the fume hood or plate.

The heater plugs were plugged into two different 120 VAC rails to avoid overloading a laboratory circuit breaker. The switch side of the relay was wired to the digital out pins of the SCB-68. The LabVIEW virtual instrument (VI) temperature controller was set to 380°C or 400°C depending on the test. A second VI temperature controller maintained the fume hood temperature. Ground biomass was massed, loaded into the hopper (which was massed prior to loading. The draw pipe was connected to the dry ice condenser was inserted through the proper port, and aligned over the center of the reaction surface. When the reactor reached the set temperature, the purge gas was introduced to the system, again allowing the surface temperature to reach the set temperature. Once this had been achieved, the condenser was filled with a mixture of acetone and dry ice, bringing its temperature to -77°C. The vacuum pump was turned on maintaining the pressure in the chamber while removing nitrogen. The feed motor, stirrer motor, shaker motor and char catch fans were then turned on, and the reactor left to run.

Following the run, the system was allowed to cool. The hopper were massed. A sheet of paper was massed, and then the char from the catch was poured onto it, and the paper massed again. The reactor and char catch were then cleaned with acetone to ensure that no residual tar remained. The oil was massed and then a sample was collected for outside composition and energy content analysis.

5.4 Evaluation of the Heat Transfer Model

5.4.1 Heat Testing Experimental Setup

A total of 1400 W of heating capacity was added to the copper heating plates in the form of six 200 W cartridge heaters, and two 100 W cartridge heaters. The 100 W cartridge heaters are placed such that they are the pair closest to the open end of the plate. This is in order to better heat the upstream sections of the heated plate with the more powerful cartridge heaters, while avoiding drawing too much power and potentially tripping a laboratory circuit breaker. The eight cartridge heaters were then wired in parallel, and the resulting net resistance was tested using a Fluke 117 True RMS Multimeter. The resulting resistance was measured to be 11.3 ± 0.2 Ω.

An initial test was performed to ensure that the plate could reach the maximum desired reaction temperature of 420°C. To test this, a Variac voltage controller was used to set the input power to 1000 W to ensure that the heaters would not overload the 120 V rail they were connected to, and then the plate was allowed to reach steady state in the chamber prior to evacuation and inert gas purging. The temperature of the plate surface was determined using a J-type surface thermocouple mounted to the lower bolt of the downstream spreader bar.

The plate was then heated in the reactor to two different set points: 380°C and 400°C, and the fume hood set to heat to temperatures of 200°C and 220°C respectively. The temperature of the fume hood was measured at the point where the fume hood touches the draw pipe using a J-type surface thermocouple. An on/off control loop was used to control both temperatures. Purge gas and ground *Pinus taeda* were introduced once the temperature of the plate had reached the set point to determine how they affected surface temperature. This was important, as new purge gas is added to the system continuously, and is not preheated, potentially cooling the plate and biomass below the specified pyrolysis temperature. Furthermore it was important to ensure that the pyrolysis reaction taking place on the plate was also not significantly lowering the plate surface temperature. Three replicates were run at 380°C and 400°C concurrent with 300 s residence time pyrolysis tests (see 5.6.4 for details).

5.4.2 Heat Testing Results

The temperature of the plate over time when connected to a steady state power load of 1000 W is plotted in Figure 5.10, with the system reaching a steady state temperature of 445°C.

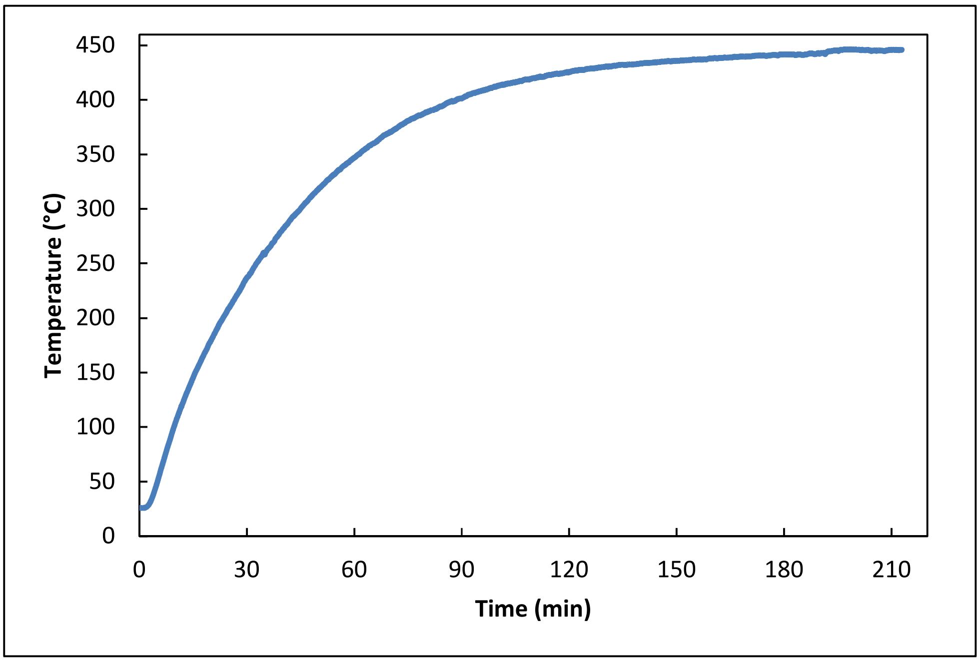

Figure 5.10 - Steady State Plate Temperature Given 1000W Input

This indicated that the amount of power that could be provided was sufficient to run commissioning tests at 380°C and 400°C. The temperature of the plate reaches steady state after 210 minutes however, indicating that there would be significant thermal lag when controlled, and that the number of tests that could be run per day would be limited due to long heat up and cool down times.

The temperature data following the plate reaching the set point temperature during each commissioning test was recorded and averaged over the length of the remainder of the replicate. The corresponding mean plate temperatures are summarized in Table 5-1.

Table 5-1 - Recorded Plate Surface Temperature During Commissioning Tests

Set Point [°C]	Recorded Temperature [°C]
380	377.9±4.0
400	396.5±4.5

As reported in Table 5-1, the average surface temperature of the plate is below the set point for the majority of the test. This is largely the result of the thickness of the stainless plate between the reacting surface and the copper heating plates imbedded in the steel. The large thermal mass of the plate delays control action due to the low thermal conductivity of 304 stainless steel, but ensures that there is sufficient energy storage within the plate to dampen the effects of sudden exposure to the nitrogen purge. Reducing the thermal lag would require machining the surface of the plate to a thickness too thin to support the spreaders which are necessary to prevent the formation of isolated hot spots on the surface of the plate.

5.5 Evaluation of the Vibratory Transport Model

5.5.1 Experimental Setup for Evaluating Vibratory Transport Model

A heater level was mounted on the tower, at a height of 0.0889m (3.5") above the reactor floor. The motor driving the eccentric mass was connected to a power supply, capable of supplying 12 volts at 3 amps, so that the motor would rotate counterclockwise. An eccentric mass of 77.48 g with an eccentricity of 20.5 mm was required to induce vibro-fluidization. Three angles: 6°, 12°, and 18°, were tested at voltages ranging between 2 and 6.5 V applied in 0.5 V increments. Four factors were measured: time required for the material to travel the length of the plate, percentage of the topmost spreader that comes into contact with biomass, percentage of the second spreader that comes into contact with biomass, and the percentage of the coverage at the bottom of the plate. Following initial testing, the range between 12° and 18° appeared most conducive to vibro-fluidization, and 4 to 5 V, the best for overall spreading.

A design of experiments with two degrees of freedom was performed, controlling plate angle and voltage. Four angles of 12°, 14°, 16° and 18°±0.5° and four voltages of 4, 4.3, 4.6 and 5 V were tested. A 16.28 cc scoop was filled with ground Loblolly pine. The scoop was massed as was an empty plastic catch. The selected angle was set using an angle gage, and the motor turned on and set to the proper voltage. The biomass was dropped onto the top-left corner of the plate, where material enters the system when fed via the reactor feed system, and a stopwatch was started. As the biomass moved past the spreaders, the percentage spread across the spreader was qualitatively determined and recorded. When particles stopped flowing over the end of the plate, the stopwatch was stopped. The scoop and the catch were massed. From these measurements it was possible to determine the mass flow rate (MFR) and residual mass fraction (RMF) using the following:

$$\dot{m} = \frac{m_{catch,\,f} - m_{catch,\,i}}{t} \tag{5.2}$$

$$f_{residual} = 1 - \frac{m_{catch,\,f} - m_{catch,\,i}}{m_{cup,\,i} - m_{cup,\,f}} \tag{5.3}$$

Damping and stiffness were further tested to ensure that the model prediction is accurate. A tapped hole was added to the plate and a PCB 353B33 accelerometer was screwed into it. This accelerometer was connected to a Kistler Type 5134 amplifier, and the amplifier to a Tektronix TDS 3014B oscilloscope. An PCB 086C05 impact hammer was wired to the amplifier and oscilloscope in the same manner. Using a triggering function to begin recording 1 second of data at a sampling rate of 10 kHz, the H frame was impacted next to the motor with the impact hammer. A fast Fourier transform (FFT) was performed on the data to determine the dominant frequencies of the vibration, and the waveform sent from the accelerometer was analyzed using the logarithmic decrement method to determine the damping coefficient, where:

$$\zeta = \frac{\delta}{\sqrt{4\pi^2 + \delta^2}} \tag{5.4}$$

where:

$$\delta = \frac{1}{n} \ln \frac{x(t)}{x(t + nT)} \tag{5.5}$$

where x(t) is the time domain response of the plate at a peak, n is an integer number of peaks after the initial peak, and T is the period of oscillation.

The motor response curve, correlating voltage to excitation frequency, was performed in a similar manner. 10000 samples at 10000 Hz were taken from the plate accelerometer while varying voltages were applied to the motor. The data was processed using an FFT, and the dominant frequencies recorded.

5.5.2 Vibratory Transport Experimental Results

The results of the MFR and RMF experiments, presented at each test angle, are plotted in Figures 5.11-14.

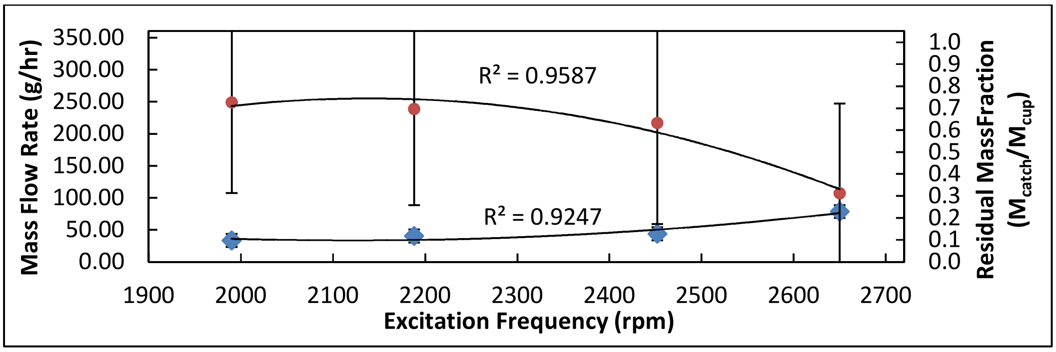

Figure 5.11 - Comparison of MFR (♦) and RMF (●) of Loblolly Pine at 12° Plate Angle and Varying Plate Excitation Frequencies and Corresponding Parabolic Fits

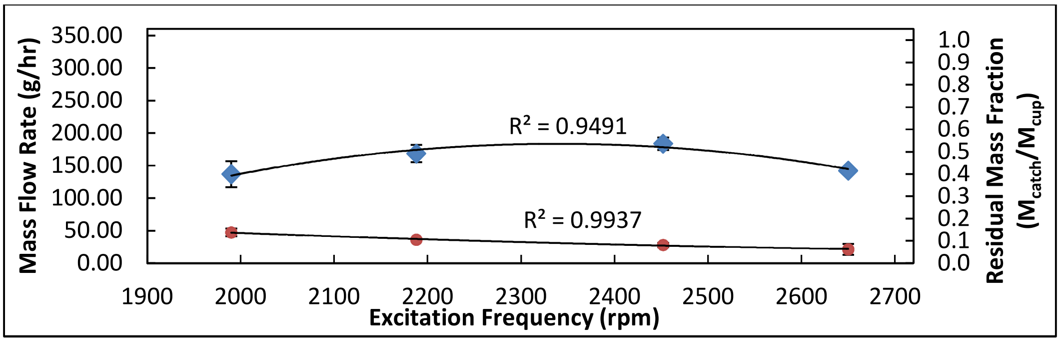

Figure 5.12 - Comparison of MFR (♦) and RMF (●) of Loblolly Pine at 14° Plate Angle and Varying Plate Excitation Frequencies and Corresponding Parabolic Fits

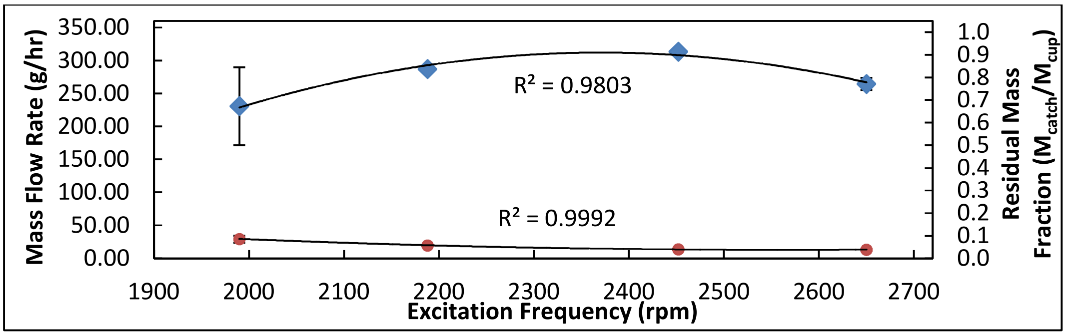

Figure 5.13 - Comparison of MFR (♦) and RMF (●) of Loblolly Pine at 16° Plate Angle and Varying Plate Excitation Frequencies and Corresponding Parabolic Fits

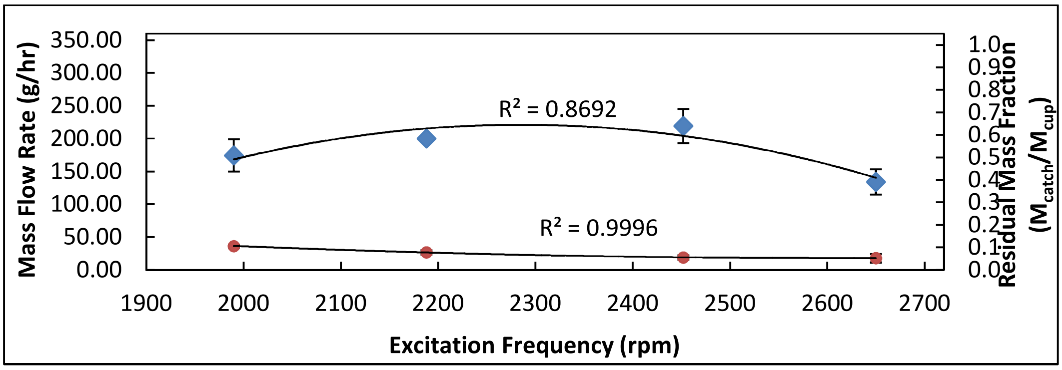

Figure 5.14 - Comparison of MFR (♦) and RMF (●) of Loblolly Pine at 18° Plate Angle and Varying Plate Excitation Frequencies and Corresponding Parabolic Fits

The dynamic response of the plate and the motor voltage-plate vibration frequency correlations were also tested. The frequency response of the plate curve is mapped in Figure 5.15.

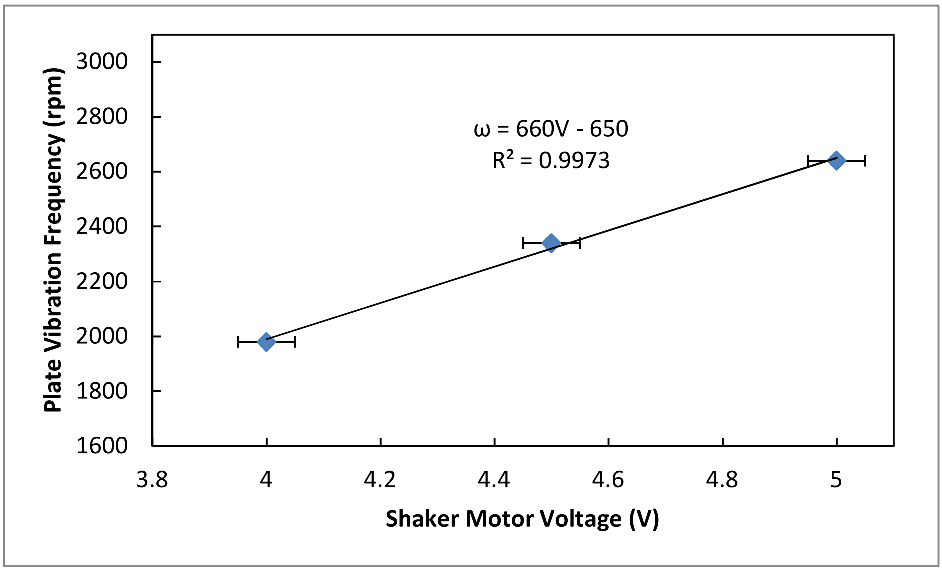

Figure 5.15 - Plate Frequency Response Curve for Single Level

The motor, which is rated to operate from 0-12 V and up to 10158 rpm, followed a linear correlation between applied voltage and motor speed.

The logarithmic decrement method uses the amplitude of the decaying peaks in a damped response to an impulse. The time domain data from the impact hammer testing of the reaction level, plotted in Figure 5.16, showed significant decay in amplitude over the first few peaks, calling the initial estimate, $\zeta = 0.5$, into question. Using the logarithmic decrement method to determine the damping ratio of the system, the damping ratio was found to be 0.124±0.018, significantly lower than the initial estimate.

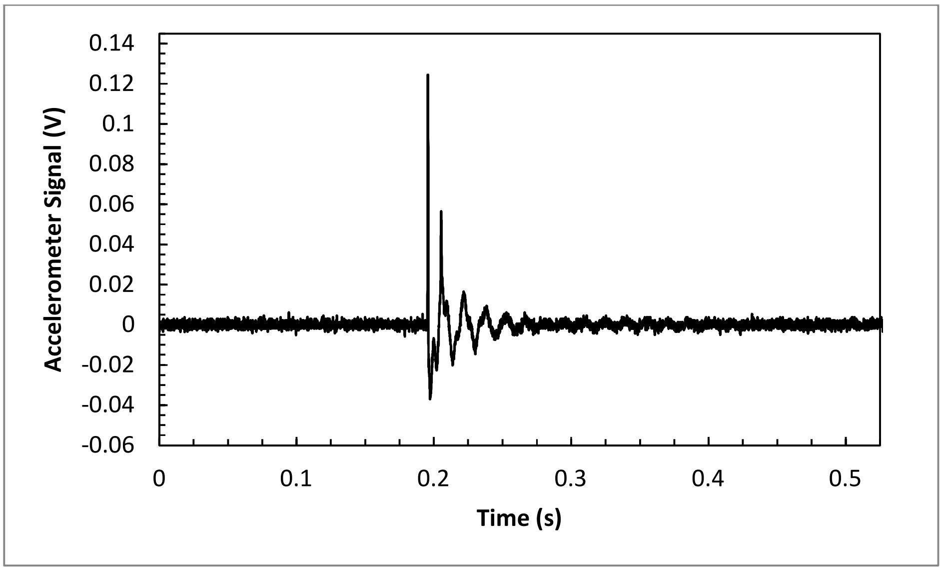

Figure 5.16 - Time Domain Response of Reaction Level to Impact Hammer Test

Additionally, the FFT of the free response of the heater level may be used to reevaluate the value that has been assigned to the natural frequency of the plate in the horizontal plane. The corresponding FFT is presented in Figure 5.17.

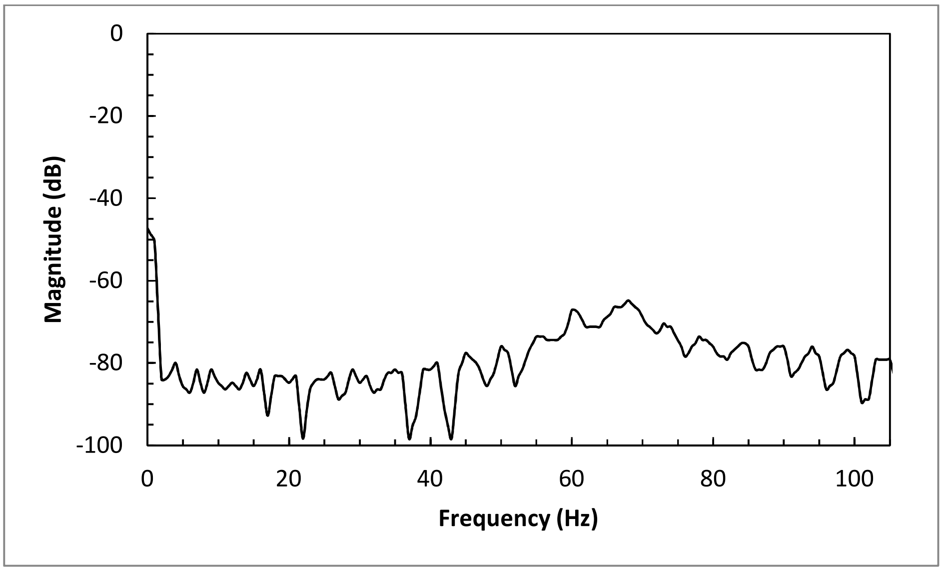

Figure 5.17 - Fast Fourier Transform of the Reaction Level Impact Hammer Test Data

As indicated by the free response, the plate is found to resonate primarily at 68 Hz. From this, an effective stiffness may be back calculated. The resulting effective spring stiffness of the vibration isolators is 3.18×10^6 N/m. Modifying the MATLAB model to account for the experimentally determined damping ratio and effective stiffness, the mass flow rate predictions changed significantly, and are presented in Figure 5.18 alongside a sample dataset from the transport tests.

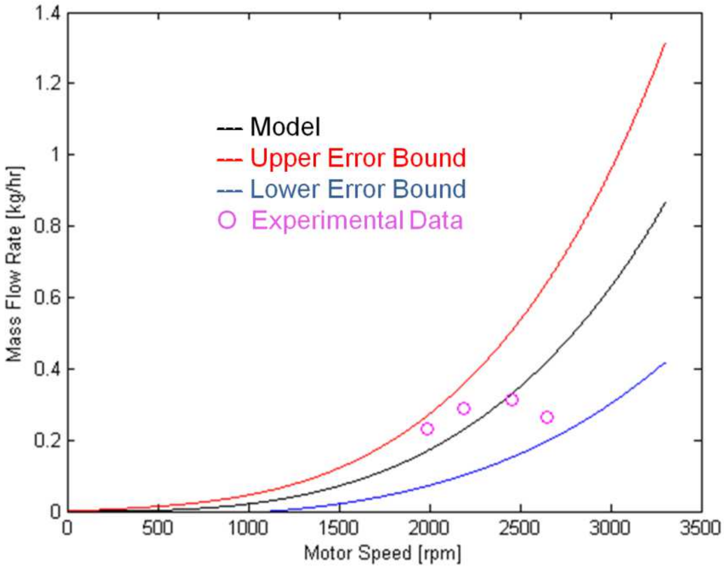

Figure 5.18 - Predicted Mass Flow Rate from Experimentally Determined Dynamic Characteristics for Transporting Loblolly Pine on a 16° Plate Angle Superimposed on Mean Data from Spreader Testing at the Same Angle

As the revised model results indicate, predicted mass flow rates drop by an order of magnitude when compared with the model developed based on the specifications given by the vibration isolators' manufacturer. As is also clear from Figure 5.18, the model encompasses the data obtained from spreader testing within its error bounds. The data, however, exhibit a significantly different frequency response curve. This may be the result of friction interactions between particles, or between particles and the plate surface that are not accounted for in the vibratory spreading model. The mass flow behavior of the biomass also defies a key parameter of the model in which full spreading is expected. While full spreading may be achieved near the top of the plate, along the longer spreader bar, this does not hold further down the plate, as the biomass coalesces along a curved path that is more excited than the rest of the plate. By this spreading phenomenon, biomass does not come into contact with large portions of the plate. The residual mass of one experiment is pictured in Figure 5.19, indicating the typical flowpath of the material.

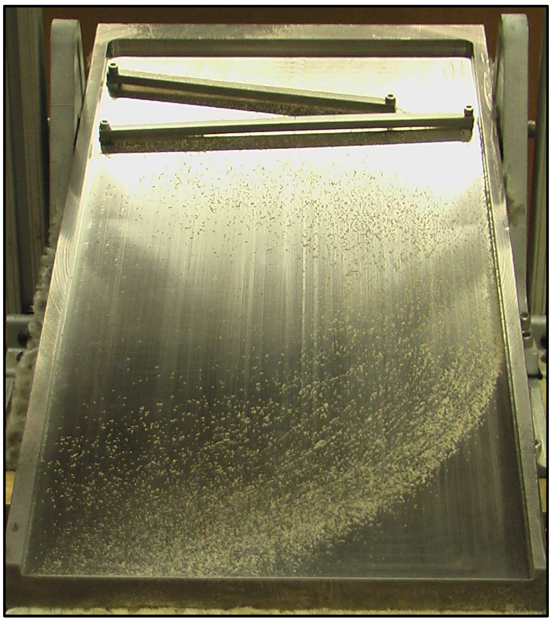

Figure 5.19 - Example Residual Mass Distribution from *Pinus Taeda* Vibratory Spreading Testing Showing Mass Flowpath and Unreacting Areas

This is problematic as an uneven temperature distribution across the plate surface will result, and the surface, being stainless steel, may not conduct heat rapidly enough to maintain isothermal pyrolysis.

Additionally, with corrections to the characteristics of the vibration isolators, new particle residence times must be considered. Table 5-2 summarizes the difference in target particle residence times before and after amplitude correction for two target reaction configurations: 14°/44.2Hz and 16°/44.2Hz, where the angle is the incline of the plate, and the frequency is the drive motor frequency.

Table 5-2 - Expected and Experimental Particle Residence Times Before and After Model Parameter Updating

Test Setting	Original Model Expected Residence Time [s]	Revised Model Expected Residence Time [s]	Experimentally Determined Residence Time [s]
14°/44.2Hz	17.3 ± 2.8	166.0 ± 32.2	99.6 ± 3.8
16°/44.2Hz	17.4 ± 2.9	167.6 ± 35.3	52.7 ± 0.4

As laid out in Table 5-2, neither the original nor the revised model exhibits a residence time similar to that determined experimentally. This is likely due to the differences between the experimental setup and granular material used in Golovanevskiy *et al.*'s [57] experiments. In their work, 50-200 μm Zirconium–Staurolite particles were used. Unlike biomass, which is fibrous in nature, sand particles, though they may be statically charged, do not exhibit the same clinging effect that wood particles do. This may contribute to a severe effective friction effect for biomass particles, retarding bulk motion. Additionally, Golovanevskiy *et al.* only considered vibration in one direction: at an angle β to the plate surface, whereas the reactor vibrates in two: circularly in the horizontal plane.

Considering these discrepancies, a new correlation for determining mass flow rate is presented in (5.6) for a plate angle range of 14-18°. A correlation for mass flow rate is presented rather than particle velocity to account for the lack of full width spreading observed during transport testing.

$$\begin{aligned}\dot{m} = &\left(1.06E-2\cdot\cos\beta-1.08E-2\right)\omega_d^2-\left(4.59E+1\cdot\cos\beta-4.65E+1\right)\omega_d \\ &+\left(4.84E+4\cdot\cos\beta-4.91E+4\right)\end{aligned} \tag{5.6}$$

where ω_d is in rpm.

5.6 Reactor Kinetics and Pyrolysis Yields

5.6.1 Review of Salient Literature

Kinetic modeling of pyrolysis reactions generally uses Arrhenius equations to relate product formation rate to temperature, following work first proposed by Bamford *et al.*[61] for modeling wood combustion. This form of modeling, which lumps multiple pyrolysis product chemicals into general product categories, is considered preferable to modeling the formation of individual products due to the large number of unique chemicals produced during pyrolysis [5]. Coefficients for these reactions are determined via thermogravimetric analaysis (TGA), in which a sample is continuously massed while being slowly heated. Fu *et al.* [62] present these coefficient values for *Pinus taeda*. This temperature-dependent reactant decay rate is then used in conjunction with a half life model to determine the mass yield of a specified product with respect to time. In biomass pyrolysis there are several methods for modeling this, all of which rely on the selection of reactants devolatilizing, or, more importantly, the products forming. The first, a pseudo-component model, attempts to model pyrolysis based on decay of the three primary macromolecules that compose woody biomass: cellulose, hemicellulose and lignin. Results from Branca *et al.*[63] have indicated that pseudo-component models perform well in matching data for TGA ovens, but are severely limited when applied to high heating rates.

The second set of models concern the production of specified groupings of product materials. Single component models consider the transformation of whole biomass into two products: char and volatiles. Two component models, complicate this somewhat, modeling the presence of secondary reactions, introducing an additional raw whole biomass (in this case, wood) reactant decaying into char and volatiles. These secondary reactions have shown to figure significantly in lower temperature reactions [4] where devolatilization rates are lower. Finally, product-based models, first proposed by Shafizadeh and Chin [64], may be used to model the breakdown of pyrolyzing material into three phases of components: char (solids), oil (liquids) and gasses. Flowcharts outlining these three models are illustrated in Figure 5.20.

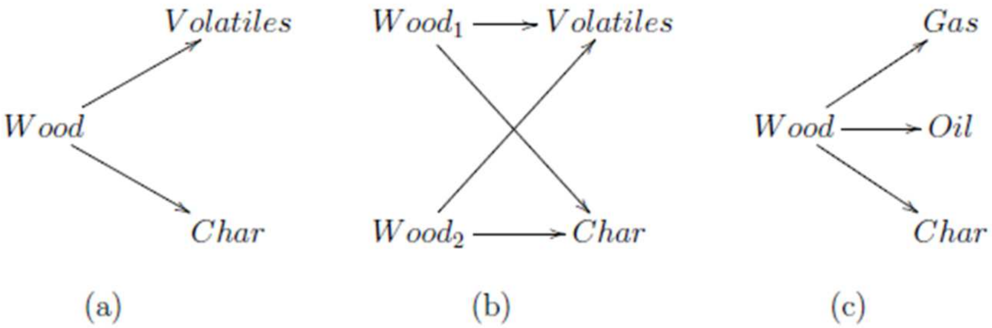

Figure 5.20 - Pyrolysis Devolitalization Models from Williams [4]: a) Single Component, b) Two-Component, c) Product-based

Williams [4] focused on developing these models for fast pyrolysis of *Pinus taeda*. Using a Chi-squared method of best fit he determined Arrhenius coefficients and maximum conversion values for fast pyrolysis reactions over a range of temperatures from 380 to 420°C, from data taken between 10 and 300 seconds of residence time.

5.6.2 Kline-McLintock Error Analysis Method for Evaluating Mass Yields

The total mass of the reacted biomass is given by the following:

$$m_{total} = \left(m_{load,i} - m_{load,f}\right) - \left(m_{hopper,f} - m_{hopper,i}\right) \tag{5.7}$$

where m_{load} is the mass of biomass and initial container before and after being fed into the hopper and m_{hopper} is the mass of the hopper before and after testing. The mass fraction of the solids yield may be determined using the following:

$$\eta_{solids} = \frac{m_{catch,f} - m_{catch,i}}{m_{total}} \tag{5.8}$$

where m_{catch} is the mass of the massing plate for the char. The mass fraction of the oil yield may be determined using the following:

$$\eta_{oil} = \frac{m_{flask,f} - m_{flask,i}}{m_{total}} \tag{5.9}$$

where m_{flask} is the mass of the Erlenmeyer flask. Finally, the mass fraction of the gas yield must be determined indirectly, because of difficulty in capturing such a large volume in gas balloon, and may be determined using the following:

$$\eta_{gas} = \frac{m_{total} - \left(m_{catch,f} - m_{catch,i}\right) - \left(m_{flask,f} - m_{flask,i}\right)}{m_{total}} \tag{5.10}$$

Using Kline-McLintock error analysis, the subsequent uncertainties in these mass balances and product yields are:

$$w_{m_{total}} = \sqrt{\begin{gathered}\left(\frac{\partial m_{total}}{\partial m_{load,i}} w_{load,i}\right)^2 + \left(\frac{\partial m_{total}}{\partial m_{load,f}} w_{load,f}\right)^2 \\ + \left(\frac{\partial m_{total}}{\partial m_{hopper,f}} w_{hopper,f}\right)^2 + \left(\frac{\partial m_{total}}{\partial m_{hopper,i}} w_{hopper,i}\right)^2\end{gathered}} \tag{5.11}$$

$$w_{\eta_{solids}} = \sqrt{\left(\frac{\partial \eta_{solids}}{\partial m_{catch,f}} w_{m_{catch,f}}\right)^2 + \left(\frac{\partial \eta_{solids}}{\partial m_{catch,i}} w_{m_{catch,i}}\right)^2 + \left(\frac{\partial \eta_{solids}}{\partial m_{total}} w_{m_{total}}\right)^2} \tag{5.12}$$

$$w_{\eta_{oil}} = \sqrt{\left(\frac{\partial \eta_{oil}}{\partial m_{flask,f}} w_{m_{flask,f}}\right)^2 + \left(\frac{\partial \eta_{oil}}{\partial m_{flask,i}} w_{m_{flask,i}}\right)^2 + \left(\frac{\partial \eta_{oil}}{\partial m_{total}} w_{m_{total}}\right)^2} \tag{5.13}$$

$$w_{\eta_{gas}} = \sqrt{\begin{gathered}\left(\frac{\partial \eta_{gas}}{\partial m_{total}} w_{m_{total}}\right)^2 + \left(\frac{\partial \eta_{gas}}{\partial m_{catch,f}} w_{m_{catch,f}}\right)^2 + \left(\frac{\partial \eta_{gas}}{\partial m_{catch,i}} w_{m_{catch,i}}\right)^2 \\ + \left(\frac{\partial \eta_{gas}}{\partial m_{flask,f}} w_{m_{flask,f}}\right)^2 + \left(\frac{\partial \eta_{gas}}{\partial m_{flask,i}} w_{m_{flask,i}}\right)^2\end{gathered}} \tag{5.14}$$

The uncertainties for all masses are 10 mg.

5.6.3 Modeling Devolatilization Kinetics

Williams' [4] series of best fit curves for different chemical rate reaction schemes must be considered in order to compare oil and total volatiles yields to his work on *Pinus taeda* pyrolysis. Williams incorporated the use of the three models presented in Figure 5.20. These models are built from the reaction rates of the groupings of products. The reaction rate of a pyrolysis product may be given as:

$$k_p(T) = A_p e^{-E_{a,p}/RT} \tag{5.15}$$

where A_p is a constant specific to the product, $E_{a,p}$ is the activation energy of the reaction, and R is the universal gas constant. Mass fractions of pyrolysis products (oil, char, gas, etc.) relate to the reaction rate in the following residence time-dependent relation:

$$\eta_{prod}(t) = c_{prod}\left(1 - \frac{1}{2}^{tk_p(T)/\ln 2}\right) \tag{5.16}$$

where c_{prod} is the maximum convertible quantity of the pyrolysis product.

A two-component devolatilization was found by Williams to be a closer-fitting model than the single component model. This model is formulated in (5.17).

$$\eta_v(t) = c_{v1}\left(1 - \frac{1}{2}^{tk_{p1}(T)/\ln 2}\right) + c_{v2}\left(1 - \frac{1}{2}^{tk_{p2}(T)/\ln 2}\right) \tag{5.17}$$

This model is however better suited to modeling thermal degradation of component chemicals at variable temperatures, rather than whole wood reacting in isothermal conditions. Williams instead uses a form of (5.17) for which the rate coefficient for a given temperature has been experimentally determined, and set as a constant within the equation, leading to the reformatted equation presented in (5.18).

$$\eta_v(t)=c_{v1}\left(1-\frac{1}{2}^{t/\tau_{v1}}\right)+c_{v2}\left(1-\frac{1}{2}^{t/\tau_{v2}}\right) \tag{5.18}$$

The values of the coefficients in (5.18) from Williams' experimentation using a Chi-squared method of best fit at the target pyrolysis temperatures are listed in Table 5-3:

Table 5-3 - Rate Coefficients for Two Component Modelof Isothermal *Pinus taeda* Pyrolysis from Williams [4]

Coefficient	At 380°C	At 400°C
c_{v1} [g/g]	0.439	0.526
c_{v2} [g/g]	0.314	0.268
τ_{v1} [s]	52.5	16.5
τ_{v2} [s]	2.06	0.834

5.6.4 Experimental Setup and Procedure

A complete step by step experimental procedure may be found in Appendix A. Following initial cleaning, setup and sealing, the temperature of the reactor was set, and the reactor turned on and left for 1.5 to 2 hours to be allowed to reach steady state. The vacuum pump was connected to the condenser system and turned on. Nitrogen was added to the system to complete the purge of oxygen and water vapor from the reactor. The nitrogen was then turned to a low flow rate. Dry ice was then added to the acetone bath until the temperature had reached -77°C, checking to make sure ice was not forming on the inside of the condenser. The hopper was fitted into the feed mechanism and a measured quantity of ground *Pinus taeda* added to it. The shaker motor was turned on and set to the desired voltage. The feed and hopper stirrer motors were then turned on.

An amount of time equal to the residence time was allowed to pass before the shaker motor and heater system were shut down following the exhaustion of the hopper contents. The vacuum pump and purge gas were turned off after no more vapor was observed entering the condenser. The condenser system was then removed and sealed to prevent moisture condensation, and the draw tube port sealed to prevent char combustion. The secondary collection flask was massed immediately, but the char and primary collection flask were massed the following day, giving the frozen condensed vapor time to thaw (example of frozen condensate pictured in Figure 5.21). Residual oil in the condenser was washed out using acetone, and the mass of this wash was taken into account. Using a squirt bottle to spray acetone on the walls of the condenser was found to transport 52.7±2.8% of the acetone, by mass, into the collection flask along with the oil. Emptying the acetone bath, flipping the condenser, and washing the walls with acetone to collect oil isolated higher on the walls of the condenser (example oil isolation pictured in Figure 5.21) was found to transport 31.2±4.5% of the acetone, by mass, into the collection flask along with the oil. These results were developed by running five replicates of "dry" washes, in which the condenser was washed with acetone, and the fraction of the residual and evaporated acetone determined.

Figure 5.21 - Examples of Frozen Condensate and Oil Formation High on Condenser Walls

Two residence times (100 s and 300 s; generated by angle and voltage settings of 14°/5V and 16°/5V respectively) and two temperatures (380°C and 400°C) were explored to determine whether the reactor would generate unique yields at varying operating points. The temperatures were selected as the kinetics models presented in Williams' [4] work laid a repeatable foundation for expected yields at these two temperatures. Higher temperatures were not selected as the two-component curves describing total volatile formation reach a steady value at residence times too short to collect meaningful data; due in part to low repeatability at low residence times. Additionally, the top spreader bar was removed as early commissioning tests found that it prevented flow when the reactor was at temperature. An example of char buildup is pictured in Figure 5.22.

Figure 5.22- Buildup of Char and Torrified Biomass on Upper Spreader During Early Commissioning Test

5.6.5 Experimental Results

Four commissioning tests of three replicates were run, and the mass balance of the pyrolysis product, as well as the total volatile yield, is presented, for all replicates in Table 5-4, and the yields summarized in Table 5-5.

Table 5-4 - Mass Balances From *Pinus taeda* Reactor Commissioning Tests - All Replicates

Pyrolysis Temperature [°C]	Residence Time [s]	Replicate Number	η_{solids} [g/g]	η_{oil} [g/g]	η_{gas} [g/g]	$\eta_{volatiles}$ [g/g]
380	100	1	0.309±0.001	0.462±0.001	0.230±0.002	0.691±0.002
		2	0.356±0.004	0.675±0.005	-0.031±0.007	0.644±0.008
		3	0.248±0.001	0.453±0.001	0.299±0.002	0.752±0.002
380	300	1	0.184±0.001	0.145±0.001	0.671±0.002	0.816±0.001
		2	0.177±0.001	0.378±0.001	0.446±0.002	0.824±0.001
		3	0.442±0.004	0.786±0.005	-0.228±0.007	0.558±0.008
400	100	1	0.456±0.001	0.281±0.001	0.263±0.002	0.544±0.002
		2	0.502±0.002	0.316±0.002	0.181±0.003	0.497±0.003
		3	0.560±0.008	0.356±0.007	0.083±0.013	0.440±0.015
400	300	1	0.269±0.051	0.191±0.300	0.540±0.255	0.731±0.050
		2	0.185±0.051	0.503±0.300	0.312±0.255	0.815±0.050
		3	0.178±0.051	0.791±0.300	0.031±0.255	0.822±0.050

Table 5-5 - Summary of Mass Balances From *Pinus taeda* Reactor Commissioning Tests

Pyrolysis Temperature [°C]	Residence Time [s]	η_{solids} [g/g]	η_{oil} [g/g]	η_{gas} [g/g]	$\eta_{volatiles}$ [g/g]
380	100	0.304±0.054	0.530±0.126	0.166±0.174	0.696±0.054
380	300	0.268±0.151	0.436±0.324	0.296±0.468	0.733±0.151
400	100	0.506±0.052	0.339±0.015	0.155±0.065	0.494±0.052
400	300	0.211±0.051	0.495±0.300	0.294±0.255	0.789±0.050

The mean oil and total volatile yields are plotted against Williams' two-component best fit models in Figure 5.23 and Figure 5.24.

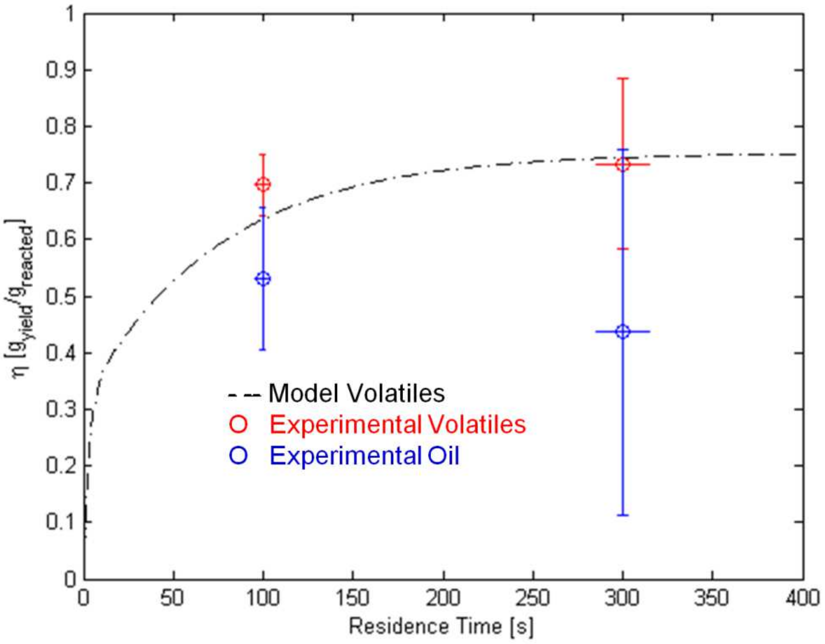

Figure 5.23 - Commissioning Test Mean Volatile and Oil Yields Plotted Against Williams' Two-Component Volatile Formation Model for Pyrolysis of *Pinus taeda* at 380°C

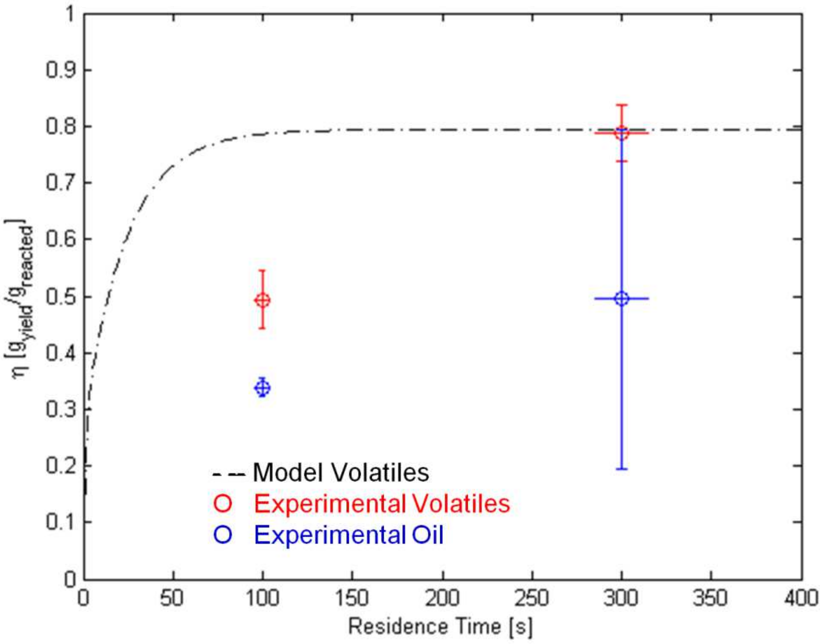

Figure 5.24 - Commissioning Test Mean Volatile and Oil Yields Plotted With Williams' Two-Component Volatile Formation Model for Pyrolysis of *Pinus taeda* at 400°C

As illustrated in Figures 5.23 and 5.24, total volatile yields increase with residence time, which is consistent with what is expected. The total volatiles, with the exception of the test performed at 400°C and 100 s, show good agreement with the two-component model. Oil yields are not consistent, exhibiting uncertainties greater than 10% in all but one test and greater than 30% in two. Oil yields also appear to decrease as residence time increases at 380°C. At non-gasifying temperatures, this is impossible, likely coinciding with incomplete evacuation leading to tar formation on the inside of the chamber or incomplete condensation leading to condensation in or beyond the pump. Tar formation on the chamber walls (pictured in Figure 5.25) is the most likely candidate, as this developed during the majority of the replicates, though tar formation in general plagues pyrolysis reactor design.

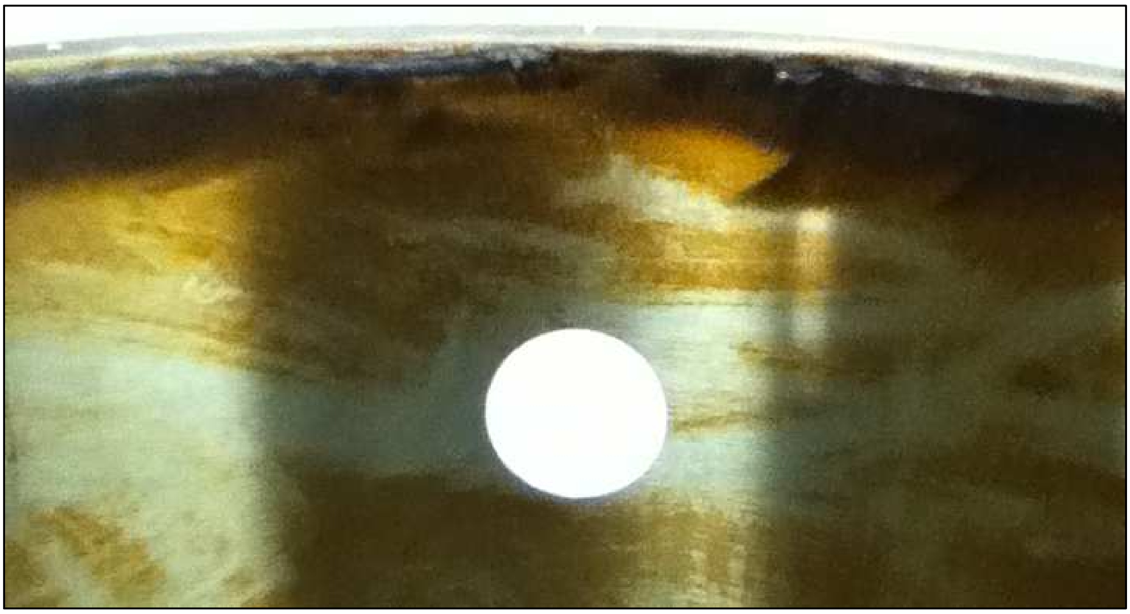

Figure 5.25 - Tar Formation on Reactor Chamber Walls

It is highly probable that, because plate residence time tests were performed only on raw wood, the residence times for the shorter tests at 100 s are actually considerably shorter, which might account for the high solids yields at 400°C. Undergoing devolatilization the ground biomass would become less dense, requiring less force to accelerate the particles. To test this theory, the 100s residence time condition was retested with both raw wood and char samples. Two tests of three replicates were run. The resulting residence times are summarized in Table 5-6.

Table 5-6 - Residence Time Results for Retest of 100 s Residence Time Condition on Raw Wood and Char Particles

Expected Residence Time [s]	Raw Wood Residence Time [s]	Char Residence Time [s]
99.6 ± 3.8	18.0 ± 2.0	15.0 ± 2.0

From the retest it becomes clear that not only does the char not behave in the same way as the ground raw wood, the heating and prolonged use of the vibration isolators have shifted the expected residence time for raw wood samples 81.6 s lower on average. Replotting (presented in Figure 5.26 and Figure 5.27) the mass yields for the 400°C case with the char residence time, the model shows considerably greater agreement between the volatile formation curve and experimental data.

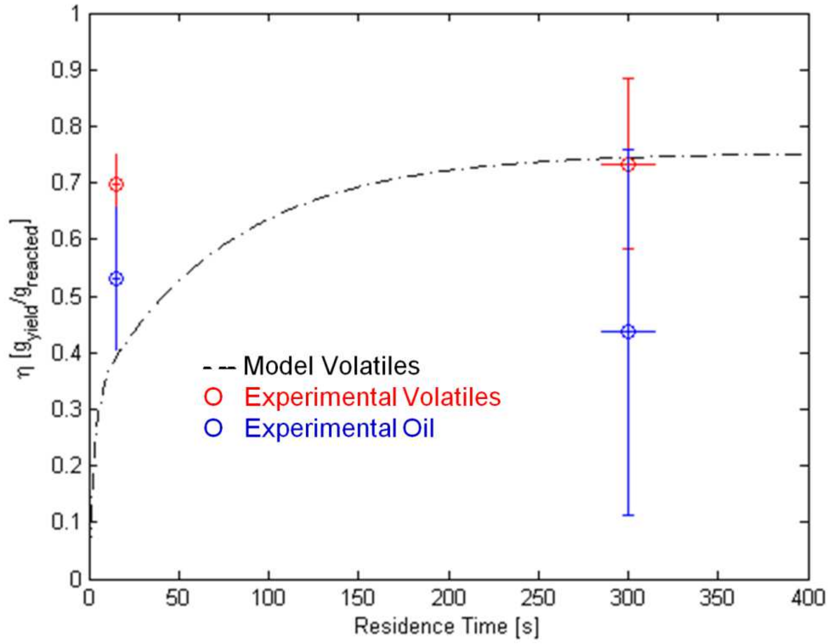

Figure 5.26 - Commissioning Test Mean Volatile and Oil Yields Plotted With Williams' Two-Component Volatile Formation Model for Pyrolysis of Pinus taeda at 380°C, with Updated Residence Times

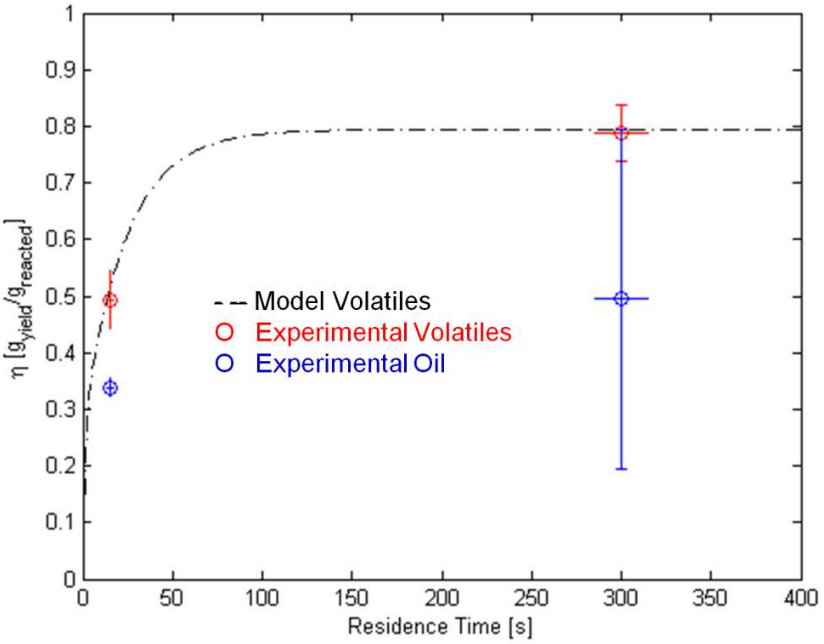

Figure 5.27 - Commissioning Test Mean Volatile and Oil Yields Plotted With Williams' Two-Component Volatile Formation Model for Pyrolysis of *Pinus taeda* at 400°C, with Updated Residence Times

While the time shift appears to correctly predict volatile formation at 400°C, the shift at 380°C results in volatile formation that greatly exceeds prediction. At 400°C, TGA data shows a greater degree of devolatilization, therefore the particles undergoing pyrolysis at 400°C must be losing mass at a rate greater than at 380°C, altering their flow characteristics. This does not, however, explain why the char yield of the 380°C test is so much less than that of the 400°C test, as the mass loss is limited by diffusion rates rather than heating rates in fast pyrolysis. While more mass will diffuse at long residence times, the biomass undergoing pyrolysis at two different temperatures would likely experience similar mass devolatilization rates, and so the most plausible explanation is a lower residence time at 400°C than at 380°C. As the temperature inside the reactor chamber increases, the mechanical properties of the rubber vibration isolators change, which may be leading to differing kinematic characteristics, leading to a change in residence time. It is difficult to believe, however, that a difference of 20°C could result in such a significant change considering that the isolators have already been heated by 180°C above the temperature of the spreading tests when the reactor is brought up to temperature.

It should be noted here that the voltage and angle settings resulting in the 300s tests did not directly correspond to residence times of 300s in the vibratory spreading experiments. Rather, when heat was applied during these tests, poor transport of the material occurred with the majority of the char remaining on the plate surface, leading to a "long residence time" condition correlating to the full extent of the pyrolysis reaction at the set temperature. This time was capped at 300s, as the two component volatile yield curves for the set temperatures have effectively reached their maximum yields after this time. This poor transport typically corresponded to a buildup of char on the plate that forced the feed motor to be cut off prematurely during several replicates to ensure all of the biomass on the plate could react. Even so, an early shutdown did not necessarily lead to repeatable solids yields; unreacted biomass collecting on top of the char under the hood is difficult to see through the reactor lid. As a result, the repeatability of the volatile yields is lower than that at 100s. As reported in Table 5-4, the third replicate at 380°C and 300s exhibited a solids yield more than two times that of the other two replicates. This discrepancy is most likely the result of buildup of unreacted biomass on top of the residual char layer, leading to an impossible negative gas yield. An example of buildup resulting from a delayed feed shut off is pictured in Figure 5.28; note the light brown partially-reacted biomass resting on top of the darker char.

Figure 5.28 - Unreacted Biomass Buildup on Residual Char Layer in Experiment with Top Spreader Removed

The amount of biomass reacted per test was highly variable; on average the mass processed by the reactor per replicate varied by more than 62%. This is, in part, due to the incomplete reaction caused during the buildup of material near the top of the plate mentioned earlier. The plate shaker motor was prone to thermal failure with prolonged use, forcing use of smaller replicate batches due to the difficulty of removing unreacted biomass from the hopper. Due to the high static cling of dried wood particles, residual unreacted biomass clung to the hopper and feed chute, lowering the amount of processed biomass per run. Given the size of the reactor, the relatively small loads processed during each replicate likely played a significant part in affecting the percentage yields of the products. Table 5-7 reports the total mass of the biomass reacted during each test.

Table 5-7 - Total Masses of Raw Biomass Pyrolyzed Per Test

Pyrolysis Temperature [°C]	Residence Time [s]	m_{total} [g]
380	100	11.13±5.56
380	300	18.62±12.19
400	100	9.56±7.01
400	300	10.55±5.39
All Tests		12.47±7.81

5.7 Summary

This chapter presented reactor assembly details and presented data from and summaries of reactor commissioning tests. The method of operation and control of the reactor was also detailed.

Steady state power requirements were determined for the desired temperatures, and steady state temperature for 1000 W of input determined. Dynamic temperature data was collected and presented during long residence time pyrolysis testing, and it was found that the control system lagged behind the plate temperature, leading to mean plate surface temperatures 2.1°C and 3.5°C below 380°C and 400°C respectively.

The vibrating motor's response to input voltage was characterized. Mass flow rate with respect to plate incline angle was also tested and compared with the vibratory transport model's predictions. Kinematic characterization of the heating level was performed via impact hammer testing, providing *in situ* values for effective stiffness and damping coefficient. Applying these revised values to the vibratory spreading model, significant improvements were seen, showing good agreement between the model and experimental data.

Full system commissioning tests at various temperatures and residence times were run for fast pyrolysis of *Pinus taeda*. These results were compared with the results of two-component pyrolysis volatile-formation models developed by Williams [4]. Total volatile yields corresponded well with Williams' predictions with the exception of 100s at 400°C. Oil yields, outside of tests at 100s at 400°C, have shown low repeatability, especially at longer residence times. Oil yields may have further been influenced by tar formation on the inside walls of the reactor and in the gas line. Test residence times were retested after prolonged reactor use and found to be considerably shorter, exhibiting even shorter residence times for char. The use of a DC motor as the shaker drive was found not to be a viable long term solution to vibrating the plate.

CHAPTER 6

CONCLUSIONS AND FUTURE WORK

6.1 Summary and Conclusions

This work addressed the need for development of a novel reactor for continuous biomass pyrolysis. Typical fast pyrolysis reactors exhibit a myriad of processing problems such as wear from char, and long vapor residence times. This work explored the design, construction and commissioning of a continuous isothermal fast pyrolysis reactor aimed at addressing these and other problems. A novel design incorporating biomass pyrolyzing while flowing down a vibrating plate was conceived, examined from a heat transfer standpoint, constructed, and then tested to characterize the vibratory transport of the target feedstock, ground *Pinus taeda*. Commissioning tests were then performed to serve as both a test that the reactor worked as designed and to verify earlier work performed by Williams [4] on small batches of material.

A multi-mode heat transfer model for the pyrolyzing plate was developed to determine the required power draw to sustain a continuous fast pyrolysis reaction in a nitrogen environment. An investigation of two potential condensers for volatile chilling were performed to determine an appropriate choice of condenser for the system, as well as for developing a system that would allow for short vapor residence times. Finally, char cooling was considered to prevent secondary reactions.

A vibratory transport model was developed for ground wood material passing down an inclined plate. This model was tested via experimental spreading tests, and found to inadequately characterize the general response, although the results fell within the error bounds of the model. As a result, empirically-derived responses were used to set pyrolysis residence time in reactor commissioning.

A novel reactor was designed which uses a continuous hopper-fed system to drop ground biomass onto a vibrating heated plate under a fume hood and collection tube. A mobile platform for the reactor was designed, and a tower to mount the reaction stages was constructed. A single reaction stage and vapor collection system were designed, machined and assembled. A National Instruments LabVIEW control system was built to control and monitor temperatures in the reactor.

Commissioning testing was undertaken to ensure that the reactor worked as designed. Four full pyrolysis tests were run to test yields at two temperatures and two residence times. These were compared with results from Williams [4], and found to be largely consistent in total volatile production and inconsistent in oil yields with his two-component product formation models. It was also found that the vibratory spreading system responds significantly differently at high temperatures than at room temperature, and that char exhibits significantly lower residence times than raw wood. While the results are insufficient for a full kinetics study, the results show that the reactor is operational, and ready for further research into the kinetics of *Pinus taeda*, as well as full testing on other biomass species.

Pursuant to work summarized here and presented in the previous chapters, the following conclusions can be made:

- A multi-mode heat transfer model of a moving biomass bed was developed to determine the heat requirement for pyrolysis as a function of mass flow rate and temperature.

- Temperature limit testing was performed using a limited power input of 1000 W, and confirmed the heat transfer model with the reacting surface reaching a steady state temperature of 445°C.
- Temperature control tests were run at 380°C and 400°C, and it was found that the reactor control system maintained the reactor surface temperature to within 2.1°C and 3.5°C respectively.
- A modeled counterflow condenser for the reactor exhibited an effectiveness of 0.999.
- A modeled dry ice trap condenser for the reactor exhibited an effectiveness of 0.994.
- A vibratory spreading model of the bed was developed and used to predict the mass flow rate and residence times of biomass within the reactor at as a function of plate angle and excitation frequency.
- Mass flow rate best fit curves were developed empirically for raw biomass and found to fit within the error bounds of the analytical vibratory spreading model.
- Particle residence time at pyrolysis temperatures was found to not be consistent with the analytical model due to char formation leading to lower particle mass and hence faster transport.
- Volatile yields from commissioning testing largely agreed with yield predictions from kinetics models developed by Williams.

6.2 Contributions

- A new experimental continuous isothermal fast pyrolysis reactor

The reactor design was presented along with its development process, vibratory transport analysis, and heat transfer analysis used in validating pyrolysis performance. The reactor, through varying plate angle and shaker motor voltage, allows for the control of resident time based on vibratory transport. A feedback control system controls heaters, utilizing conduction as the primary heat transfer mode, allowing for the separation of heat and mass transfer.

- A characterization of vibratory transport behavior of ground raw *Pinus taeda*

An empirical evaluation of the vibratory transport model for the reactor was performed. The evaluation found that the physical model did not perform in accordance with the analytical model, but operated within the error bounds of the model. As a result several empirically-derived curves for vibratory transport of ground *Pinus taeda* were developed for varying angles and vibratory frequencies.

- The comparison between commissioning data and micro-reactor results

Williams [4] performed extensive testing on the fast pyrolysis of *Pinus taeda*, utilizing single and two-component kinetic models to characterize volatile formation, generating a set of time-dependent yield curves at temperatures between 380 and 420°C. Commissioning tests were run at 380°C and 400°C and at residence times of 100s and 300s. Product yields were compared with Williams' two-component curves to verify the results obtained by the micro-reactor. While these results are not sufficient to serve as a complete kinetics evaluation, they form the basis for one to compare with Williams' results.

- The following papers have been submitted for review:

1. Glauber, S. and Mayor, J. R., "An investigation of vibratory spreading of ground loblolly pine for application in pyrolysis". Journal of Biomass and Bioenergy, ###.
2. Glauber, S. and Mayor, J. R., "Design of a novel continuous isothermal fast pyrolysis reactor". Journal of Thermal Science and Engineering Applications, ###.
3. Glauber, S. and Mayor, J. R., "Design and commissioning of a novel continuous isothermal fast pyrolysis reactor". To be presented at the ASME 2013 Summer Heat Transfer Conference, Minneapolis, MN USA, July 14-19.
4. Glauber, S. and Mayor, J. R., "An investigation of continuous fast pyrolysis of loblolly pine using a novel reactor". To be presented at the ASME 2013 Summer Heat Transfer Conference, Minneapolis, MN USA, July 14-19.

6.3 Recommendations for Future Work

- Pyrolysis of *Miscanthus x giganteus*

An investigation into the pyrolysis of giant miscanthus (*Miscanthus x giganteus*) was planned for in addition to the work presented. While attempting to obtain micro-reactor results, against which to compare results from the continuous reactor, it was found that grinding the grass was exceedingly difficult, leading to highly fibrous particles. These particles clung together, resisting vibratory spreading in both the micro and continuous reactors. Research by Kokko *et al.* [65] has indicated that the grindability of miscanthus greatly increases with torrefaction, but this also alters the material being studied. This would make an interesting study if the reactor were modified to have a torrefying and grinding stage, and the data from the miscanthus compared with torrefied *Pinus taeda*.

- Modal analysis and tuning of heater level

It was originally assumed that the material flow down the inclined plate would spread across the entire width of the plate. While the spreaders did accomplish this at the top of the plate, the pattern did not continue all of the way down. This is because the plate has a series of mode shapes at which vibratory input excites. As a result, the system can only handle, at maximum, a tenth of the desired mass flow rate. Modal analysis and exploration into subsequent modifications may be warranted to increase this mass flow rate.

- Inclusion of mass loss in vibratory spreading model

Char particles were found to exhibit different vibratory spreading characteristics than raw wood, throwing off the residence time calculations. The vibratory spreading model should be modified to account for mass loss, and subsequent change in particle kinematic behavior over time. The devolatilization rates are given by the kinetics models serving as a model of mass loss with respect to time.

- Expanded build for fractionated pyrolysis

The projected future of this reactor will incorporate multiple levels to achieve fractionated pyrolysis. This is of interest as it will allow the experimenter to explore the different products produced at increasing temperatures. In such a setup, the raw material would pass down an angled plate at a low set temperature over a desired residence time. The resulting partially-reacted char would then fall onto a lower plate at a higher temperature and so forth. Each level would have its own fume hood and condenser. The chamber is currently compatible with three condensers. Utilizing them will, of course, require the construction of two additional shaker levels and, likely, a restructured control system.

- Redesign of heater plate for cost and waste reduction

The machining of the plate required a significant amount of time, at least 30 man-hours, and produced almost 10 kg of waste material. Even so, additional machining would be required to decrease the thickness of the reacting surface, bringing the heat source closer to the reacting surface and hence making the surface temperature more responsive to the control system, in addition to lowering test lead times. It may be beneficial to construct future plates from three pieces of water-jetted stainless steel. A half inch thick block with a cutout for the heater plates and tapped holes for fixing the angle serves as the base. A thin sheet is the second piece and serves as the reacting surface. Finally, a thin-walled U-shaped piece is cut from 1/2" or 1/4" thick material, serving as the walls of the reacting area. Four through holes would pass through the corners of each plate, allowing the assembly, and backing insulation and plate, to be bolted together and sealed. This would reduce the time to produce the plate to no more than 3 hours. Some of the time savings could also be used to cut slots into the base piece to allow the cartridge heaters leads to easily pass out of the plate, a complication in the current design, the solution to which required additional machining time to prevent the modified backing from sagging. A modification of the spreader mounting would be required however, as the thin sheet cannot support the bolts necessary to hold the spreaders in place.

- Redesign of condenser system for prolonged cooling

While the existing feed system is well-suited for continuous use for two or more hour batches, the volatile condensation system is not. Dry ice must be fed into the condenser at regular intervals to keep the dry ice and acetone mixture at a constant temperature. Currently there is no way to do this automatically, and is thus an area for further improvement to the design. Additional cooling concerns are raised by running short batches. The existing design allows the heating plate to remain at temperature because of its high mass, but it takes upwards of two hours to heat up, and many more to cool down, limiting testing to, at best, twice per day. Additional material removal in non-structural areas of the plate would help alleviate the heat up and cool down time.

- Replacement of motor with pnuematic vibrator

As discussed in Chapter 5, motor failure was an issue during several tests. While some motors overheated before the introduction of radiation shields for the motors, later ones vibrated enough that the brushes worked loose, causing the motor to die mid-experiment forcing prolonged downtime as the reactor was stripped down and refitted with a new motor. A modification of the reactor should be considered to replace the motor with a pneumatic vibrator. A pneumatic vibrator does not run the risk of overheating, unless thermal expansion of the vanes or bearings causes the rotational piece to stall. Though most are designed to work with air, nitrogen could be pumped through one instead, doubling as a purge gas system.

APPENDIX A

CONTINUOUS REACTOR STEP BY STEP TESING PROTOCOL

1. Set the desired plate angle using an angle gauge.
2. Check to ensure that all in-chamber power cables are not frayed and connected to the appropriate relays.
3. Assemble secondary flask unit by inserting branch adapter assembly into a clean, dry 500 mL Erlenmeyer flask.
4. Mass the secondary flask assembly and set aside on a clean towel, metal tray or shop rag.
5. Mass a clean, dry 2L Erlenmeyer flask, and attach it to the bottom of the condenser via the standard taper joint, and move the assembly to the aluminum spill tray.
6. Connect the condenser and the draw tube so that the holes in the draw tube face downwards.
7. Lifting the condenser assembly and tray, insert the draw tube through the middle port of the chamber, until the seal at the condenser mouth meets the seal around the port, letting the tray and weight of the flask come to rest on the support platform.
8. Tighten one of the adjustable straps around the condenser and chamber at the level of the draw tube to securely hold the condenser in place.

9. Place the secondary flask assembly in the grip of the ring stand, gripping the joint of the flask, and slide the free male taper joint into the free female joint on the condenser, positioning the ring stand to hold the assembly in place.
10. Slide the fume hood into place so that the lofted portion is just touching the draw tube.
11. Replace the top of the internal frame and tighten down the bolts holding it in place.
12. Lower the chamber lid into position, ensuring that the feed chute has not bent or been rotated.
13. Bolt the chamber lid to the chamber, and connect the feed motor to one of the power supplies.
14. Connect the plate surface, fume hood, and gas line thermocouples to the thermocouple reader.
15. Plug the power cables for the plate and fume hood heaters into different 120 VAC rails. Make sure to plug the fume hood heater plug in first, as it is connected to the chamber grounding wire.
16. In the LabVIEW VI, set the desired plate and fume hood temperatures.
17. Rename the data file in the VI using the following notation: NxxTyyyVzzAww, where "xx" is the replicate number, "yyy" is the temperature in degrees Celsius, "zz" is the shaker motor voltage to the first decimal place without a decimal point, and "ww" is the plate angle.
18. Click "run" on the VI, and leave for 1.5 hours to reach the set point.

19. Fill a cup or other distribution container with ground biomass stored in the freezer, and mass it.
20. Mass the hopper and place it into its support structure and feeding system.
21. Pour the biomass into the hopper, and cover with the lid.
22. Re-mass the cup and record its empty mass.
23. Connect the hopper stirrer motor and char catch fans to power supplies, and run each at 10 V.
24. Once the plate reaches the set point, connect the vacuum pump to the free barbed connector on the branch adapter, and turn on the pump.
25. Turn on the purge gas to a low flow rate (line pressure: 100 kPa), and leave for 5 minutes.
26. Fill the bath of the condenser at least 3/4 of the way full with acetone.
27. Slowly, using tongs, lower chunks of dry ice no larger than your fist into the acetone bath, making sure to maintain control over the chunk (be able to pull it out rapidly) to ensure that the bath does not spill over. IMPORTANT: If a chunk of dry ice shows a visible fracture line, break the chunk along that line and then insert one of the half chunks. This will go a long way towards preventing spills.
28. When the acetone bath stops noticeably boiling, this happens at around -55°C, insert a large chunk of dry ice, and allow it to sit on the bottom of the condenser.
29. Slowly add additional acetone until the addition of more will lead to spillover. This will likely happen with between 1 and 2 inches of the bath unfilled.

30. Start the shaker motor, setting it to the desired voltage.
31. Turn the nitrogen purge down so that the line pressure is reduced to 25 kPa.
32. Set the feed motor voltage to 1.6 V, and look through the lid to ensure that material is reaching the plate.
33. Leave the feed motor on until no more material is dropped onto the plate, and then turn off it and the stirrer motor.
34. Allow the shaker motor to continue until the desired residence time has elapsed, and then turn the motor off.
35. Hit the stop button in the VI to turn off control action, and unplug the power cables for the fume hood and plate heaters.
36. Ensure that the relays are not still on by entering the block diagram of the VI in LabVIEW, double clicking on the DAQmx output box on the far right side of the diagram, bringing up the manual controls for teh DAQ output.
37. Ensure that neither output channel radio button is selected, and click the "run continuously" button.
38. Click "stop" and exit the DAQmx popup.
39. Leave the vacuum pump and purge gas on until vapor can no longer be seen entering the condenser.
40. Remove the secondary flask assembly and mass it.
41. Seal the connection point on the condenser for the branch adapted with a no. 5 rubber stopper.
42. Using heat-resistant gloves, remove the adjustable strap around the condenser.
43. Carefully, remove the condenser assembly and tray and move to a clean area.

44. Plug the draw tube port with the unused large orange stopper.
45. Remove the draw tube, gripping it at the connection point with heat-resistant gloves, and set aside to cool.
46. Plug the connection point and the condenser with the glass plug.
47. Set the condenser aside to let the condensate melt (this will take upwards of 12 hours).
48. Clean the secondary flask assembly with acetone, collecting the condensed oil in the Erlenmeyer flask.
49. Pour the acetone/oil mixture into a clean vial.
50. Label this vial "NxxTyyyVzzAww HO" for heavy oil - the product that forms in the secondary flask is typically more viscous than the oil condensed on the condenser walls.
51. Allow the reactor to cool for at least 5 hours.
52. Remove the hopper and mass.
53. Carefully remove the lid, making sure not to spill any material still on the chute or in the feeder, and place on a flat surface so that the feed pipe hangs freely.
54. Mass an empty receptacle.
55. Turn on the feed motor and gently tap the feed pipe and chute to knock any unreacted biomass into the empty receptacle.
56. Turn off the feed motor and re-mass the receptacle. Store or discard the partially reacted biomass. Do not recycle it.
57. Remove the top of the internal frame and fume hood.

58. Remove the char catch.
59. Mass a clean tray or piece of paper and set on a clean surface.
60. Flip the char catch upside-down onto the tray or paper, and strike it in multiple places with a mallet to free residual char.
61. Mass the tray or paper and pour the char into a clean collection vial.
62. Label this vial "NxxTyyyVzzAww SC" for short char.
63. Use an air hose to clean any residual char out of the catch.
64. Clean the tray or paper and re-mass.
65. Sweep the residual char on the plate onto the tray or paper.
66. Re-mass the tray or paper and pour the char into a clean collection vial.
67. Label this vial "NxxTyyyVzzAww LC" for long char.
68. Clean the reacting surface with acetone and replace the char catch.
69. Mass a clean 500 mL Erlenmeyer flask.
70. Remove the 2 L Erlenmeyer flask from the condenser and replace it with the 500 mL flask.
71. Mass the 2 L Erlenmeyer flask.
72. Mass the acetone squirt bottle.
73. Spray the condenser walls and insides of the connection joints with acetone and allow the oil/acetone mixture to drain into the flask.
74. Re-mass the squirt bottle and flask.
75. Remove the flask and pour the acetone bath into the aluminum spill tray.
76. Flip the condenser upside-down and place on a clean surface.
77. Re-mass the squirt bottle and 500 mL flask.

78. Spray the condenser walls and joints with acetone.
79. Swirl the acetone/oil mixture collected in the top of the condenser, before draining it into the flask.
80. Re-mass the flask and squirt bottle.
81. Set the condenser aside in a safe place.
82. Pour the oil from the 2L flask into the oil/acetone mixture in the 500 mL flask.
83. Transfer this mixture to a clean vial.
84. Label this vial "NxxTyyyVzzAww LO" for light oil.

REFERENCES

[1] EIA, "Annual Energy Outlook 2011," U. E. I. Agency, Ed., ed. Washington, DC: EIA, 2011.

[2] A. Uslu, *et al.*, "Pre-treatment technologies, and their effect on international bioenergy supply chain logistics. Techno-economic evaluation of torrefaction, fast pyrolysis and pelletisation," *Energy,* vol. 33, pp. 1206-1223, 2008.

[3] M. Puig-Arnavat, *et al.*, "Review and analysis of biomass gasification models," *Renewable and Sustainable Energy Reviews,* vol. 14, pp. X2841-2851, 2010.

[4] A. W. Williams, "An Investigation of the Kinetics for the Fast Pyrolysis of Loblolly Pine Woody Biomass," Doctorate of Mechanical Engineering, Mechanical Engineering, Georgia Institute of Technology, Atlanta, GA, 2011.

[5] A. M. Azeez, *et al.*, "Fast Pyrolysis of African and European Lignocellulosic Biomasses Using Py-GC/MS and Fluidized Bed Reactor," *Energy & Fuels,* vol. 24, pp. 2078-2085, 2010.

[6] M. G. Gronli, "A Theoretical and Experimental study of the Thermal Degradation of Biomass," Doktor Ingenior Doctoral Thesis, Mechanical Engineering Division of Thermal Energy and Hydro Power, The Norwegian University of Science and Technology, Trondheim, Norway, 1996.

[7] M. G. Gronli and M. C. Melaaen, "Mathematical Model for Wood Pyrolysis-Comparison of Experimental Measurements with Model Predictions," *Energy and Fuels,* vol. 14, pp. 791-800, 2000.

[8] W. R. Arthur, "The Pyrolysis of Biomass Fuels," Master of Science in Mechanical Engineering, Mechanical Engineering, Georgia Institute of Technology, Atlanta, GA, 1981.

[9] C. Branca, *et al.*, "Devolatilization of conventional pyrolysis oils generated from biomass and cellulose," *Energy and Fuels,* vol. 20, pp. 2253-2261, 2006.

[10] C. Di Blasi, *et al.*, "Degradation characteristics of straw and washed straw," *Thermochimica Acta,* vol. 364, pp. 133-142, 2000.

[11] M. Lanzetta and C. Di Blasi, "Pyrolysis kinetics of wheat and corn straw," *Journal of Analytical and Applied Pyrolysis,* vol. 44, pp. 181-192, 1998.

[12] P. Bhattacharya, *et al.*, "Wood/plastic copyrolysis in an auger reactor: Chemical and physical analysis of the products," *Fuel,* vol. 88, pp. 1251-1260, 2009.

[13] C. Di Blasi, "Linear pyrolysis of cellulosic and plastic waste," *Journal of Analytical and Applied Pyrolysis,* vol. 40-41, pp. 463-479, 1997.

[14] J. Reina, *et al.*, "Kinetic Study of the Pyrolysis of Waste Wood," *Industrial & Engineering Chemistry Research,* vol. 37, pp. 4290-4295, 1998.

[15] L. Sorum, *et al.*, "Pyrolysis characteristics and kinetics of municipal solid wastes," *Fuel,* vol. 80, pp. 1217-1227, 2001.

[16] J. R. Mayor and A. Williams, "Investigation into the Effects of Reaction Duration on the Isothermal Fast Pyrolysis of Biomass," presented at the Energy Sustainability 2009, San Francisco, CA USA, 2009.

[17] M. J. Moran, *Fundamentals of engineering thermodynamics*, 6th ed. ed. Hoboken, N.J. :: Wiley, 2008.

[18] A. Oasmaa, *et al.*, "Acidity of biomass fast pyrolysis bio-oils," *Energy and Fuels,* vol. 24, pp. 6548-6554, 2010.

[19] N. Hall. (2001) Passing the Acid Test. *Frontiers*.

[20] J. Meng, *et al.*, "The effect of torrefaction on the chemistry of fast-pyrolysis bio-oil," *Bioresource Technology,* vol. 111, pp. 439-446, 2012.

[21] R. L. Amateis and H. E. Burkhart, "Rotation-age results from a loblolly pine spacing trial," *Southern Journal of Applied Forestry,* vol. 36, pp. 11-18, 2012.

[22] A. Demirbas and G. Arin, "An Overview of Biomass Pyrolysis," *Energy Sources,* vol. 24, pp. 471-482, 2002.

[23] G. Maschio, *et al.*, "Pyrolysis, a promising route for biomass utilization," *Bioresource Technology,* vol. 42, pp. 219-231, 1992.

[24] G. Maschio, *et al.*, "Production of syngas from biomass," *Bioresource Technology,* vol. 48, pp. 119-126, 1994.

[25] R. Venderbosch and W. Prins, "Fast pyrolysis technology development," *Biofuels, Bioproducts and Biorefining,* vol. 4, pp. 178-208, 2010.

[26] A. V. Bridgwater, *et al.*, "An overview of fast pyrolysis of biomass," *Organic Geochemistry,* vol. 30, pp. 1479-1493, 1999.

[27] J. Lede, "Solar thermochemical conversion of biomass," *Solar energy,* vol. 65, pp. 3-13, 1999.

[28] L. Hofmann and M. J. Antal Jr, "Numerical simulations of the performance of solar fired flash pyrolysis reactors," *Solar energy,* vol. 33, pp. 427-440, 1984.

[29] M. J. Antal*, et al.*, "Design and operation of a solar fired biomass flash pyrolysis reactor," *Solar energy,* vol. 30, pp. 299-312, 1983.

[30] G. V. C. Peacocke and A. V. Bridgwater, "Ablative plate pyrolysis of biomass for liquids," *Biomass & bioenergy,* vol. 7, pp. 147-154, 1994.

[31] C. Di Blasi, "Heat transfer mechanisms and multi-step kinetics in the ablative pyrolysis of cellulose," *Chemical Engineering Science,* vol. 51, pp. 2211-2220, 1996.

[32] J. A. Knight*, et al.*, "Oil production by entrained flow pyrolysis of biomass," *Biomass,* vol. 6, pp. 69-76, 1984.

[33] C. W. Gorton*, et al.*, "Modeling pyrolysis oil production in an entrained-flow reactor," *Biomass,* vol. 21, pp. 1-10, 1990.

[34] M. Garcia-Perez*, et al.*, "Vacuum pyrolysis of softwood and hardwood biomass. Comparison between product yields and bio-oil properties," *Journal of Analytical and Applied Pyrolysis,* vol. 78, pp. 104-116, 2007.

[35] M. Carrier*, et al.*, "Comparison of slow and vacuum pyrolysis of sugar cane bagasse," *Journal of Analytical and Applied Pyrolysis,* vol. 90, pp. 18-26, 2011.

[36] C. Roy*, et al.*, "Development of a novel vacuum pyrolysis reactor with improved heat transfer potential," in *Developments in thermochemical biomass conversion*. vol. 1, A. V. Bridgwater and B. G. B. Boocock, Eds., ed London: Chapman and Hall, 1997.

[37] M. W. Hopkins*, et al.*, "The flash pyrolysis of cellulosic materials using concentrated visible light," *Solar energy,* vol. 32, pp. 547-551, 1984.

[38] O. Boutin*, et al.*, "Solar flash pyrolysis of biomass direct measurement of the optical properties of biomass components," *Journal De Physique. IV : JP,* vol. 9, pp. Pr3-367 - Pr3-372, 1999.

[39] C. Gomez*, et al.*, "Influence of secondary reactions on the heat of pyrolysis of biomass," *Industrial and Engineering Chemistry Research,* vol. 48, pp. 10222-10233, 2009.

[40] J. Rath*, et al.*, "Heat of wood pyrolysis," *Fuel,* vol. 82, pp. 81-91, 2003.

[41] C. A. Koufopanos*, et al.*, "Modelling of the pyrolysis of biomass particles. Studies on kinetics, thermal and heat transfer effects,"

Canadian Journal of Chemical Engineering, vol. 69, pp. 907-915, 1991.

[42] M. Van de Velden*, et al.*, "Fundamentals, kinetics and endothermicity of the biomass pyrolysis reaction," *Renewable Energy,* vol. 35, pp. 232-242, 2010.

[43] K. Papadikis*, et al.*, "CFD modelling of the fast pyrolysis of biomass in fluidised bed reactors: Modelling the impact of biomass shrinkage," *Chemical Engineering Journal,* vol. 149, pp. 417-427, 2009.

[44] D. L. Pyle and C. A. Zaror, "Heat Transfer and Kinetics in the Low Temperature Pyrolysis of Solids," *Chemical Engineering Science,* vol. 39, p. 147, 1984.

[45] F. P. Incropera, *Fundamentals of heat and mass transfer*, 5th ed. ed. New York :: J. Wiley, 2002.

[46] U. Gross, Spindler, K., and Hahne, E., "Shape factor equations for radiation heat transfer between plane rectangular surfaces of arbitrary position and size with rectangular boundaries," *Letters in Heat and Mass Transfer,* vol. 8, pp. 219-227, 1981.

[47] E. Hoekstra*, et al.*, "Heterogeneous and homogeneous reactions of pyrolysis vapors from pine wood," *AIChE Journal,* vol. 58, pp. 2830-2842, 2012.

[48] R. W. Fox, *Introduction to fluid mechanics*, 6th ed. ed. New York :: Wiley, 2004.

[49] B. Hijazi*, et al.*, "Two-step cross correlation-based algorithm for motion estimation applied to fertilizer granules' motion during centrifugal spreading," *Optical Engineering,* vol. 50, 2011.

[50] P. Van Liedekerke*, et al.*, "Recent results of experimentation and DEM modeling of centrifugal fertilizer spreading," *Granular Matter,* vol. 10, pp. 247-255, 2008.

[51] F. Rioual*, et al.*, "Rolling and sliding dynamics in centrifugal spreading," *Applied Physics Letters,* vol. 90, 2007.

[52] E. Lajeunesse*, et al.*, "Spreading of a granular mass on a horizontal plane," *Physics of Fluids,* vol. 16, pp. 2371-2381, 2004.

[53] L. Staron and E. J. Hinch, "The spreading of a granular mass: Role of grain properties and initial conditions," *Granular Matter,* vol. 9, pp. 205-217, 2007.

[54] C. Meruane*, et al.*, "On the role of the ambient fluid on gravitational granular flow dynamics," *Journal of Fluid Mechanics,* vol. 648, pp. 381-404, 2010.

[55] L. Staron and E. J. Hinch, "Study of the collapse of granular columns using two-dimensional discrete-grain simulation," *Journal of Fluid Mechanics,* vol. 545, pp. 1-27, 2005.

[56] V. N. Chelomey, "Vibration in Engineering," in *Vibrational Processes and Machinery*. vol. 4, E. E. Lavendel, Ed., ed Moscow: Mashinostroenie, 1981.

[57] V. A. Golovanevskiy*, et al.*, "Vibration-induced phenomena in bulk granular materials," *International Journal of Mineral Processing,* vol. 100, pp. 79-85, 2011.

[58] D. J. Inman, *Engineering Vibration*, 3rd ed. Upper Saddle River, NJ: Pearson Education, Inc., 2008.

[59] C. Di Blasi, "Influences of physical properties on biomass devolatilization characteristics," *Fuel,* vol. 76, pp. 957-964, 1997.

[60] A. Haider and O. Levenspiel, "Drag coefficient and terminal velocity of spherical and nonspherical particles," *Powder Technology,* vol. 58, pp. 63-70, 1989.

[61] C. H. Bamford*, et al.*, "The combustion of wood," *Proceedings Cambridge Philosophical Society,* vol. 42, pp. 166-182, 1946.

[62] Q. Fu*, et al.*, "Understanding the Pyrolysis of CCA-treated Wood Part I. Effect of Metal Ions," *Journal of Applied Pyrolysis,* vol. 81, pp. 60-64, 2008.

[63] C. Branca*, et al.*, "Critical evaluation of global mechanisms of wood devolatilization," *Thermochimica Acta,* vol. 429, pp. 133-141, 2005.

[64] F. Shafizadeh and P. P. S. Chin, "Thermal Deterioration of Wood," in *ACS symposium series , 43; Wood technology, chemical aspects,* I. S. Goldstein, Ed., ed Washington: American Chemical Society, 1977, pp. 57-81.

[65] L. Kokko*, et al.*, "Comparing the energy required for fine grinding torrefied and fast heat treated pine," *Biomass and Bioenergy,* vol. 42, pp. 219-223, 2012.